

Numerical and diagnostic techniques for modelling stratified coastal seas

Dissertation

zur Erlangung des akademischen Grades

doctor rerum naturalium (Dr. rer. nat.)

der Mathematisch-Naturwissenschaftlichen Fakultät

der Universität Rostock

vorgelegt von

Richard Hofmeister, geb. am 09.04.1982 in Neustrelitz

aus Rostock

Rostock, 22.10.2010

Gutachter

Prof. Dr. Hans Burchard

Leibniz Institut für Ostseeforschung Warnemünde, Physikalische Ozeanographie

Prof. William D. Smyth, Ph.D.

Oregon State University, College of Oceanic & Atmospheric Sciences

Tag der Verteidigung: 2. Februar 2011

I want to thank my family for supporting me in carrying out my research and I want to thank the whole Coastal-Ocean-Physical-Processes group at the Institute of Baltic Sea Research for the pleasant collaboration. I highly appreciate the cooperation with Jean-Marie Beckers throughout the last years. This work would not have been possible without the scientific guidance of my advisor Hans Burchard.

Zusammenfassung

In dieser Doktorarbeit werden die Stärken und Schwächen der numerischen Modellierung von geschichteten Küstenmeeren detailliert ausgewertet. Dafür wurden zwei verschiedene marine Systeme exemplarisch untersucht - ein flaches Ästuar, das über ein Jahr hinweg mehrmals geschichtet und wieder durchmischt wird, und die tiefere, permanent geschichtete Ostsee. Beide Systeme zeigen Einströme dichten Wassers entlang des Meeresbodens, die eine wichtige Rolle im physikalischen Regime der Systeme spielen. Daher wird hier der Ansatz verfolgt ein numerisches Modell zu verwenden, das auf dem neuesten wissenschaftlichen Stand ist und bodenfolgende Koordinaten verwendet, die die Strömung entlang des Bodens auflösen.

Die Stärken der numerischen Modellierung geschichteter Küstenmeere ist offensichtlich die Möglichkeit eine vollständige und detaillierte Analyse der wirkenden physikalischen Prozesse durchzuführen. Die Prozesse werden im besten Fall gut in Zeit und Raum durch die Diskretisierung und Implementierung der primitiven Gleichungen aufgelöst.

Um die Entstehung und den Abbau von Schichtung in flachen Gewässern zu studieren wurde im Rahmen dieser Arbeit eine Methode entwickelt, die es möglich macht die relevanten Prozesse zu analysieren. Feldmessungen können üblicherweise nicht alle nötigen Daten bereitstellen um alle beteiligten Prozesse der Ein- und Entschichtung auszuwerten. Im Beispiel, dem flachen Ästuar Limfjord, hat es die hoch-auflösende Modellstudie möglich gemacht die maßgeblichen Prozesse der Schichtung anhand der Simulation zu identifizieren. Die Prozesse der differentiellen Advektion tragen maßgeblich zur Schichtung im Limfjord bei. Zudem lieferte schon die Anwendung der Schichtungsanalyse auf idealisierte Experimente die Einsicht, dass die Schichtung durch das gleichzeitige Zusammenspiel mehrerer Prozesse bestimmt wird. Nur durch eine gute Auflösung der vertikalen und horizontalen Gradienten der Dichte und Transporte in der Wassersäule kann ein numerisches Modell die laufenden Schichtungsprozesse abbilden.

Mit dieser neuen, vollständigen Diagnosemethode der Schichtungsprozesse können empirische Abschätzungen und einfache numerische Modelle theoretisch verifiziert werden. Gleichzeitig können dabei unaufgelöste oder ignorierte Beiträge zur Schichtung abgeschätzt werden. Die Schichtungsanalyse in der realistischen, hoch-auflösenden Studie des Limfjords zeigt dass mit Hilfe eines numerischen Modells physikalische Prozesse in flachen Küstengewässern erfolgreich untersucht werden können.

Die numerische Simulation größerer und tieferer, permanent geschichteter Küstenmeere mit Auflösungen, die mit der heutigen Computerleistung zu bewältigen sind, unterliegt nachweislich großen Diskretisierungsfehlern. In der vorliegenden Arbeit wird die Ostsee untersucht, weil an den Hängen ihrer Becken typische Küstenmeerprozesse eine Rolle spielen. Die Ergebnisse sind in ähnlicher Weise für andere geschichtete Küstenmeere, wie z.B. das Schwarze Meer, gültig. Ein Anliegen dieser Arbeit ist es, numerische Techniken bereitzustellen, um die Abbildung physikalischer Prozesse durch die Diskretisierung eines Modells zu untersuchen und zu verbessern. Große Diskretisierungsfehler (wie z.B. die numerische Mischung und Druckgradientenfehler) treten in den realisierbaren Modellauflösungen auf, auch obwohl vorherige Modellstudien bereits in der Lage waren realistische Tracerbudgets für z.B. die Ostsee zu reproduzieren.

In der Arbeit wird der mischende Effekt der Druckgradientenfehler in Modellen mit bodenfolgenden Koordinaten ausgewertet, der eine maßgebliche Quelle für Unsicherheiten in numerischen Modellen darstellt. Druckgradientenfehler bauen, zusätzlich zu künstlich erzeugten Strömungen, künstlich die permanente Schichtung im Modell ab. Es wird gezeigt, dass verbesserte numerische Techniken im Modell, wie z.B. verbesserte Druckgradientenschemen und adaptive vertikale Koordinaten, die Druckgradientenfehler effektiv reduzieren.

Ein maßgebliches Ergebnis dieser Arbeit ist die Entwicklung der adaptiven vertikalen Koordinaten für realistische, drei-dimensionale, numerische Ozeanmodelle. Die Stärke der Gitteradaption wurde für idealisierte Experimente und für das realistische Beispiel der Ostsee demonstriert. Mit einem relativ kleinen, zusätzlichen Rechenaufwand durch die Benutzung adaptiver vertikaler Koordinaten können Diskretisierungsfehler genauso effektiv reduziert werden wie durch die Verdopplung der horizontalen Auflösung bei festen vertikalen Gittern, die einen weitaus größeren Rechenaufwand bedeutet. Zudem ermöglicht die optimierte Darstellung des physikalischen Regimes durch die adaptiven Koordinaten, dass diskretisierungssensitive Techniken, wie z.B. die Druckgradientenberechnung, gegen die erwartete Lösung konvergieren. In realistischen Simulationen geschichteter Küstenmeere mit heutigen Auflösungen spielt die künstliche, numerische Mischung trotz effektiver Reduzierung mit den vorgestellten Techniken immer noch eine gleichwertige Rolle im Vergleich zu der physikalisch begründeten Mischung im numerischen Modell.

Contents

1	Introduction	1
1.1	Investigation of stratification and mixing in stratified seas	1
1.1.1	Exemplary investigation of stratification and de-stratification in the Limfjord	1
1.1.2	Evaluating stratification and de-stratification in coastal seas	2
1.1.3	Exemplary investigation of mixing during inflow periods in the Baltic Sea	4
1.2	Introducing model techniques for (permanently) stratified seas	5
1.3	The GETM model system	7
1.4	The document structure	8
2	Diagnostical techniques for evaluating stratification and mixing coastal seas	9
2.1	A dynamic equation for the potential energy anomaly (PEA)	9
2.1.1	Deriving a dynamic equation for ϕ	9
2.1.2	Applications to estuarine flow	14
2.1.2.1	One-dimensional strain-induced periodic stratification	14
2.1.2.2	Comparison to empirical estimates	14
2.1.2.3	Two-dimensional estuarine dynamics	17
2.1.3	Summarising: The dynamic equation for the PEA	19
2.2	Evaluating stratification and mixing in the Limfjord	20
2.2.1	Methodology	20
2.2.2	Model validation and results	21
2.2.3	Stratification in the Limfjord	24
2.2.3.1	The processes of stratification and de-stratification according to the dynamic equation of PEA	26
2.2.3.2	Some aspects of stratification in the central basin	29
2.2.4	Summarising the Limfjord studies	33
3	Numerical techniques for modelling stratified seas	34
3.1	Adaptive vertical coordinates	34
3.1.1	Grid adaptation	34
3.1.1.1	The transformed model space	34
3.1.1.2	Optimisation technique	35
3.1.1.3	Vertical discretisation	36
3.1.1.4	Horizontal filtering of interface positions	37
3.1.1.5	Advection of z , Lagrangian approach	38
3.1.1.6	Horizontal filtering of layer thicknesses	39
3.1.1.7	Isopycnal tendency	39
3.1.1.8	Enforcing well defined grids	40

3.1.2	Implementation	41
3.1.2.1	Implementation of the grid adaption in the model loop . .	41
3.1.3	Examples	44
3.1.3.1	Internal seiche	45
3.1.3.2	Multi-basin overflow	47
3.1.3.3	Seamount test case	49
3.1.3.4	Coastal upwelling	55
3.1.4	Summarising the adaptive vertical coordinates method	59
3.2	Evaluating the internal pressure gradient (PG) calculation	63
3.2.1	Idealised Simulation of a sloping pycnocline	64
3.2.2	PG errors during stagnation in an idealised Gotland Basin	68
3.2.3	Conclusion on internal PG errors	69
4	Realistic modelling of inflows into the Baltic Sea	73
4.1	Methodology	73
4.2	Verification and comparison of different model techniques	75
4.3	Spacial hydrography of the inflows as projected by the model	83
4.4	Characteristic inflow dynamics in channelled bathymetry	88
4.5	Conclusions on the Baltic Sea modelling	88
5	Summary and conclusions	91
	Bibliography	93

1 Introduction

1.1 Investigation of stratification and mixing in stratified seas

Understanding the processes of stratification and mixing is essential for the assessment and usage of the marine, coastal environment. The aim of the present thesis is to provide numerical and diagnostic techniques for studying the processes of stratification and mixing in stratified, coastal seas.

The motivation for the development of the new techniques for models of stratified seas arose from the desire to understand of the stratification in the Limfjord, Denmark, and the desire to understand the mixing during inflow periods in the Baltic Sea. These two, very different regimes are the study areas representative for shallow estuaries and permanently stratified seas. Both systems are characterised by dense currents along the sea bed, which suggests the approach to use a numerical ocean model with bottom-following coordinates in the studies below. For the high-resolution model study in the Limfjord, an exemplary process study is presented below, whereas the study of the Baltic Sea required to improve the numerical techniques in order to reduce numerical uncertainties when studying processes in stratified regimes.

1.1.1 Exemplary investigation of stratification and de-stratification in the Limfjord

In shallow seas and estuaries, understanding the physical effects of development and breakdown of stratification is a key to understanding the ecosystem dynamics of such regions. Physical processes due to vertical mixing of heat, salt and momentum depend on the intensity of stratification. The vertical mixing also controls properties which are relevant for the marine ecosystem, like the flux of nutrients and the vertical transport of phytoplankton. A re-distribution of particulate suspended matter feeds back in the turbidity and thus into the physical system. For example, the primary production of phytoplankton takes place in a near-surface layer. Under unstratified conditions, turbulent mixing distributes the produced phytoplankton in the whole water column, leading to low productivity when the water depth exceeds the depth of the euphotic zone. In a stratified regime, suppressed turbulence at the pycnocline leads to a shallower mixed layer, such that the phytoplankton cannot leave the euphotic zone by means of turbulent mixing. That process leads to exponential algal growth as long as nutrients are not limiting (*Sverdrup* [1953]). High phytoplankton concentrations however will increase the turbidity of the mixed layer, limit absorption of solar radiation to a shallower layer, increasing stratification and thus further shallowing of the mixed layer (*Burchard et al.* [2006]). The subsequent self-shading of phytoplankton may limit the primary production even in the presence of sufficient nutrient concentration (*Cloern* [1987]).

Stratification and mixing do not only affect the primary production, but can have a large impact on the supply of phytoplankton to benthic filter feeders (*Frechette and Bourget* [1985]). In areas with high density of benthic filter feeders, like the Limfjord (see below) where mussels are cultivated on shellfish beds, the mussels may consume more phytoplankton and oxy-

gen than is transported downwards, which results in an oxygen and food depletion boundary layer near the sea bed (*Ackermann et al.* [2001], *Muschenheim and Newell* [1992]). Oxygen depletion may lead to the extinction of whole shellfish communities and thus a huge economic loss in periods of strong stratification as happened in 1997 in the Mariager Fjord, Denmark (*Fallesen et al.* [2000]).

The exemplaric study site, the Limfjord is a shallow sound in Denmark. It stretches from the western opening to the North Sea (Fig. 2.6 shows a map) to the Kattegat at the western side with a length of approximately 180 km. The irregular shape of the Limfjord shows several basins and channels. The mean water depth is about 4.5 m with a maximum depth of 24 m. In the central basin, Løgstør Bredning, the mean depth is about 5.8 m. There is a permanent horizontal salinity gradient between the two boundaries, with a salinity of 32-34 psu at the connection to the North Sea and 19-25 psu at the connection to the Kattegat. The total water volume in the Limfjord is 7.1 km³, comparing to the net west-east through-flow of 8.7 km³ per year. With a freshwater input from rivers in the same order of magnitude cumulating up to 2.4 km³ in 2003, the Limfjord is neither dominated by North Sea water only, nor by riverine freshwater only, but rather by the interaction of both.

The stratification in the Limfjord was already studied by *Wiles et al.* [2006]. They evaluated stratification in terms of potential energy anomaly (PEA) as defined by *Simpson et al.* [1977] and suggested an empirical model for the temporal evolution of PEA in the Limfjord. The progressing terms describe influences of waves, heating, horizontal density gradients, wind, and tides. These kind of terms empirically describing sources and sinks of the PEA are widely used in the literature (*Simpson and Bowers* [1981], *Simpson et al.* [1990], *Nunes Vaz et al.* [1989], *Ranasinghe and Pattiaratchi* [1999], *Gale et al.* [2006]). The zero-dimensional model for the temporal evolution of the local PEA used by *Wiles et al.* [2006] showed that stratification and de-stratification is mainly controlled by the heat flux and surface wave mixing. *Burchard and Hofmeister* [2008] showed that these terms based on empirical parameters lack generality and recommend to evaluate the temporal evolution of the PEA from a dynamic equation derived from the dynamic equation of density (see section 2.1). This approach includes effects of differential advection and was already used with further assumptions for shelf sea studies by *van Aken* [1986] and recently by *de Boer et al.* [2008] for a Rhine outflow model study.

1.1.2 Evaluating stratification and de-stratification in coastal seas

For studying processes of stratification and destratification, it is therefore essential to define a suitable measure for the stability of the water column, which can be easily quantified from field observations as well as from numerical models. As a convenient measure, the potential energy anomaly ϕ has been defined by *Simpson* [1981] as the amount of mechanical energy (per m³) required to instantaneously homogenise the water column with a given density stratification:

$$\phi = \frac{1}{D} \int_{-H}^{\eta} gz(\bar{\rho} - \rho) dz = -\frac{1}{D} \int_{-H}^{\eta} gz\bar{\rho} dz \quad (1.1)$$

with the depth mean density

$$\bar{\rho} = \frac{1}{D} \int_{-H}^{\eta} \rho dz, \quad (1.2)$$

the deviation from the depth-mean density, $\tilde{\rho} = \rho - \bar{\rho}$, the mean water depth H , the sea surface elevation η , the actual water depth $D = \eta + H$, and the gravitational acceleration g .

Due to its tremendous relevance to the marine ecosystem, stratification and de-stratification processes in shelf seas have been intensively studied during the last decades. In their key paper on fronts in the Irish Sea, *Simpson and Hunter* [1974] made an important step towards quantifying processes determining stratification in shelf seas. *Simpson et al.* [1977] first suggested to use the potential energy of the water column derived from continuous density profiles as a measure for stratification, and *Simpson* [1981] finally defined the potential energy anomaly as shown in (1.1).

Several authors have derived dynamic equations for ϕ under idealised conditions. *Simpson* [1981] assumed vanishing horizontal density gradients and divergence-free depth-mean horizontal currents and considered surface heat fluxes as the only source of stratification, and from these assumptions derived a ϕ -equation including ϕ -advection, surface heat flux and vertical mixing. The ϕ -advection term has been neglected by *van Aken* [1986], but he added the effects of horizontal density gradients (constant over the vertical). This process was denoted as *differential advection* and includes effects of tidal straining and estuarine circulation. Recently, in order to investigate the processes of stratification and mixing in an idealised Rhine outflow model, *de Boer et al.* [2008] derived a dynamic equation for ϕ under the assumptions of constant water depth and zero surface and bottom density fluxes, as well as vanishing horizontal turbulent transport and sea surface elevation and water depth gradients.

There have been many suggestions made for parameterisations of the source and sink terms in the ϕ -equation. Based on constant bulk mixing efficiencies and drag coefficients, *Simpson* [1981] and *Simpson and Bowers* [1981] derived expressions for wind and tidal mixing. Since indeed the mixing efficiency is highly variable (zero for vanishing stratification), *Simpson and Bowers* [1981] suggested mixing efficiencies depending on ϕ itself. *Nunes Vaz et al.* [1989] parameterised the mixing effect of convective surface cooling by means of a constant mixing efficiency for this process. As further mixing process, *Wiles et al.* [2006] parameterised the effect of surface wave breaking as function of significant wave height and wave period. Straining of vertically constant horizontal density gradients by tides and estuarine circulation has been parameterised by *Simpson et al.* [1990] on the basis of velocity profiles from analytical theory for tidal flow and for estuarine circulation. *Wiles et al.* [2006] furthermore suggested an empirical expression for the effect of absorption of short-wave radiation in the water column and (for shallow water) at the sea bed.

The potential energy anomaly has been used in numerous studies for quantifying the relative contributions of different processes of stratification and de-stratification in coastal seas and estuaries. Early studies concentrated on the positions and movements of fronts in shelf seas, see e.g. *Simpson et al.* [1977], *Simpson* [1981] and *Simpson and Bowers* [1981] who analysed field data from the Irish Sea and the British Channel, and *van Aken* [1986] who studied frontal dynamics in the Southern North Sea. Mixing by surface cooling and re-stratification by dense water overflows have been studied by *Rippeth and Simpson* [1996] for the Clyde Sea. The competition between tidal straining and vertical mixing has been intensively investigated for the Liverpool Bay by *Simpson et al.* [1990], *Sharples and Simpson* [1995], *Rippeth et al.* [2001], and *Scott* [2004]. For the shallow Limfjord in Denmark in which competition between the stratificational effects of estuarine circulation and surface heating and the mixing due to wind, waves and surface cooling leads to episodic stratification in summer with potentially hazardous consequences for benthic filter feeder populations, *Wiles et al.* [2006]

studied the balance of empirical source terms in the ϕ -equation. The dynamics of Intermittently Closed and Open Lakes and Lagoons (ICOLs) has been intensively studied by means of analysing the empirical ϕ -equation terms by *Ranasinghe and Pattiaratchi [1999]* and *Gale et al. [2006]*.

No study however has so far rigorously derived the ϕ -equation. Effects of sloping sea beds, surface slopes, vertical variations of horizontal density gradients, vertical advection, internal heating due to absorption of short-wave radiation, non-linear effects of the equation of state for sea water and the divergence of horizontal turbulent density fluxes have not yet been considered.

It is therefore the aim of the study in section 2.1 to rigorously derive a time-dependent dynamic equation for ϕ , based on the dynamic equations for potential temperature and salinity, the continuity equation and an equation of state for the potential density. With these equations given, no further approximations will be made. A ϕ -equation which is fully consistent with the dynamic equations discretised in numerical models will provide a tool for numerically quantifying all terms relevant for generation and destruction of stratification. It will further help to improve parameterisations for empirical ϕ -equations as they have been extensively used for studying the dynamics of estuaries and coastal seas.

1.1.3 Exemplary investigation of mixing during inflow periods in the Baltic Sea

The Baltic Sea (see figure 4.1) is a brackish sea between the European main continent and Scandinavia in the transitions between typical estuaries, such as the Neva estuary, and the narrow connections to the shelf sea. The topography is determined by different basins connected with channels and over sills. The main central basin is the Gotland Basin with up to 240 m depth. In the deeper basins of the Baltic Sea, there is a permanent salinity stratification with a halocline at around 80 m depth. Due to the temperature-salinity-properties, the density is determined mainly by salinity. The permanent salinity stratification is maintained by occasional major, saline inflows during inflow “seasons” separated statistically by stagnation periods of 1-4 years (*Matthäus and Frank [1992]*). These inflows propagate from the Kattegat through the Belt Sea into the central Baltic Sea. One period of recent major inflow “seasons” is the years 2002-2004 after a 4-5 years period without major inflows (*Feistel et al. [2003]*). The driving forces for the major inflows are well understood (*Schinke and Matthäus [1998]*; *Matthäus and Frank [1992]*; *Feistel et al. [2006]*) as being a wind-induced, barotropic forcing during winter times and baroclinic forcing during summer times. A number of numerical circulation studies showed that numerical models are able to re-construct the volume and salinity budgets of the central Baltic Sea (*Lehmann and Hinrichsen [2000]*, *Lehmann et al. [2004]*; *Meier et al. [2004]*; *Kremp et al. [2007]*; *Meier [2007]*). Observations during inflow periods showed a very detailed hydrography (*Piechura and Beszczynska-Möller [2003]*; *Golenko et al. [2008]*; *Umlauf et al. [2007]*) in the basins and channelled bathymetry. Nevertheless, the physical processes acting locally during the inflow into the central Baltic Sea, such as entrainment of ambient water in a gravity current and eddy mixing, are still subject to research (*Wählin and Cenedese [2006]*; *Umlauf and Arneborg [2009a, b]*; *Reissmann et al. [2009]*). In the numerical models, the resolution of the physical processes as indicated by the observations of, e.g., occasionally strong stratification and boundary layer mixing is almost impossible to achieve with the present computer power. Also the numerical treatment of near-bottom processes in geopotential coordinates (as used in *Kremp et al. [2007]*, *Meier et al. [2004]*, *Meier [2007]*) is subject to discretisation errors for heights of the

gravity currents, which are comparable to typical bathymetric steps resulting the horizontal and vertical discretisation. *Rennau and Burchard* [2009] showed for the western Baltic Sea, that uncertainties due to numerical mixing are comparable to the simulated turbulent mixing, even for higher resolutions as typically used in the recent Baltic Sea modelling studies. Hence, analysing mixing as a result of the explicitly simulated turbulence will not include the total tracer mixing as projected in the simulation. It can be assumed that similar to the approach of *Riemenschneider and Legg* [2007], the numerical mixing is compensating the unresolved physical processes partially. In bottom-boundary-layer resolving models using terrain following coordinates, the permanent salinity stratification in the central Baltic Sea would be subject to internal pressure gradient errors (see, e.g., *Shchepetkin and McWilliams* [2003] and references therein), which impact on the model results by artificial circulation and mixing. However, *Burchard et al.* [2009] showed promising model results for the inflows into the western Baltic Sea with a sigma-coordinate model. It is therefore due to evaluate the conflict between pressure gradient errors and the resolution of along-bottom moving inflows for Baltic Sea modelling. Additionally to the halocline, a thermocline builds up in summer and is moved downward by strong wind events over the year. Due to the coastline of the Baltic Sea, up-welling is happening throughout the whole year along some of the Baltic coasts and displaces the pycnoclines off the coast and thus is subject to numerical mixing in a fixed model grid. A numerical model for the Baltic Sea has to reproduce numerically the effect of the permanently moving pycnoclines, which suggests to use isopycnal coordinates (*Halliwell* [2004], *Chassignet et al.* [2006]) with a very high number of density layers in order to resolve the wide (horizontal) range of Baltic densities and the turbulent mixing in the boundary layers. The alternative, chosen for assessment in the present study, is gradient-adaptive vertical model layers (as presented in *Hofmeister et al.* [2010b] also for an idealised up-welling scenario).

Hofmeister et al. [2010b] also showed for idealised model experiments that numerical mixing and pressure gradient errors can be reduced by the adaptive vertical coordinate method, with keeping boundary layer resolving terrain-following coordinates.

1.2 Introducing model techniques for (permanently) stratified seas

The modelling of permanently stratified, coastal seas requires that the model can preserve the stratified regime but also resolves the processes in the boundary layers. Although numerical model techniques improved during the last decades, fulfilling both requirements is a non-trivial challenge, even in higher-resolution models. In chapter 3, a new vertical coordinate method for layered, coastal ocean models is presented. It is developed for improving the simulations of permanently stratified, coastal seas by reducing discretisation errors.

In *Burchard and Beckers* [2004] a strategy to create a vertical grid layer distribution that adapts the distribution of calculation points to the solution of a vertical 1D ocean model is presented. The purpose for that method was paving the way for extensions to 3D models where adaptations could be more beneficial than in a 1D case. In section 3.1, we therefore generalise this approach to the more interesting 3D case, with the aim to provide some strategies to adapt the numerical grid vertically with keeping the horizontal distribution of coordinates unchanged. The reason for using adaptive grids in 3D models can be found in the analysis of the different advantages and drawbacks of the vertical coordinate systems classically used in 3D ocean models.

One can basically distinguish z -coordinate models (e.g. Modular Ocean Model, see *Bryan* [1969]), σ coordinate models (e.g. Princeton Ocean Model, *Blumberg and Mellor* [1987]), or isopycnal models (e.g. *Bleck and Smith* [1990], *Bleck* [2002]). For z -coordinates models grid lines are horizontal, for σ coordinates they interpolate between surface and bottom slopes and for isopycnal models they follow density surfaces. When comparing advantages and disadvantages of the different kind of models, it appears that the choice of a particular vertical coordinate system has some advantages in some occasions (and locations), but is not optimal in other locations or moments (see *Griffies et al.* [2001]). Also sometimes, the optimal choice of the vertical coordinates would depend upon the characteristics of the circulation which may change in space and time. The presently optimal model should make use of isobaric coordinates near surface, isopycnal coordinates in the interior and sigma coordinates at the bottom.

If one had a model in which different vertical coordinate systems could be used, one could more easily distinguish and separate the different contributions to changes in simulation results (as presented in *Ezer* [2005] for a downflow experiment). Such a hybrid coordinate model has already been introduced by *Kasahara* [1974] in the sense that a generalised vertical coordinate transformation was suggested for ocean models. The so called s -coordinate models or hybrid coordinate models see *Song and Haidvogel* [1994]; *Burchard and Petersen* [1997]; *Madec et al.* [1998]; *Pietrzak et al.* [2002]) are now standard modelling tools. They allow vertical coordinates to be located in a completely arbitrary way and therefore allow to compare the effect of different choices of coordinate systems. However, presently generalised coordinates models do not yet consider the question how to dynamically change the coordinates in an optimal way so as to reduce the numerical discretisation errors. Errors that could be reduced include e.g. errors in isopycnal diffusion discretisations (*Beckers et al.* [2000]), pressure gradient errors (*Deleersnijder and Ruddick* [1992]), unsatisfactory representation of downslope flow of plumes (*Beckmann and Döscher* [1997]), numerical damping of internal waves (*Stanev and Beckers* [1999]) and numerical mixing in stratified basins (*Rennau and Burchard* [2009]).

Such error reductions are generally not done dynamically, since hybrid models and more classic models are often used in an *a priori* way, where the coordinates are placed according to the modellers *a priori* knowledge of the processes to be properly resolved. This approach is certainly already advantageous compared to the classic models were such a free choice is not possible, but it does not use the possibility of adapting the coordinate positions during the calculation according to the modelling results themselves¹.

Though standard in classic computational fluid dynamics (see *Thompson et al.* [1985]; *Liseikin* [1999]) or atmospheric models (see *Fiedler* [2002]), the use of adaptive vertical grids in ocean models is rare. Exceptions are the use of grid adaptation by empirical functions to achieve boundary layer refinements in isopycnal models (see *Dewar and McDougall* [2000]; *Holt and James* [2001]; *Bleck* [2002]) or grid refinements on horizontally meshes (by adaptive nesting for example *Blayo and Debreu* [1999]). A general extension to the s -coordinate system has been suggested by *Song and Hou* [2006], who showed that hybrid coordinate systems allow for reducing discretisation errors without losing the advantages of terrain following coordinates. A hybridisation of different vertical grids with regard to global ocean modelling

¹ σ -coordinate models are of course adaptive grids in the sense that they follow sea surface elevation changes, and isopycnal models are also adaptive in the sense that they follow isopycnals. Here we refer to adaptive grids as to those which explicitly include a strategy to modify the vertical distributions of coordinate points by other means.

is used in the HYCOM model (*Bleck [2002]; Halliwell [2004]; Chassignet et al. [2006]*) to allow the transition from an isopycnal grid for the deep ocean to a terrain-following grid in shallow waters and a near- z -level grid at the surface. Here our objective is to define and test strategies to generate dynamically adaptive vertical grids based on the simulation results themselves.

Some aspects of adaptive grids in meteorological modelling should be considered here. *Behrens et al. [2000]* used a semi-Lagrangian approach to move adaptive grid refinements in a meteorological model which allows to keep sharp structures in a moving grid even without increasing the total resolution of the model grid. For ocean modelling applications, *Adcroft and Hallberg [2006]* discuss the benefits and drawbacks of Lagrangian and Eulerian approaches and prefer an arbitrary Lagrangian-Eulerian method with a generally Lagrangian coordinate allowing for cross-coordinate flow. This is applied and tested for the adaptive grid method presented here.

The pressure gradient problem in σ or s -coordinate models (*Mellor et al. [1994], Haney [1991], Burchard and Petersen [1997]*) is shown to be reduced by numerically advanced model techniques for non-isopycnal vertical coordinates. The vertically adapted grid generally has to deal with the calculation of horizontal gradients (*Stelling and van Kester [1994]*) and the internal pressure gradient (*Shchepetkin and McWilliams [2003]* and references therein).

Auclair et al. [2000] showed that an optimised grid placement (double σ -coordinate systems) and an optimised initial density field can significantly reduce truncation errors in ocean models at least for fixed grids. Also *Song [1998]* and *Song and Wright [1998]* argue that the truncation error in the pressure gradient calculation is minimised for optimal grid distributions. In meteorological modelling, grid adaption with respect to estimates of the truncation error for adaptive grids is advocated by *Skamarock [1989]*.

The vertical adaptive coordinate method, as presented in section 3.1, is expected to optimise the vertical grid in an optimal way for calculating horizontal gradients. A near-isopycnal grid adaption would improve the representation of diffusive fluxes as discussed by *Mellor and Blumberg [1985]* and recently by *Marchesiello et al. [2009]*. Advantages for mass transport modelling with a grid method adapting to vertical gradients of sediment are shown by *Wai and Lu [1999]* for modelling sediment transport. In their case, a Eulerian-Lagrangian technique was used for flat-bottom experiments. In general oceanic applications, it is needed to account for multiple state variables for the grid adaption (as the idea of *Burchard and Beckers [2004]*). Additionally, with coarser resolution and strongly varying topography, the grid could get distorted such that it would need strong horizontal filtering.

1.3 The GETM model system

GETM is the abbreviation for General Estuarine Transport Model. It is a fully baroclinic ocean-circulation model based on the primitive equations with hydrostatic and Boussinesq assumption (*Burchard and Bolding [2002], Burchard et al. [2004]*). The model has implemented a free surface with drying and flooding such that the dynamics of intertidal flats can be reproduced. The turbulence closure models are taken from GOTM, a public domain water column model providing an archive of state of the art turbulence closure models (*Burchard et al. [2002], Umlauf et al. [2005], GOTM [2005]*) and GETM works with the eddy viscosity assumption.

The numerical discretisation in the model uses the Arakawa C-Grid approach (see *Arakawa and Lamb [1977]*) and bottom-following, vertical coordinates (as described in more detail

in section 3.1). GETM is implemented with mode splitting between barotropic and baroclinic mode. The free surface and the vertically integrated velocities are calculated explicitly whereas for the baroclinic mode, the tracer equations, vertically resolved currents and turbulent quantities are integrated usually with a larger timestep than for the barotropic mode. These different timesteps are called micro timestep for the barotropic mode and macro timestep for the baroclinic mode in the following sections. Both modes are two-way coupled using an iterative approach: the baroclinic velocity profile is shifted in terms of vertical mean transport as necessary to fit the vertical integrated transport from the barotropic mode. Contributions from the three-dimensionally resolved bottom friction, the advection, the diffusion and the pressure gradient force correct the assumptions of vertically homogeneity in the vertically integrated momentum equations used in the barotropic mode.

Bed friction is implemented by a logarithmic law assumption for the velocity in the near-bottom layer with the bottom roughness length as tunable parameter for friction stresses and the logarithmic law itself. The effect of the bed friction in the upper layers is examined by the turbulence model.

GETM has high order, positive-definite advection schemes implemented for the discretisation of momentum, salt and temperature advection (*Pietrzak [1998]*).

The pressure gradient formulations included in GETM contain several standard second-order formulations (*Blumberg and Mellor [1987]*; *Song [1998]*), a high-order approximation suggested by *Shchepetkin and McWilliams [2003]* and a monotone, horizontal interpolation method suggested by *Stelling and van Kester [1994]*.

The GETM code is written in Fortran 90/95 with a modular code structure and prepared for parallel computing. Input and output data can be handled in the self-describing NetCDF format. GETM and GOTM are public domain models under the GNU Public Licence.

1.4 The document structure

In the present dissertation, the following three chapters represent the work of Richard Hofmeister published in the recent years². Chapter 2 will introduce a dynamic equation for the potential energy anomaly as published by *Burchard and Hofmeister [2008]*, where the author contributed to the publication in the theoretical work and provided the two-dimensional simulation and analysis. The dynamic equation for the potential energy anomaly is then applied for the exemplary investigation of the processes of stratification and de-stratification in the Limfjord as published in *Hofmeister et al. [2009]*. In chapter 3, the adaptive vertical coordinates method is introduced in section 3.1 as published in *Hofmeister et al. [2010b]*. Additionally different internal pressure gradient schemes are evaluated for idealised models with respect to realistic Baltic Sea modelling. The chapter 4 contains results of the realistic modelling of the Baltic Sea using the adaptive coordinates as submitted for publication in *Hofmeister et al. [2010a]*.

²also sections 1.1.1 to 1.1.3 and section 1.2 in the thesis's introduction are based on the published work listed below

2 Diagnostical techniques for evaluating stratification and mixing coastal seas

2.1 A dynamic equation for the potential energy anomaly (PEA)

This section is organised as follows: First, the time-dependent dynamic equation for ϕ is derived in section 2.1.1 and the resulting terms in the ϕ -equation are discussed. Afterwards, the dynamics of ϕ is evaluated for idealised vertically-resolving model studies (section 2.1.2). In section 2.1.2.1, a one-dimensional study of tidal straining and wind mixing is described, and the resulting source terms in the ϕ -equation are compared to empirical estimates in section 2.1.2.2. In section 2.1.2.3, a two-dimensional estuarine study is presented, with the evaluation of ϕ -terms at two locations, in the periodically stratified area of the outer estuary and further upstream in the permanently stratified salt wedge area. Some conclusions about implications of the ϕ -equation will be given in section 2.1.3.

2.1.1 Deriving a dynamic equation for ϕ

The dynamic equation for ϕ will be obtained by combining the definition of ϕ from (1.1) with a dynamic equation for the potential density ρ , see *van Aken* [1986]. In oceanography, this may be derived from the dynamic equations for potential temperature θ and salinity S :

$$\partial_t \theta + \mathbf{u} \cdot \nabla_h \theta + w \partial_z \theta - \partial_z (K_v \partial_z \theta) - \nabla_h (K_h \nabla_h \theta) = \frac{1}{\rho_0 C_p} \partial_z I, \quad (2.1)$$

$$\partial_t S + \mathbf{u} \cdot \nabla_h S + w \partial_z S - \partial_z (K_v \partial_z S) - \nabla_h (K_h \nabla_h S) = 0, \quad (2.2)$$

with the horizontal velocity vector \mathbf{u} and the vertical velocity w , jointly fulfilling the continuity equation

$$\nabla_h \cdot \mathbf{u} + \partial_z w = 0. \quad (2.3)$$

Here, ∇_h denotes the horizontal gradient operator, such that $\nabla_h \cdot \mathbf{u}$ is the horizontal flow divergence. In (2.1) and (2.2), K_v and K_h denote the vertical eddy diffusivity and the horizontal eddy diffusivity, respectively, resulting from down-gradient parameterisations of vertical and horizontal turbulent fluxes. For simplicity, higher order turbulence closure approaches partially resulting in counter-gradient parameterisations are not considered here, but may be included in this approach in a straight-forward way. The term on the right hand side of the temperature equation is the heating due to absorption of solar radiation, with the constant reference density ρ_0 , the heat capacity C_p (here assumed to be constant) and the short wave radiation I , the gradient of which strongly depends on the light attenuation properties of the water, see *Paulson and Simpson* [1977].

For the derivation of a dynamic equation for potential density based on the temperature and salinity equation, it is essential to consider the non-linear equation of state for sea water (see e.g. *Jackett et al.* [2006]):

$$\rho = \rho(\theta, S, p_0) \Rightarrow \begin{cases} \nabla_h \rho = -\rho\alpha \nabla_h \theta + \rho\beta \nabla_h S, \\ \partial_z \rho = -\rho\alpha \partial_z \theta + \rho\beta \partial_z S, \\ \partial_t \rho = -\rho\alpha \partial_t \theta + \rho\beta \partial_t S, \end{cases} \quad (2.4)$$

with the constant reference pressure p_0 , the thermal expansion coefficient $\alpha = -(1/\rho)\partial_\theta \rho$ and the haline contraction coefficient $\beta = (1/\rho)\partial_S \rho$.

By combining (2.1) and (2.2) under consideration of (2.4), we obtain

$$\partial_t \rho + \mathbf{u} \cdot \nabla_h \rho + w \partial_z \rho - \partial_z (K_v \partial_z \rho) - \nabla_h (K_h \nabla_h \rho) = Q \quad (2.5)$$

with the source term for density,

$$Q = -\frac{\rho\alpha}{\rho_0 C_p} \partial_z I + K_v \partial_z \theta \partial_z (\rho\alpha) - K_v \partial_z S \partial_z (\rho\beta) + K_h \nabla_h \theta \cdot \nabla_h (\rho\alpha) - K_h \nabla_h S \cdot \nabla_h (\rho\beta). \quad (2.6)$$

For the derivation of a dynamic ϕ -equation, we furthermore need to define the depth mean horizontal velocity vector

$$\bar{\mathbf{u}} = \frac{1}{D} \int_{-H}^{\eta} \mathbf{u} \, dz. \quad (2.7)$$

It is furthermore convenient to define a vertical velocity \bar{w} , which together with $\bar{\mathbf{u}}$ fulfils a continuity equation:

$$\nabla_h \cdot \bar{\mathbf{u}} + \partial_z \bar{w} = 0. \quad (2.8)$$

>From (2.8), it is clear that \bar{w} is linear and integration of (2.8) gives

$$\bar{w} = -\bar{\mathbf{u}} \cdot \nabla_h H \frac{\eta - z}{D} + (\partial_t \eta + \bar{\mathbf{u}} \cdot \nabla_h \eta) \frac{z + H}{D}. \quad (2.9)$$

Here, we have used the vertically integrated incompressibility equation,

$$\partial_t \eta = -\nabla_h \cdot (D\bar{\mathbf{u}}), \quad (2.10)$$

and we have applied a kinematic boundary condition for \bar{w} at the bottom,

$$\bar{w}(-H) = -\bar{\mathbf{u}} \cdot \nabla_h H. \quad (2.11)$$

With this, \bar{w} is the vertical velocity which would result from kinematic boundary conditions (alignment of the flow velocity vector with bottom and surface) and the incompressibility condition for the case of vertically homogeneous horizontal flow velocity. For this case, the flow would be parallel to depth-proportional coordinates (so-called σ coordinates, see e.g. *Blumberg and Mellor* [1987]). With this definition of the linearly varying vertical velocity \bar{w} , a dynamic equation for ϕ can be derived in a concise form (see below).

The deviation from the depth-mean horizontal velocity vector is defined as $\tilde{\mathbf{u}} = \mathbf{u} - \bar{\mathbf{u}}$ and the deviation from the linear vertical velocity as $\tilde{w} = w - \bar{w}$. Surface volume fluxes due

to precipitation and evaporation are neglected here for simplicity, but may be included in a straight-forward way.

Combining (1.1), (1.2), (2.5), (2.7) and (2.9), we obtain a time-dependent dynamic equation for ϕ :

$$\begin{aligned}
 \partial_t \phi = & \underbrace{-\nabla_h(\bar{\mathbf{u}}\phi)}_{(A)} + \underbrace{\frac{g}{D}\nabla_h\bar{\rho}\cdot\int_{-H}^{\eta}z\tilde{\mathbf{u}}\,dz}_{(B)} \\
 & \underbrace{-\frac{g}{D}\int_{-H}^{\eta}\left(\eta-\frac{D}{2}-z\right)\tilde{\mathbf{u}}\cdot\nabla_h\tilde{\rho}\,dz}_{(C)} \\
 & \underbrace{-\frac{g}{D}\int_{-H}^{\eta}\left(\eta-\frac{D}{2}-z\right)\tilde{w}\partial_z\tilde{\rho}\,dz}_{(D)} \\
 & + \underbrace{\frac{\rho_0}{D}\int_{-H}^{\eta}P_b\,dz}_{(E)} - \underbrace{\frac{\rho_0}{2}(P_b^s+P_b^b)}_{(F)} + \underbrace{\frac{g}{D}\int_{-H}^{\eta}\left(\eta-\frac{D}{2}-z\right)Q\,dz}_{(G)} \\
 & + \underbrace{\frac{g}{D}\int_{-H}^{\eta}\left(\eta-\frac{D}{2}-z\right)\nabla_h(K_h\nabla_h\rho)\,dz}_{(H)},
 \end{aligned} \tag{2.12}$$

with the vertical buoyancy flux

$$P_b = \frac{g}{\rho_0}K_v\partial_z\rho, \tag{2.13}$$

and the surface buoyancy flux P_b^s and the bottom buoyancy flux P_b^b . For the derivation of (2.12), we have applied the kinematic boundary conditions

$$w(\eta) = \partial_t\eta + \mathbf{u}(\eta)\cdot\nabla_h\eta, \quad w(-H) = -\mathbf{u}(-H)\cdot\nabla_h H \tag{2.14}$$

as well as the Leibniz rule for derivatives of integrals with moving limits,

$$\begin{aligned}
 \partial_s \int_{a(s)}^{b(s)} f(s, \xi) \, d\xi = \\
 \int_{a(s)}^{b(s)} \partial_s f(s, \xi) \, d\xi + \partial_s b(s) f(s, b(s)) - \partial_s a(s) f(s, a(s)).
 \end{aligned} \tag{2.15}$$

In (2.12) the terms on the right hand side have the following meaning:

A: ϕ -advection due to the vertical mean horizontal velocity vector, $\bar{\mathbf{u}}$, including also density advection with the linearly varying vertical velocity \bar{w} as defined in (2.9); the

consideration of ϕ -advection has already been suggested by *Simpson* [1981] who however assumed a non-divergent depth-mean flow ($\nabla_h \cdot \bar{\mathbf{u}} = 0$) for better estimating the movements of fronts in shelf seas.

- B: *depth-mean straining*, based on the vertical mean horizontal density gradient strained by the deviation from the depth-mean velocity vector, $\tilde{\mathbf{u}}$; this term has first been derived by *Bowden* [1981] and has been denoted as the *differential advection* term by *van Aken* [1986];
- C: *non-mean straining*, based on straining of the deviation from the vertical mean horizontal density gradient; for the case of no mean horizontal density gradient ($\nabla_h \bar{\rho} = \mathbf{0}$), the non-mean straining term may still change the stratification. If in the lower half of the water column ($\eta - D/2 - z > 0$) the velocity anomaly is in the direction of decreasing density ($\tilde{\mathbf{u}} \cdot \nabla_h \tilde{\rho} < 0$), then the water column is stabilised ($\partial_t \phi > 0$), and vice versa, see figure 2.1;
- D: *vertical advection*, based on the deviation from the linear vertical velocity, \tilde{w} ; for a stably stratified two-layer flow the value of ϕ is largest when the interface between the two layers is at mid-depth. Therefore, for stable stratification ($\partial_z \tilde{\rho} < 0$), an upward displacement of isopycnals ($\tilde{w} > 0$) in the lower half of the water column ($\eta - D/2 - z > 0$) increases ϕ and vice versa, see figure 2.1;
- E: *vertical mixing* of density expressed as the integrated vertical buoyancy flux. By using the dynamic equation for the turbulent kinetic energy, this term may be expressed by means of the vertically integrated shear production and dissipation, see e.g. *van Aken* [1986];
- F: *surface and bottom buoyancy fluxes*, with negative (downward, e.g. surface warming) buoyancy fluxes both increasing ϕ ;
- G: *inner sinks or sources* of potential density, with a density decrease ($Q < 0$, e.g. solar radiation) in the upper half of the water column ($\eta - D/2 - z < 0$) increasing ϕ and vice versa;
- H: *divergence of horizontal turbulent transport*. The structure of this term is in analogy to term G, i.e. horizontal density flux divergence ($\nabla_h (K_h \nabla_h \rho) < 0$) in the upper half of the water column has a stabilising effect.

The kinematic terms A - D are graphically sketched in figure 2.1.

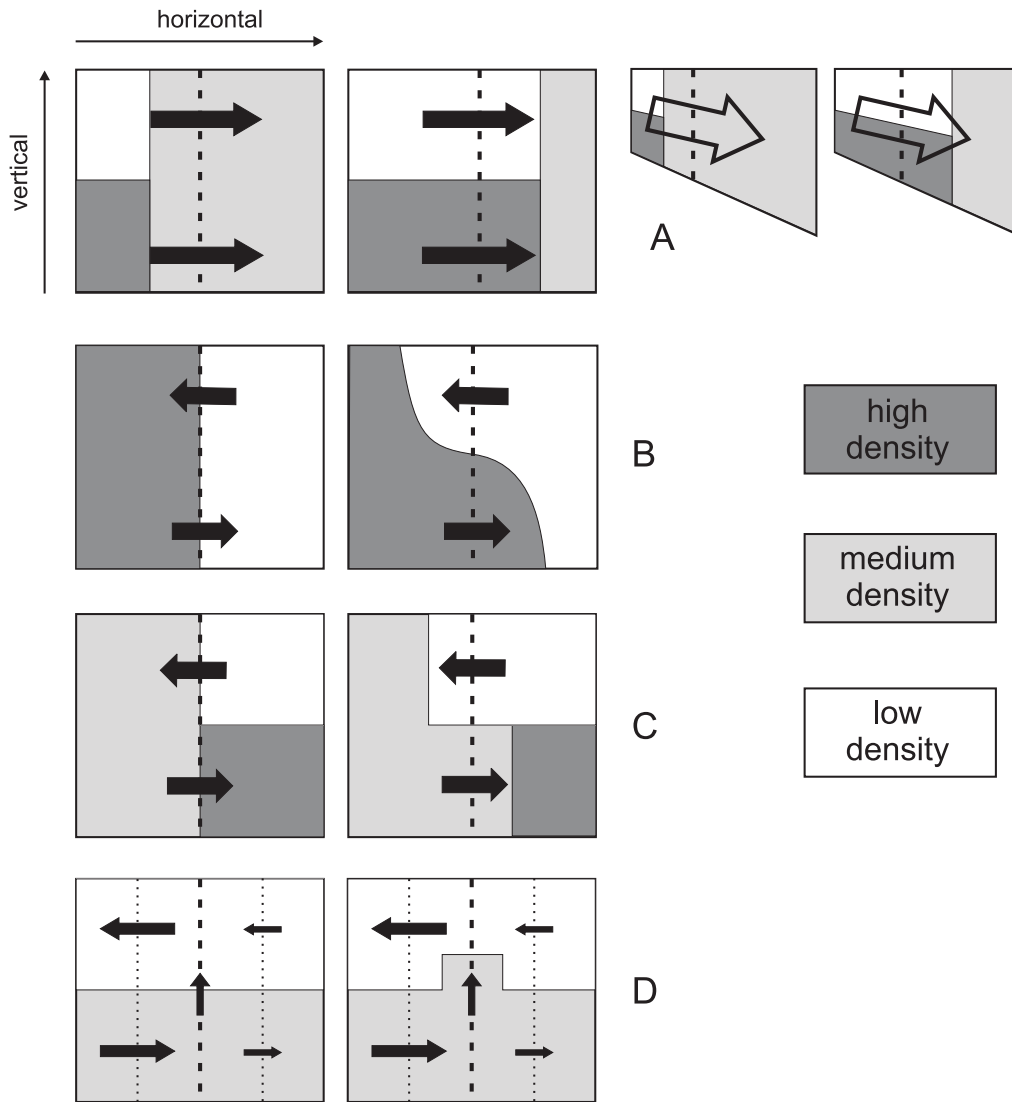


Figure 2.1: Sketch explaining the the principle of how the kinematic terms A - D in equation (2.12) change the potential energy anomaly ϕ . A: horizontal advection of ϕ for flat (upper left) or sloping (upper right) sea bed; B: mean straining; C: non-mean straining; D: vertical advection.

2.1.2 Applications to estuarine flow

2.1.2.1 One-dimensional strain-induced periodic stratification

Here, the dynamics of strain-induced periodic stratification (SIPS, see *Simpson et al.* [1990]) is studied with the one-dimensional model by prescribing a rectilinear tide interacting with a constant wind stress and a constant density gradient, both acting in the direction of the flow. For simplicity, Earth rotation is neglected. With this, the dynamic momentum equation reads as

$$\partial_t u - \partial_z (A_v \partial_z u) = z \frac{g}{\rho_0} \partial_x \bar{\rho} - g p_g(t), \quad (2.16)$$

where the first term on the right hand side represents the effect of the internal pressure gradient and p_g is the surface slope oscillating with period T chosen in such a way that the depth-averaged transport is sinusoidal:

$$\bar{u}(t) = u_{\max} \cos\left(2\pi \frac{t}{T}\right), \quad (2.17)$$

with the vertical mean velocity amplitude u_{\max} (see *Burchard* [1999] for details). In (2.16), A_v denotes the vertical eddy viscosity.

In this one-dimensional case, the transport equation for density is given as

$$\partial_t \rho + u \partial_x \bar{\rho} - \partial_z (K_v \partial_z \rho) = 0, \quad (2.18)$$

with zero density fluxes through surface and bottom.

For the simulation discussed here, the following parameters are used: constant water depth $D = H = 10$ m; tidal period $T = 44714$ s (same as for M_2 tide); tidal velocity amplitude $u_{\max} = 0.5$ m s⁻¹, constant horizontal density gradient $\partial_x \bar{\rho} = -5 \cdot 10^{-4}$ kg m⁻⁴; surface wind stress $\tau_s = 0.1$ N m⁻² (equivalent to a 10 m wind speed of the order of 5 m s⁻¹).

Figure 2.2 shows the resulting density structure, potential energy anomaly ϕ and the balance of the ϕ -equation after 30 tidal periods. After flood ($t/T = 0$ and $t/T = 1$), the water column is vertically fully homogenised, resulting in vanishing ϕ . With the onset of the ebb current ($0 \leq t/T \leq 0.5$), less dense water is sheared over denser water, with an increasingly positive straining term, not fully balanced by vertical mixing, such that ϕ is growing. At the end of the ebb tide ($t/T = 0.4$), the vertical mixing is ceasing, leading to a maximum increase of ϕ . After the onset of flood ($t/T > 0.5$, straining is reversed with the effect of decreasing ϕ . With full flood ($t/T = 0.75$) vertical mixing is supporting the erosion of stratification, resulting in a maximum decrease of ϕ at $t/T = 0.8$, and slightly unstable stratification ($\phi < 0$). With unstable stratification, however mixing is increasing ϕ , such that for the last phase of the flood tide ($0.8 < t/T < 1$) destabilising straining and stabilising mixing are in balance.

2.1.2.2 Comparison to empirical estimates

Simpson et al. [1990] suggested an empirical model for estimating some of the forcing terms in the ϕ -equation. Their model is valid for scenarios with flow and gradients only in one horizontal direction (which is here aligned with the x -direction, with the x -component of the flow velocity denoted as u). For the depth-mean straining term (B) they overlaid an empirical profile for unstratified tidal flow (see *Bowden and Fairbairn* [1952]) with a profile

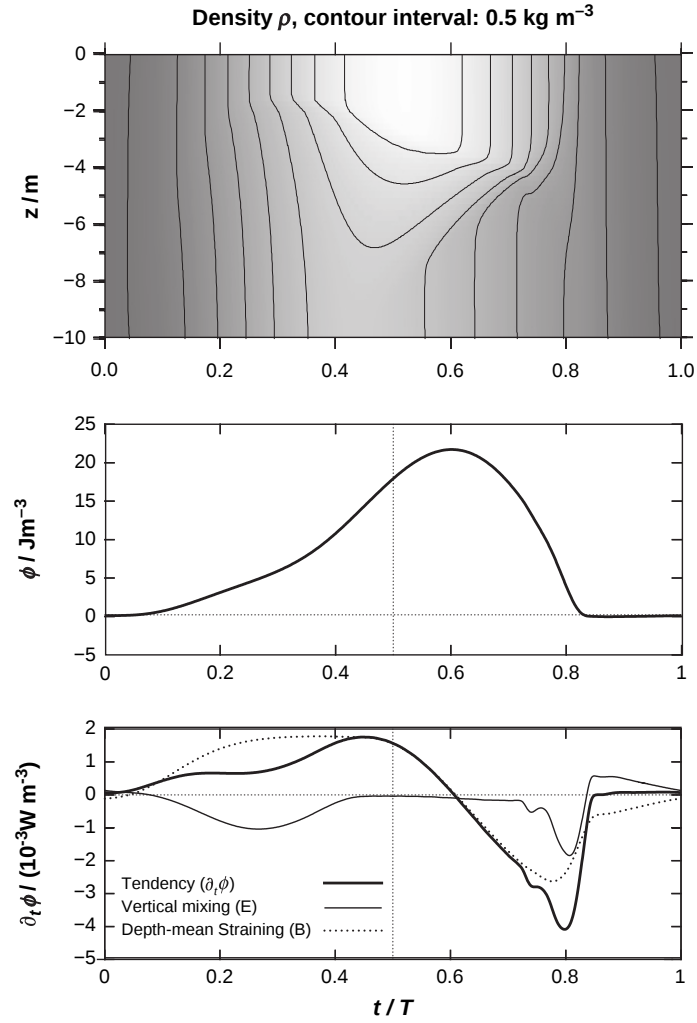


Figure 2.2: Idealised one-dimensional simulation of tidal straining during one tidal cycle. Upper panel: time series of density profiles; middle panel: time series of potential energy anomaly ϕ ; lower panel: time series of the tendency ($\partial_t \phi$), vertical mixing (E) and depth-mean straining (B) terms in the ϕ -equation. There is ebb tide for $t/T < 0.5$ and flood tide for $t/T > 0.5$.

for estuarine circulation derived from analytical theory (see *Officer [1976]*) as estimate for \tilde{u} . With these assumptions, the empirical depth-mean straining term is of the following form:

$$(\partial_t \phi)_B = \left(a\bar{u} + b \frac{gD^3}{\bar{A}_v \rho_0} \partial_x \bar{\rho} \right) gD \partial_x \bar{\rho} \quad (2.19)$$

with the empirical parameters $a = 0.031$ and $b = 0.0031$, and the depth mean eddy diffusivity

$$\bar{A}_v = \gamma |\bar{u}| D, \quad (2.20)$$

see *Simpson et al. [1990]*. In (2.20), γ is an empirical parameter which is estimated here as $\gamma = 0.00333$ (see also *Nunes Vaz et al. [1989]*) by taking the depth average of the parabolic empirical eddy viscosity formulation for channel flow (see e.g. *Fischer et al. [1979]*):

$$A_v = \kappa u_* (-z) \left(1 + \frac{z}{D}\right) = \kappa c_d^{1/2} |\bar{u}| (-z) \left(1 + \frac{z}{D}\right) \quad (2.21)$$

with the bed friction coefficient $c_d = 2.5 \cdot 10^{-3}$, the von Kármán number $\kappa = 0.4$ and the bed friction velocity, u_* . In order to prevent the estuarine circulation part of (2.19) from increasing towards infinity for slack tides, a lower background limit for \bar{A}_v has been prescribed as one tenth of the maximum value.

The mixing term has been estimated by *Simpson et al.* [1990] as

$$(\partial_t \phi)_E = -c_d \Gamma \rho_0 \frac{|\bar{u}^3|}{D} \quad (2.22)$$

with the bulk mixing efficiency Γ . Here we use $\Gamma = 0.04$, which means that 4 % of the turbulent kinetic energy produced in the entire water column is used for vertical mixing (increasing the potential energy) and 96 % are dissipated into heat. Given that a typical local mixing efficiency is 20 % for stratified flow (*Osborn* [1980]) and that unstably or neutrally stratified situations (with negative or zero mixing efficiencies) are present at times, a bulk mixing efficiency of 4 % seems reasonable. This is by a factor of 10 larger than the value chosen by *Simpson et al.* [1990] who used estimates from mixing in shelf seas which are substantially deeper than the 10 m deep test case considered here and where mixing is probably is much less efficient due to the typically well-mixed bottom boundary layer. Thus, the bulk mixing efficiency may be considered as an adjustable parameter which may be estimated by means of comparing $(\partial_t \phi)_E$ from (2.22) and the mixing term E in (2.12).

Wind mixing, although included in our simulations discussed in section 2.1.2.1, is not considered for this comparison, since it is here hardly contributing to changes in ϕ . Nonetheless, in order to roughly separate mixing in the surface (SBL) and in the bottom boundary layer (BBL), we have estimated the height of the SBL by finding at each time the highest local minimum of the turbulent kinetic energy (TKE) and defining this location as the lower bound of the SBL. The tidal mixing part of term B in the ϕ -equation has then been defined as the integral of the buoyancy flux G from the bottom to the lower bound of the SBL, thus excluding wind mixing.

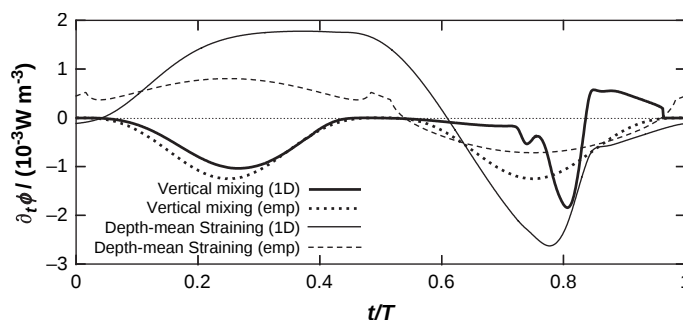


Figure 2.3: Comparison between forcing terms in the ϕ -equation as calculated from the one-dimensional model discussed in section 2.1.2.1 (full lines) and as estimated from the empirical model suggested by *Simpson et al.* [1990] (dashed lines). The bold lines show the vertical mixing term (E) and the thin lines show the depth-mean straining term (B).

Figure 2.3 shows a comparison between the straining and mixing terms of the ϕ -equation computed from the one-dimensional model in section 2.1.2.1 and as estimated from the em-

pirical model given in the equations (2.19) and (2.22). It can be seen that there is good agreement for the straining term between the empirical and the resolved model only during late flood when stratification is weak. During full ebb ($t/T = 0.25$) and full flood ($t/T = 0.75$) straining is underestimated by the empirical model, because the modification of the velocity profiles due the tidal mixing asymmetry (enhanced mixing during flood and suppressed mixing during ebb due to tidal straining, see *Jay and Musiak* [1994]), is not considered. The mixing terms of the resolved and the empirical model are in quite good agreement for ebb ($0 < t/T < 0.5$). However for flood, the agreement is poor, in the first half of the flood ($0.5 < t/T < 0.75$) due to a time lag between mixing and flow velocity represented only in the resolved model and around the end of the flood ($0.8 < t/T < 0.95$) due to the fact that most of the mixing acts on unstable stratification in the resolved model, such that the effective bulk mixing efficiency becomes negative. The mixing term may be parameterised in a more realistic way by using a formulation with the mixing efficiency varying with the value of ϕ (see *Simpson and Bowers* [1981]).

2.1.2.3 Two-dimensional estuarine dynamics

For studying the impact of ϕ -advection (term A in (2.12)), the non-mean straining (term C in (2.12)) and vertical advection (term D in (2.12)), which are all not included in the one-dimensional simulations of section 2.1.2.1, we carry out a two-dimensional simulation along an idealised estuary. This scenario is a slight modification of the idealised estuarine used by *Warner et al.* [2005] for comparing various turbulence closure schemes. The length of the estuary is 100 km, the depth is linearly decreasing from the open boundary at the river mouth at $x = 0$ km (depth: 15 m) to the riverine boundary at $x = 100$ km (depth: 10 m). Earth rotation is neglected. The horizontal resolution is $\Delta x = 500$ m, and 20 equidistant σ layers are used in the vertical. The timestep is $\delta t = 20$ s for the barotropic mode (explicitly calculated free surface) as well as for the baroclinic mode, including the rate of change of potential energy and its contributions. As initial conditions, we chose the same setup as *Warner et al.* [2005], with a vertically homogeneous salt distribution, with a salinity of 30 for $x \leq 30$ km, a salinity of 0 for $x \geq 80$ km and decreasing linearly from 30 to 0 in between. As boundary conditions, we prescribe a salinity of 30 at $x = 0$ and a freshwater runoff at the river boundary with a velocity of 0.01 m s^{-1} . At the open boundary, we further prescribe a sinusoidal semi-diurnal tide with a sea surface elevation amplitude of 1 m, resulting into a horizontal velocity amplitude of about 1 m s^{-1} near the open boundary. Meteorological forcing is not considered. In order to allow for complete destabilisation of the water column due to tidal straining at the end of the flood in parts of the estuary, the present scenario deviates from the *Warner et al.* [2005] idealised estuary by increased the tidal forcing and depth and decreased freshwater inflow.

The simulation was carried out for 8 days. After about 5 days, a periodic steady state is reached, with a salt wedge moving up and down the estuary with the tide, see the snapshot at the end of ebb in figure 2.4.

The dynamics of the potential energy anomaly is examined at two locations with different characteristics: at $x = 38$ km (position A), where the SIPS mechanism fully destabilises the water column during flood and at $x = 80$ km (position B), where the water column is strongly stratified during the whole tidal period.

At position A, the dynamics is comparable to the situation simulated with the one-dimensional model in section 2.1.2.1. The only terms playing a significant role are the depth-mean straining and the vertical mixing, see figure 2.5. After the end of ebb, ϕ has a maximum, which

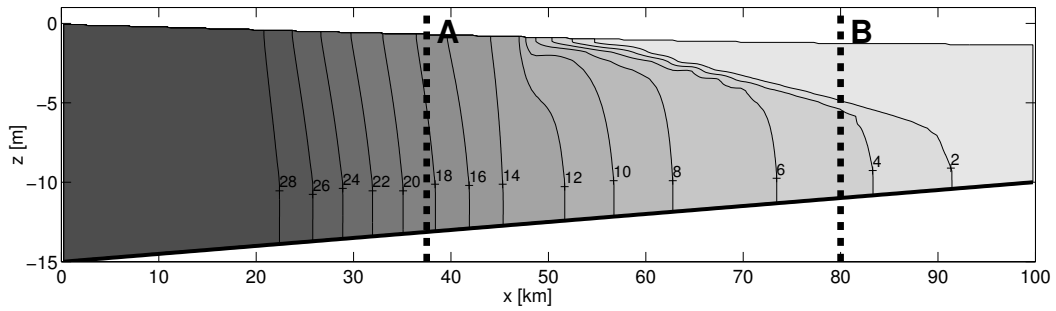


Figure 2.4: Salinity distribution in the idealised estuarine near the end of ebb. The sections A and B indicate the two positions at which time series of ϕ and the terms in the ϕ -equation have been extracted, see figure 2.5.

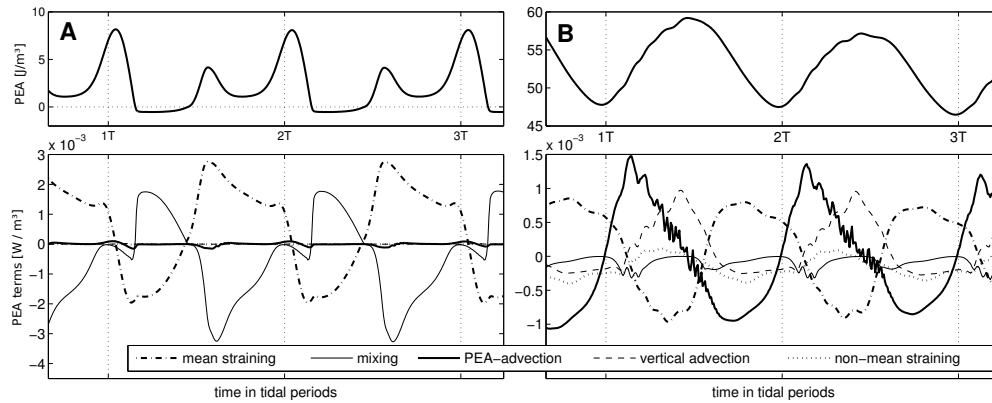


Figure 2.5: Time series of ϕ (upper panels) and the terms in the ϕ -equation (lower panels) for the locations indicated in figure 2.4. The terms shown in the lower panel are the depth-mean straining (term B in (2.12)), vertical mixing (term E in (2.12)), PEA-advection (term A in (2.12)), vertical advection (term D in (2.12)), and non-mean straining (term C in (2.12)). The vertical dotted lines roughly indicate the end of the ebb flow.

is then steeply eroded by both, depth-mean straining and mixing, such that at full flood the water column becomes unstably stratified. Here, in contrast to the one-dimensional study, a local maximum of ϕ is visible around the slack water after flood, showing that here estuarine circulation is more effective than in the one-dimensional model. A similar intensification of the stratification maximum after slack tide flood has been observed by *Burchard et al.* [2008] for a three-dimensional model simulation in the Wadden Sea if horizontal density gradients are considered. A small contribution of ϕ -advection is also visible for location A.

At location B, the balance of the terms in the ϕ -equation is completely different. Here, the major balance is between the ϕ -advection, the vertical advection and the depth-mean straining. Smaller contributions come from vertical mixing and non-mean straining. After ebb, ϕ has a minimum value, since the salt wedge, the maximum extent of which is always upstream of location B, has a minimum thickness at minimum density. After the onset of flood, ϕ -advection strongly forces stabilisation of stratification, however, depth-mean straining is opposing to it, similarly to the situation at location A. With increasing flood current,

the vertical advection is stabilising the flow as well, due to a rise of the main halocline. At slack tide after flood, ϕ has a maximum value, which is then mainly reduced by ϕ -advection, again opposed by depth-mean straining. The significant role of the non-mean straining is explained here by the fact that the horizontal density gradient is substantial inside the salt wedge, but negligible in the near-surface waters.

2.1.3 Summarising: The dynamic equation for the PEA

With the time-dependent dynamic equation for the potential energy anomaly, ϕ , which has been rigorously derived here from the dynamic equations for potential temperature and salinity, the continuity equation and the equation of state for sea water, we have now provided a complete reference solution for all empirical model parameterisations. The physical basis which has been used here is sufficiently general for including most of the processes relevant for estuaries and coastal seas. The major approximation on which the dynamic equations for potential temperature and salinity are based on is the Reynolds averaging of state variables leading to the definition of turbulent fluxes. The down-gradient approximation for these turbulent fluxes applied here has been included for convenience since it is used in most coastal models, but a general formulation of the turbulent salt and heat fluxes could be considered in a straight-forward way. A number of thermodynamic approximations has been made as well, commonly summarised as the Boussinesq approximation. Some of these idealisations could also be relaxed and included into the ϕ -equation. With the ϕ -equation, we have now a tool for completely quantifying the processes of mixing and stratification from numerical model simulations.

In realistic estuarine and coastal scenarios, all terms in the ϕ -equation will be present, but typically the major local balance will be based on a few terms only. It is however clear from the two-dimensional estuarine scenario discussed in section 2.1.2.3 that completely different regimes may be spatially located close to each other, each with a different balance of terms. Regimes may also change in time (e.g. seasonal cycle, spring-neap cycle) and with this also the balance of terms in the ϕ -equation.

Great effort has been made by many studies to find empirical estimates for various processes leading to depth-mean straining (term B) and vertical mixing (term E), for which the ϕ -equation provides only one term each. Depth-mean straining is divided into estuarine circulation (asymmetric) and tidal straining (symmetric for ebb and flood), see equation (2.19). It should in principle be possible in numerical model studies to separate tidal flow velocity profiles into symmetric and asymmetric parts in order to improve the empirical estimates for depth-mean straining, but wind, Earth rotation and non-rectilinear tides would complicate this. Although rotational effects are not directly included in the ϕ -equation, they have an indirect impact on the stability of the water column through the advection and straining terms. This has been demonstrated by *Rippeth et al.* [2001] in their field observations of transverse straining in Liverpool Bay due to Coriolis acceleration, see also the numerical simulations by *Simpson et al.* [2002].

Due to non-linear interactions, similar problems would arise for numerically separating influences of wind, tides, surface cooling and waves on vertical mixing. An attempt to do so has been demonstrated in section 2.1.2.2 where wind mixing was assumed to be the part of mixing which takes place in the surface mixing layer, defined by the depth range above the highest TKE minimum in the water column. This worked fine for constant wind stress, but for highly varying wind stress and simultaneous impact of surface waves and surface cooling, these impacts can practically not be separated. This means that for realistic flow

situations empirical estimates of mixing will be inaccurate and that the model-based mixing impact on stratification as given by the potential energy anomaly has to be limited to term E , the vertically integrated vertical buoyancy flux.

The PEA equation can also be used for relating the local processes of mixing and stratification to the energetics of a whole marine system by laterally integrating the equation. Following, e.g., the concept of *Winters et al.* [1995], the available potential energy (APE) budget can be related to the PEA equation terms.

2.2 Evaluating stratification and mixing in the Limfjord

Here we present a validated three-dimensional numerical model for the Limfjord which provides a high-resolution hindcast study for the year 2003. We will use the dynamic equation for the PEA from *Burchard and Hofmeister* [2008] to evaluate the processes of stratification and de-stratification for the scenario already studied by *Wiles et al.* [2006].

2.2.1 Methodology

Here we simulate the dynamics of the Limfjord in the year 2003 with the General Estuarine Transport Model (GETM). We use the k - ε turbulence model coupled to a second-moment closure by *Cheng et al.* [2002] (see *Umlauf and Burchard* [2005]). The Limfjord model was set up with a Cartesian horizontal grid using a horizontal resolution of 200 m. All the narrow channels within the domain of about 650x360 gridpoints are resolved with at least a few gridpoints in cross-channel direction. The barotropic time step is 4 seconds, whereas the baroclinic mode is integrated with a time step of 80 seconds. In the vertical, bottom-fitted general vertical coordinates with a discretisation into 10 vertical layers have been used (see *Burchard and Bolding* [2002]). The model setup was divided horizontally into 16 model domains which are distributed on a cluster computer with 8 processors for parallel computation.

The open lateral boundaries in the Limfjord model are narrow channels with a connection to the North Sea at the western side and a connection to the Kattegat at the eastern side (see Fig. 2.6). Hourly observed data for the sea surface elevation from the boundary channels are used at the open boundaries in the model. The temperature and salinity data at the open boundaries are available from observations every three hours and are included as depth-mean values. They are linearly interpolated in time also for periods with gaps in the observational data.

The initial temperature on 1st January, 2003 was set to 3 °C for the whole 3D-field as suggested by observations. The temperature adjusts within the first weeks of January, 2003 by radiation, heat flux and wind mixing of the whole water body in the winter times in the shallow waters of the Limfjord. For the initial salinity distribution vertically mixed conditions with horizontally variations were assumed. The observations at the monitoring stations in the Limfjord show for winter conditions that the salinity reaches from 31 psu in the very western part of the Limfjord down to salinities around 20-23 psu in the central and eastern parts. Therefore, the initial salinity was set to 22 psu in the central (Løgstør Bredning) and eastern parts of the Limfjord, increasing westward of Løgstør Bredning linearly to 31 psu at the western open boundary. The initial surface elevation is set to zero for the whole Limfjord.

As meteorological forcing, model data from the German Weather Service Local Model (DWD-LM) were used. These data contain air temperature, dew point temperature, humidity and air pressure 2 m above sea surface, and the wind velocity vector 10m above sea surface.

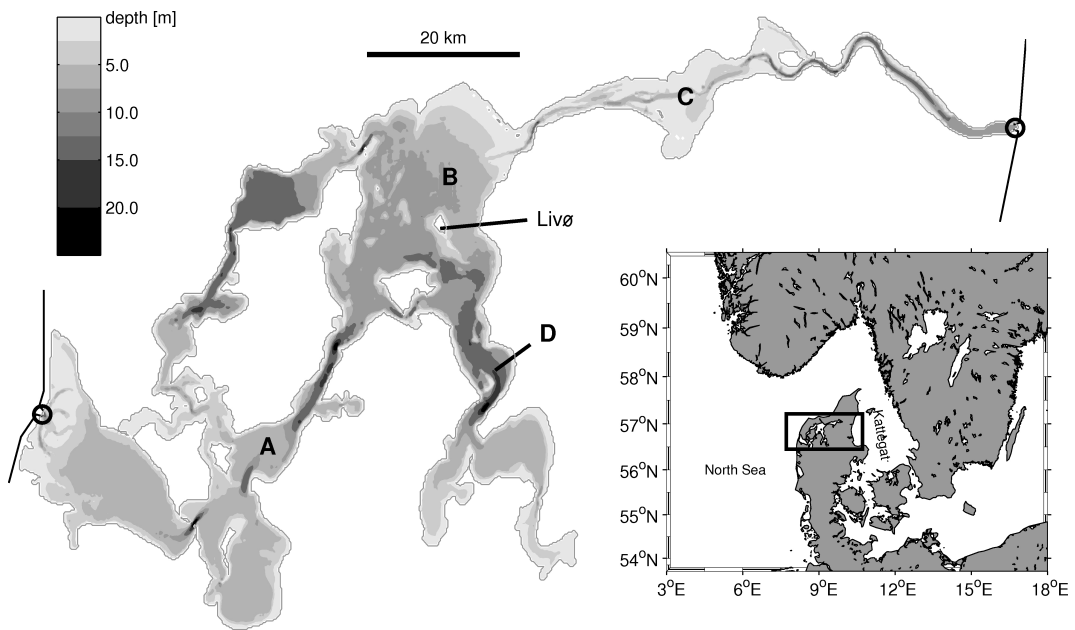


Figure 2.6: The bathymetry of the Limfjord, its location and some monitoring sites: A - Kås Bredning, B - Løgstør Bredning, C - Nibe Bredning, D - Risgårde Bredning. The circles denote the open boundaries of the model.

The time interval of these data is 3 hours. The fluxes of momentum and heat in the meteorological forcing are calculated from the meteorological data by using the bulk formula of *Kondo* [1975]. The meteorological forcing is only extrapolated constant in space from a data point located near the island of Livø (see Fig. 2.6), in the central basin of the Limfjord, into the model domain. Since observed sea surface heights are used at the Limfjord's boundaries, which include the external wind effect, the constant local forcing should lead to small errors only in this local model with a horizontal scale of 130 x 70 km. A comparison of the forcing data out of the meteorological model and measurements during a campaign at the end of May, 2003, shows a good agreement (shown in *Hofmeister* [2006]).

In the Limfjord model, freshwater runoff data from the local authority, Nordjyllands Amt, have been used. These are observed monthly runoff data for 30 catchment areas, covering the coast of the Limfjord. There are many small rivers along the coast giving a more diffuse freshwater inflow into the Limfjord. In the model, 45 individual rivers are defined. The region of the Limfjord which stretches southward from Risgårde Bredning (see Fig. 2.6) receives the largest fraction of freshwater input compared to the rest of the Limfjord.

Since the mussel producing area is located in the northern central basin, the whole study is focussed to Løgstør Bredning. The model has been adjusted slightly in bathymetry and boundary forcing in order to get realistic volume and salt fluxes into the central basin. Discretisation errors in the resistance of the very narrow channels are balanced with a small, artificial external pressure gradient imposed by the prescribed surface elevations at the boundaries.

2.2.2 Model validation and results

In order to verify the model results, monitoring measurements along the way from the North Sea to the Kattegat are used. As validation for sea surface height, observed data for Løgstør

Bredning are compared to the model results (see Fig. 2.7). These are dominated by subtidal variations at that location. The simulated sea surface height closely follows the observations with a correlation coefficient of 0.964. The scatter plot (Fig. 2.7) is located around equality with a standard deviation of 7.53 cm between both time series.

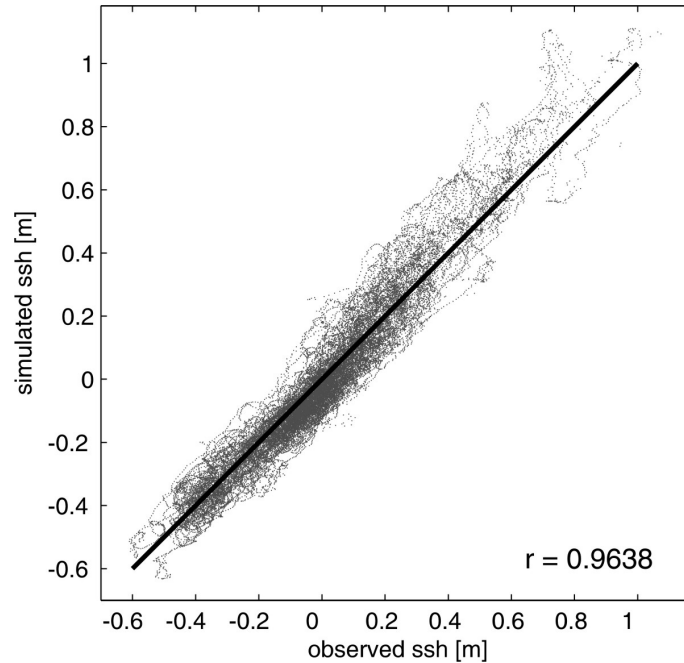


Figure 2.7: Scatter plot of centred time series of simulated and observed sea surface height (ssh) in Løgstør Bredning for the whole year 2003. The correlation of both time series gives a correlation coefficient of 0.9638.

Fig. 2.8 shows comparisons of observed and simulated bottom and surface salinity and temperature in the western (Kås Bredning, site A in Fig. 2.6), central (Løgstør Bredning, site B in Fig. 2.6) and eastern (Nibe Bredning, site C in Fig. 2.6) Limfjord, respectively. In general, the monitoring intervals for salinity and temperature are too long to validate the temporal variability of the results quantitatively. But the comparison shows that the simulated salinity has the same magnitude and trend as the observed salinity. The observed major events are represented by the model at least qualitatively. In March and around 1 July, significant discrepancies between the model results and the observations occur. In both cases the discrepancies are due to gaps in the boundary conditions and are recovered by the simulation within two weeks. The salinity is underestimated at the beginning of March at both open boundaries and overestimated around the 1 July at the North Sea side. The simulated sea surface temperature (shown for Løgstør Bredning) follows the observations close to perfect in all locations.

Fig. 2.9 shows the vertically resolved salinity over depth for the whole year 2003 at the monitoring station in Løgstør Bredning (see Fig. 2.6). The simulated salinity is in good agreement with the measured salinity. The observed events and trends are reproduced in the simulation, except during the three weeks around the 1 July. The modelled bottom salinities seem to lack the event of a drastically decreasing salinity in Kås Bredning before the 1 July (see Fig. 2.8) which results in the high bottom salinity in Løgstør Bredning. This discrepancy is recovered in the simulation already in the middle of July. The rms-differences of modelled salinity and

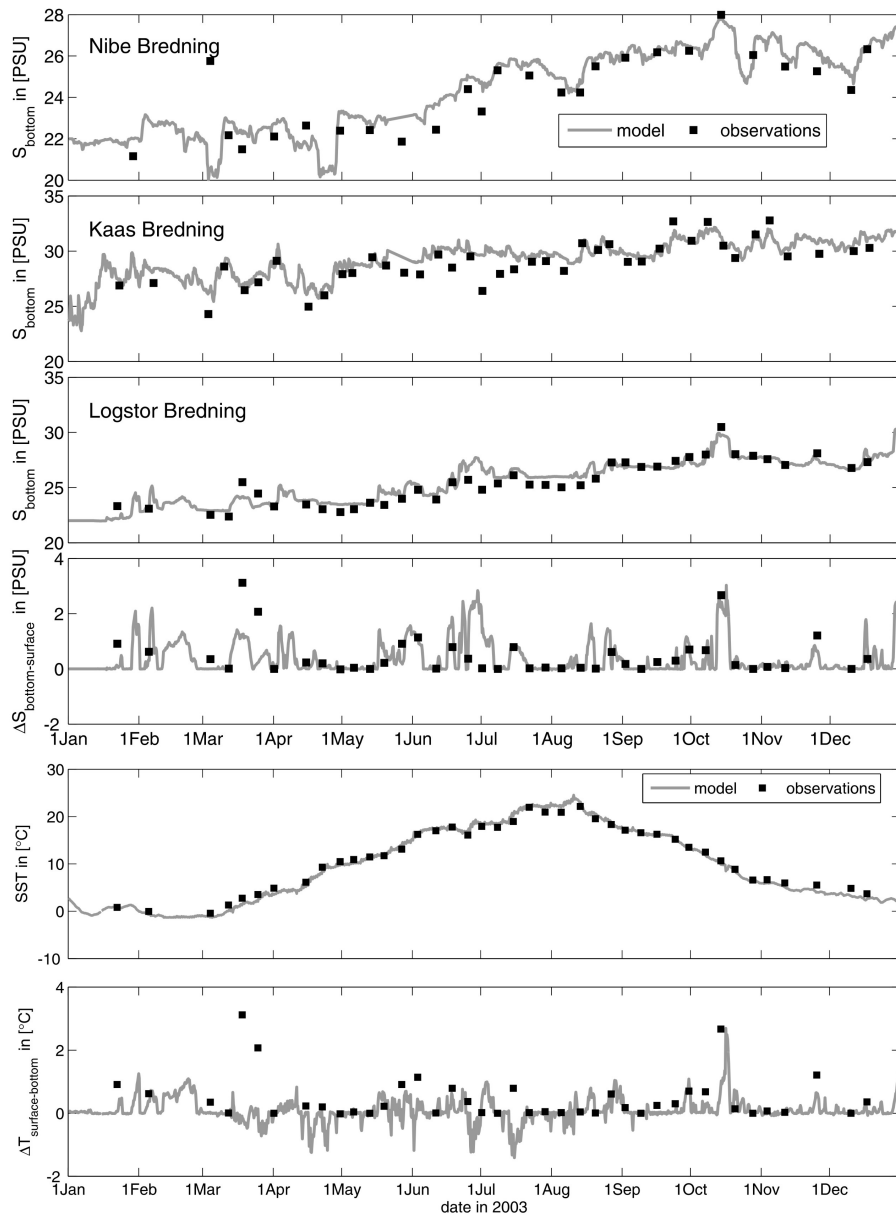


Figure 2.8: Comparison between modeled (line) salinity and the observations (dots) for the monitoring stations A-C from Fig 2.6 for the year 2003 in the upper 3 panels. The fourth panel shows the same comparison for the bottom to surface salinity difference for the central Limfjord (Løgstør Bredning, station B). The lower 2 panels show comparisons of the modeled and observed temperature and surface to bottom temperature difference for the central Limfjord.

observed salinity for Løgstør Bredning is 0.68 psu for the salinity at the sea bed and 0.52 psu at the sea surface.

In Fig. 2.10, the salinity distribution at the bottom during the year 2003 is plotted as monthly snapshots. The central basin shows a permanent horizontal salinity gradient of several psu between the south-western and the north-eastern entrance. The salinity in the central basin is increased by inflows through the deep and relatively broad, south-western connection. There are no saline inflows through the narrow, northern connection to the western Limfjord. The

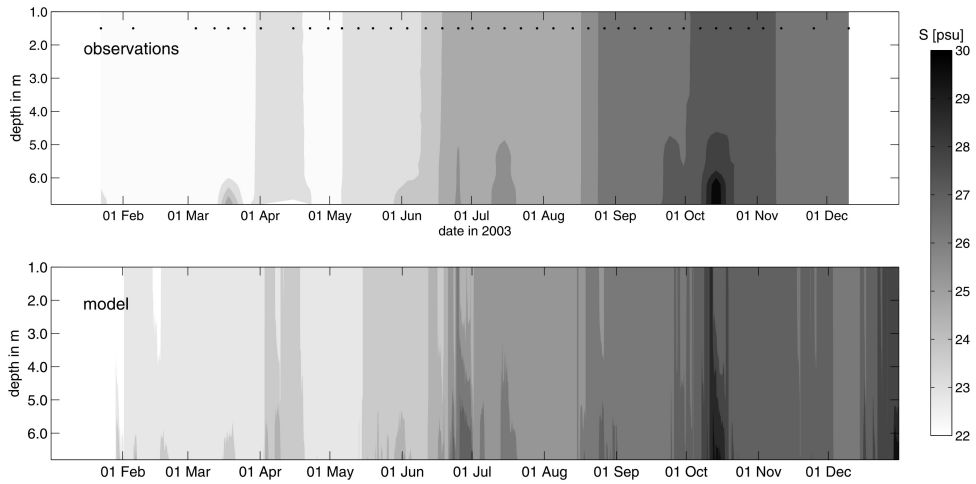


Figure 2.9: Vertical, modeled and measured salinity profiles for the year 2003 at the monitoring station in Løgstør Bredning. Dots in the upper panel denote the time of profiling.

gradient occasionally sharpens and builds a front in Løgstør Bredning (for example in March, June, August, October). A comparison with Fig. 2.9 shows that an inflow, which increases stratification, occurred in these months. Almost all parts of the Limfjord become more saline over the year 2003, which is due to the dry year 2003 and thus relatively weak freshwater supply.

2.2.3 Stratification in the Limfjord

The potential energy anomaly is used as the measure for stratification. *Simpson et al.* [1977] (see also *Simpson and Bowers* [1981]) define the anomaly of potential energy as

$$\phi = \frac{1}{D} \int_{-H}^{\eta} gz (\bar{\rho} - \rho) dz \quad (2.23)$$

with the depth-mean density

$$\bar{\rho} = \frac{1}{D} \int_{-H}^{\eta} \rho dz, \quad (2.24)$$

where g is the gravitational acceleration, z is the vertical coordinate (positive upwards from the bottom $-H$ up to the sea surface η), $\rho(z)$ is the density profile in a water column of depth $D = H + \eta$. The PEA, ϕ , is zero for a fully mixed water column, positive for stable stratification and negative for unstable stratification. Physically, ϕ gives the amount of energy per volume that is necessary to vertically homogenise the entire whole water column.

When inspecting the temporal distribution of the simulated PEA, especially in Løgstør Bredning, it can be seen that the Limfjord is an area where mixed and stratified periods are alternating. Fig. 2.11 shows the simulated and measured PEA for the whole year at the monitoring station in Løgstør Bredning together with the oxygen saturation (discussed later). The simulated PEA time series for 2003 is correlated to the simulated salinity difference of surface and near-bed salinity time series for 2003 with a correlation factor of 0.96 at the monitoring station. This is characteristic for estuaries and shows for the present study that the number of

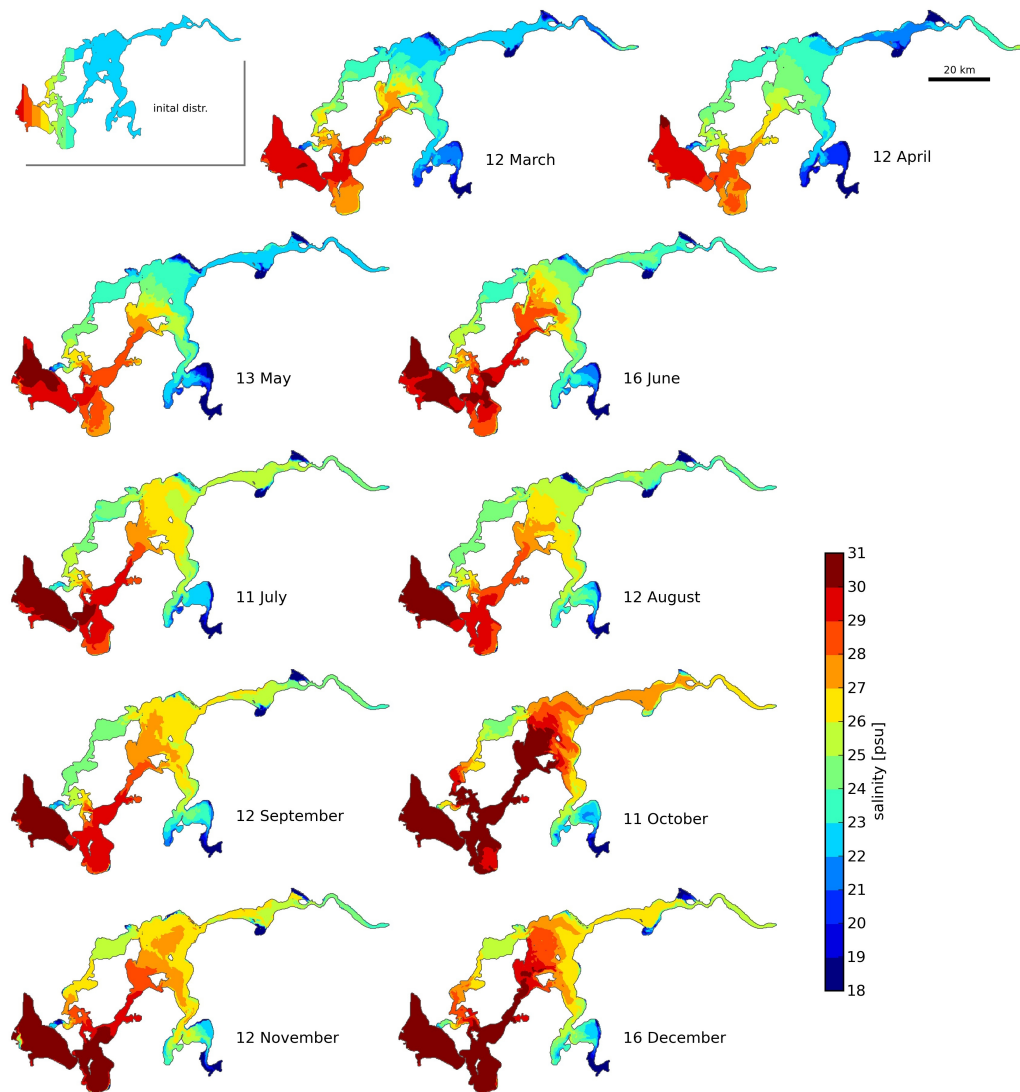


Figure 2.10: Monthly snapshots of the simulated bottom salinity in the Limfjord for the year 2003.

stratification events concentrating in June/July 2003, when the solar radiation is at maximum, is not primarily related to an increasing temperature stratification. The effect of temperature will be discussed below when analysing the heating influence on the PEA. The simulated PEA may be overestimated at the end of June 2003, which is due to the differences between the simulated salinity and observations in the short period (described above). Fig. 2.12 shows the annual mean potential energy anomaly for 2003, calculated from the model results. Most of the modeled stratification of 2003 occurs in the deep areas around Risgårde Bredning and the attached south-eastern bays. The relatively high cumulating freshwater input in that region increases the mean stratification. Additionally, the wind mixing efficiency in these deeper parts of the Limfjord is not as high as in the shallow parts, simply due to the water depth.

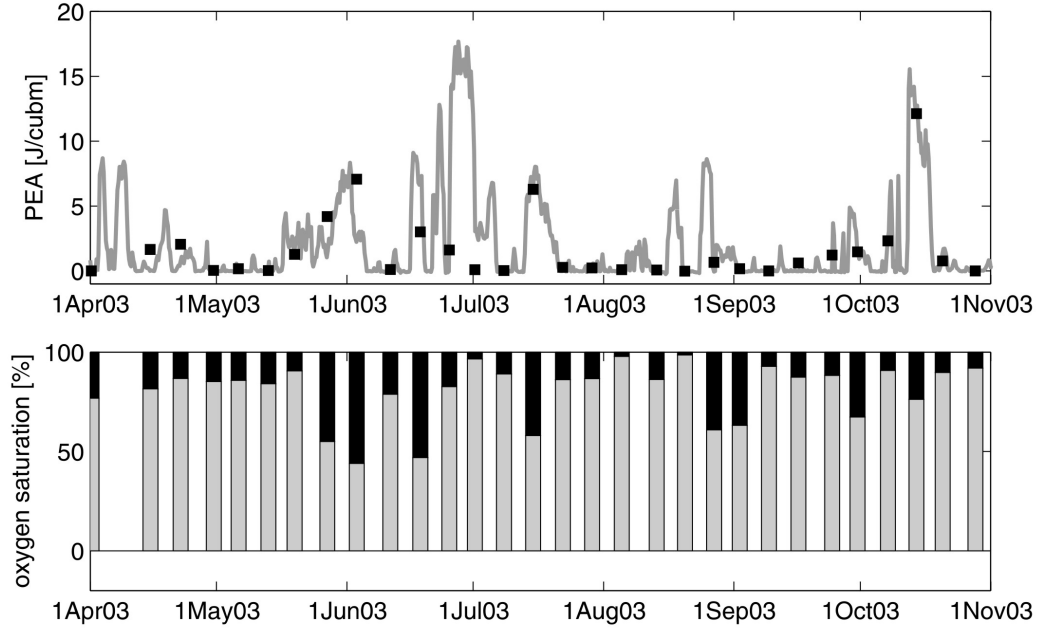


Figure 2.11: Comparison of measured (squares) and modeled (line) PEA in the upper panel and oxygen saturation near the bed in the lower panel for the period April to October 2003. The black part of the bars in the lower panel denotes the oxygen depletion.

2.2.3.1 The processes of stratification and de-stratification according to the dynamic equation of PEA

For analysing processes of stratification and de-stratification in the Limfjord, the dynamic PEA equation derived by *Burchard and Hofmeister* [2008] is used here. After omitting terms due to bottom buoyancy fluxes and horizontal mixing, the PEA equation is of the following form:

$$\begin{aligned}
 \partial_t \phi = & \underbrace{-\nabla_h(\bar{\mathbf{u}}\phi)}_{(A)} + \underbrace{\frac{g}{D}\nabla_h\bar{\rho}\cdot\int_{-H}^{\eta}z\tilde{\mathbf{u}}dz}_{(B)} \\
 & - \underbrace{\frac{g}{D}\int_{-H}^{\eta}\left(\eta-\frac{D}{2}-z\right)\tilde{\mathbf{u}}\cdot\nabla_h\tilde{\rho}dz}_{(C)} \\
 & - \underbrace{\frac{g}{D}\int_{-H}^{\eta}\left(\eta-\frac{D}{2}-z\right)\tilde{w}\partial_z\tilde{\rho}dz}_{(D)} \\
 & + \underbrace{\frac{\rho_0}{D}\int_{-H}^{\eta}P_bdz}_{(E)} - \frac{\rho_0}{2}(P_b^s) + \underbrace{\frac{g}{D}\int_{-H}^{\eta}\left(\eta-\frac{D}{2}-z\right)Qdz}_{(F)}
 \end{aligned} \tag{2.25}$$

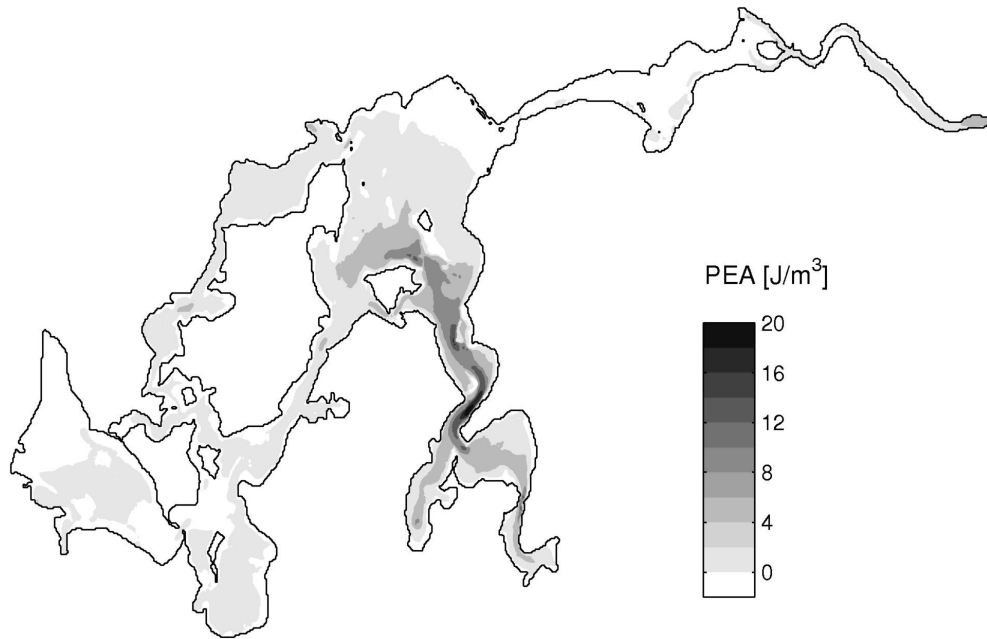


Figure 2.12: The simulated annual mean PEA for the Limfjord for the year 2003.

using the the depth-mean velocity vector $\bar{\mathbf{u}}$ and the deviation from the depth-mean velocity vector, defined as $\tilde{\mathbf{u}} = \mathbf{u} - \bar{\mathbf{u}}$ and the deviation of the depth-mean-density $\tilde{\rho}$, with ∇_h denoting the horizontal gradient operator. Here, $\tilde{w} = w - \bar{w}$ is defined as the deviation from a linear vertical velocity profile interpolation \bar{w} between the kinematic boundary conditions at the surface and the bottom, as derived in *Burchard and Hofmeister* [2008]. The linear vertical velocity profile fulfils the continuity equation of the depth-mean horizontal velocities. Further, P_b is the vertical buoyancy flux, P_b^s the surface buoyancy flux and Q is the source term for density due to heating by absorption of light. For simplicity, a linear equation of state was used to avoid contributions from the non-linearity of the equation of state by diffusion of temperature and salinity as a source for density. The processes of stratification and destratification according to (2.25) are A: advection of PEA, B: depth-mean straining, C: non-mean straining, D: vertical advection, E: vertical mixing and F: heating due to short-wave radiation and surface heat fluxes.

The PEA-analysis focuses on the central basin and the period 27 May to 6 June which was investigated in *Wiles et al.* [2006]. Fig. 2.13 shows a time series of the PEA and its six terms reproduced by the model. Within the model applied here, it cannot be distinguished between mixing by tides or wind mixing. The PEA in the central basin increases up to the 31 May (day 150) in the year 2003 in accordance with *Wiles et al.* [2006] (see Fig. 2e and Fig. 7b in their publication). The calculated PEA terms show a mixture of all above mentioned processes with having similar order of magnitudes. The numerical calculation of the PEA terms is realised here with central differences in the discrete model grid, which is a numerical approximation of the PEA terms as implicitly calculated by the model. Therefore, the difference between the sum of the PEA terms and the total change of the PEA is about 10-15% at the discussed locations.

In Fig. 2.13, the non-mean straining, the advection of PEA and the vertical advection show a high variability, depending on the strength of stratification. When the stratification is stronger, then a change in the PEA by vertical displacement of the pycnocline or the horizontal movement of the stratified regime is supported. Additionally, the occurrence of horizontal density gradients varying with depth is enhanced, so that the non-mean straining is supported in stratified situations (see *Burchard and Hofmeister [2008]* for an illustration of the process). The variability of the mean straining term does not show a dependence of stratification. The heating term shows a diurnal period overlaid by effects from surface cooling and long-wave back-radiation. There is a positive contribution of the mixing term at night which indicates instable stratification and can be tracked back to the night-time surface cooling. The mixing contributes to a reduction of PEA in the showed period mostly due to wind. Mixing due to bottom friction is not expected to be important because of low flow velocities less than 10 cm/s. Fig. 2.13 shows negative rates for the mixing term, when the wind speed exceeds roughly about 5 m/s (at this specific location and time) and the wind induced mixing reaches the pycnocline.

At times when the water column is almost completely mixed and mainly heating and mixing are active (e.g. the night between 5 and 6 June), the instable stratification by night-time surface cooling is compensated by convective mixing. The only remainder for the dynamic terms in this vertically mixed regime with a mean horizontal density gradient is a small contribution from the depth-mean straining.

A cumulative analysis for a better understanding of the contributions of the different PEA terms to the stratification has been done for two locations in the central basin of the Limfjord. Fig. 2.14 shows mean total change of the PEA in the period from 27 May to 2 June, 2003, in the the central basin Løgstør Bredning. The colours are overlaid with the directions of the time-averaged, vertically integrated transports. In that specific period, the PEA is increasing from about 0 up to a value about 6 J/m^3 in the period shown in Fig. 2.13. The whole waterbody is slowly moving from the south-eastern opening (higher salinities) through Løgstør Bredning, slowly transporting salty water into and through the basin. Additionally to the monitoring station B, which is labelled L1 in Fig. 2.14, a second station L2 is added near the south-eastern opening. Location L2, 7.8 m deep, is subject to substantial increases of stratification in the investigated period. It is also directly influenced by the dynamics at the opening, where the salty water enters into the central basin from the North Sea side.

At location L1, Fig. 2.15 shows the PEA terms from Fig. 2.13 integrated from 27 May. The total contributions of the different terms can be found at the end of the integrated time series. The mixing and the advection of PEA do not show a mean contribution to the stratification at 2 June. For both straining terms as well as for the vertical advection the result shows positive contributions as stratifying agents in the specific situation. A contribution against stratification turns out to come from the heating effect. The surface cooling at night as well as the long-wave back radiation do compensate the stratifying effect of light absorption in the daytime. A diurnal cycle of warming and stratification is overlaid with a mean de-stratifying cooling effect. During the whole period, both of the straining terms do have a positive trend in their stratifying effect.

The location L2 shows a completely different situation (see Fig. 2.16). The heating and the non-mean vertical advection do not have a significant integrated effect. Whereas the mixing due to higher velocities (up to 30 cm/s) near the opening de-stratifies the water column. Again, both straining terms do have positive contributions to the stratification. The advection of PEA seem to trigger the temporal PEA evolution until 30 May. A significant

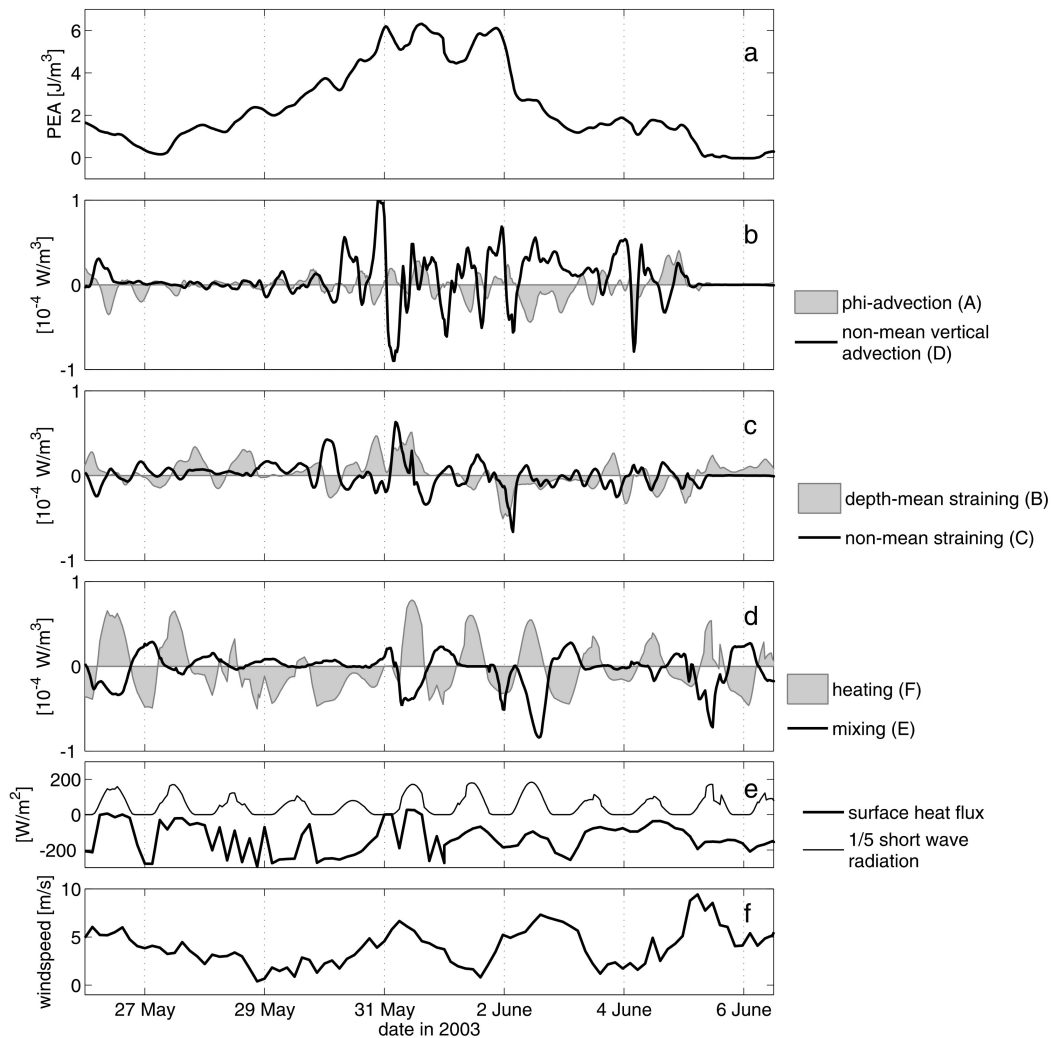


Figure 2.13: The different terms in the dynamic equation of the PEA for the days 27 May to 6 June in the year 2003 in the central basin of the Limfjord. Panel a shows the temporal evolution of the PEA and panels b,c,d below show rates of the PEA due to the different contributors in the dynamic equation (2.25). The panels e and f show the surface heat flux, the short wave radiation (scaled) and the wind speed as used in the model forcing.

de-stratification in panel a in Fig. 2.16 is always seen in the PEA advection term at location L2 until 30 May. A PEA-advection event occurs at 30 May which remains for the whole period as one of the main de-stratifying processes.

Both locations in Fig. 2.14 do show positive mean contributions from the straining terms. The wind event at the 31 May (see Fig. 2.13) can be identified in both locations in the mixing time series. Heating of the water column in terms of definition in (2.25) does not have a mean stratifying effect. It more likely de-stratifies the water column by surface cooling.

2.2.3.2 Some aspects of stratification in the central basin

The tidal signal inside the Limfjord is almost filtered out by the narrow and shallow channels. A harmonic analysis for the M_2 period, which is the strongest tidal component in the

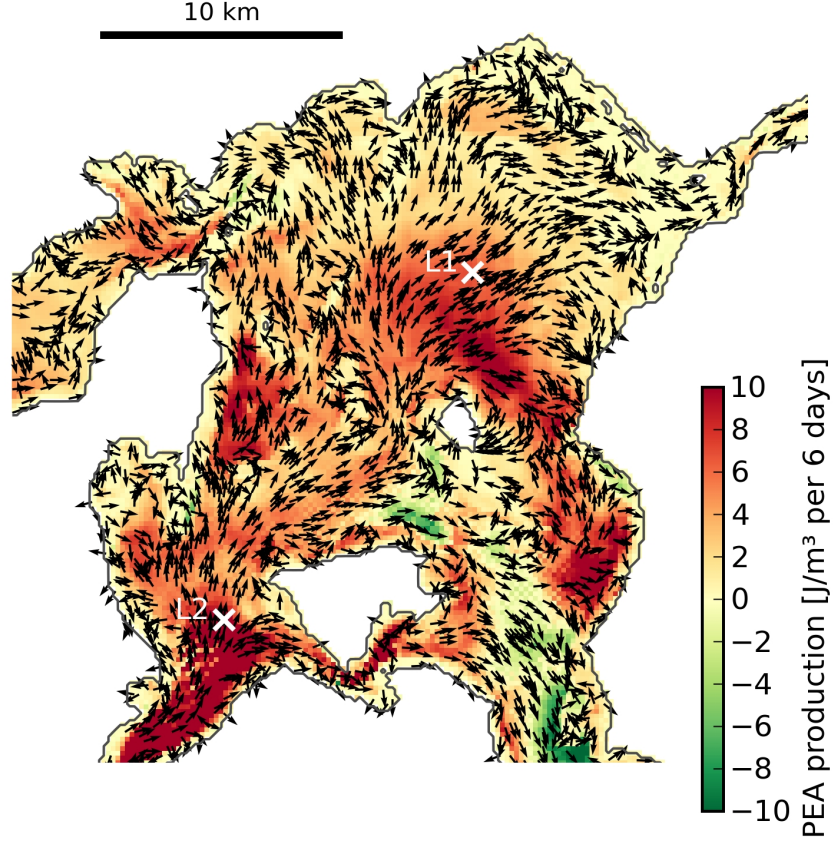


Figure 2.14: The change in the PEA from 27 May to 2 June in colours, overlaid with the directions of the mean, vertically integrated transport for the same period. The integrated effect of the different PEA contributions is investigated at locations L1 (station B in 2.6) and L2.

Limfjord, results in 4.6 cm of tidal amplitude in Løgstør Bredning. The tidal stirring in the Limfjord can be estimated by an empirical term quantifying the power per volume for reducing stratification, taken from *Simpson and Bowers* [1981]

$$T = \left(\frac{\partial \phi}{\partial t} \right)_{\text{tide}} = \frac{4\varepsilon k_b \rho u_s^3}{3\pi H} \quad (2.26)$$

with ε being the efficiency of tidal stirring, k_b being the seabed drag coefficient, H being the water depth and u_s being the depth averaged amplitude of tidal spring velocities. The tidal stirring term T can be compared to the anomaly of potential energy ϕ from (2.23). The ratio ϕ/T gives the time scale for fully mixing the water column. When setting $\varepsilon = 0.0037$ (like in *Simpson and Bowers* [1981]), $k_b \approx 0.0025$, $H = 7\text{m}$, $u_s \approx 0.1\text{m s}^{-1}$ and $\rho = 1017\text{ kg}\cdot\text{m}^{-3}$, $T \approx 0.6 \cdot 10^{-6}\text{W}\cdot\text{m}^{-3}$ is obtained. With a $\phi = 7.2\text{ J}\cdot\text{m}^{-3}$, which is a mean value for stratified periods in Løgstør Bredning, the tidal stirring would need ≈ 140 days to mix the

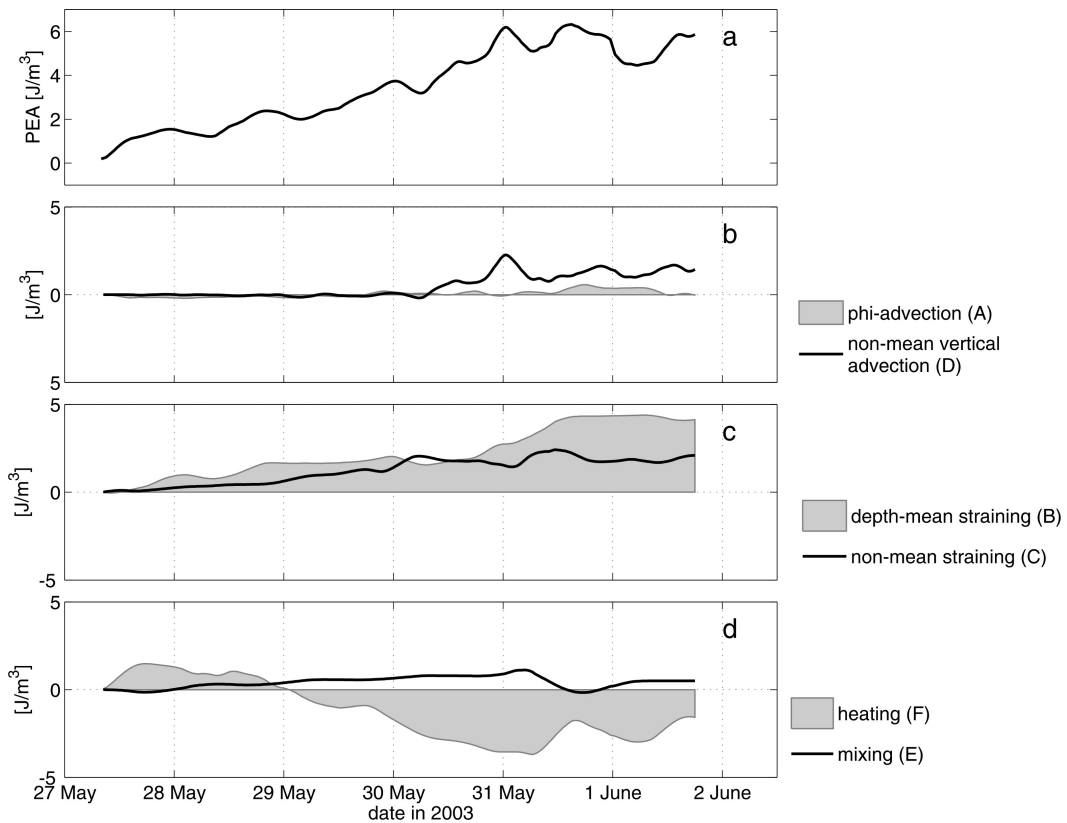


Figure 2.15: The integral time series of the different terms in the dynamic equation of PEA for the days 27 May to 2 June in the year 2003 at location L1 in Fig. 2.14. Panel a shows the temporal evolution of the PEA and panels b,c,d below show the integrated rates of the PEA due to the different contributors in the dynamic equation (2.25).

water column completely. In accordance with *Wiles et al.* [2006], we can therefore assume that tidal stirring does not have a significant effect on reducing stratification.

In the presence of dense bottom plumes, the weak tidal signal can have a considerable influence on the local PEA. Fig. 2.10 shows situations with bottom fronts in salinity. The stratified situations due to high salinities at the bottom in Fig. 2.9 can be interpreted to be plume-like structures triggered by the salinity fronts. A moving, dense plume results in advection of PEA and changes in the PEA by the vertical advection. The influence of the weak tidal motion on the changes of the PEA by the vertical advection and the non-mean straining is developing with the stratification and overlays the time series with an almost semidiurnal period since 30 May up to 3 June. At the south-western opening of the central basin (location L2 in Fig. 2.14), a tidal signal cannot be clearly identified in the integrated time series of the PEA terms. A harmonic analysis does result in 3.2 cm of variation in sea surface elevation by the M_2 tide. The small signature of an M_2 influence, which is hardly visible in the PEA advection since 31 May, is overlaid by other, more important processes at that location.

It is instructive to compare the simulated stratification with the measured oxygen saturation, and test whether low saturation levels are correlated with strong enduring stratification, as shown in Fig. 2.11. The oxygen saturation O_2^{sat} is calculated as ratio of measured oxygen

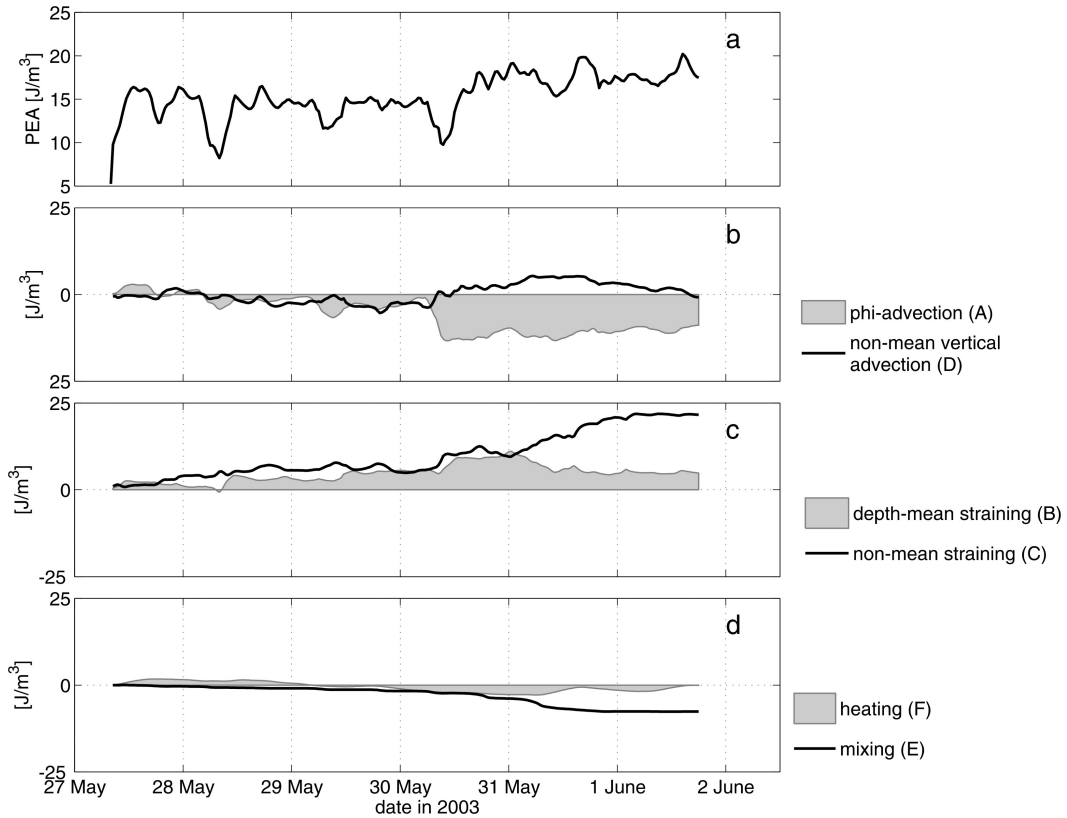


Figure 2.16: The integral time series of the different terms in the dynamic equation of PEA for the days 27 May to 2 June in the year 2003 at location L2 in Fig. 2.14. Panel a shows the temporal evolution of the PEA and panels b,c,d below show the integrated rates of the PEA due to the different contributors in the dynamic equation (2.25).

over the calculated maximum dissolved oxygen

$$O_2^{sat} = \frac{O_2^{abs}}{O_2^{max}}. \quad (2.27)$$

The maximum dissolved oxygen is calculated according to *Mortimer* [1981] as function of water temperature. The oxygen saturation near the bottom is low in periods of stratification due to depletion by benthic organisms. In periods of stratification, the pycnocline separates the bottom from the surface and thus the near-bottom water is not ventilated. Even when the PEA decreases already, the oxygen may still be depleted near the bottom, if mixing processes are limited to the upper water column. Oxygen measurements near the bottom therefore could be used as indicator for a recent stratified period. The model results should be able to close the gaps between the measurements. For example, Fig. 2.11 shows for the middle of June, that oxygen was depleted (oxygen saturation is still less than 60%, the same value like in the long stratification period around the 1 June) even though the measured PEA is already below typically values of stratification periods. The measured oxygen depletion indicates a period of suppressed mixing, which is reproduced by the model with a period of stratification in the days before. The same situation can be found at the end of August and around the 1 October. It should be stated again, that the high PEA values around 1 July is not verified and cannot be included in this comparison.

2.2.4 Summarising the Limfjord studies

The Limfjord model simulation provides verified data for investigating stratification in the Limfjord in the year 2003. The meteorological forcing and the riverine freshwater supply into the Limfjord are keys for a realistic Limfjord simulation. The processes of stratification and de-stratification are investigated as changes of the potential energy anomaly (PEA). The temporal changes of the PEA are decomposed into four terms directly related to differential advection, one term due to vertical mixing and one term due to heating and cooling. The decomposition provided an insight into the different stratifying and de-stratifying processes in the Limfjord.

Differential advection, driven by strong horizontal density gradients, and the superposition of these gradients with the additionally forced differential circulation by wind or a mean external pressure gradient are the major sources for stratification in the Limfjord. A case study shows that the de-stratification in the central Limfjord is driven by night-time surface cooling, mixing due to strong winds, and locally by advection of the stratified water body. It is interesting to note that the stabilising effect (in terms of stratification) of the mixing during night-time cooling is a significant cumulating effect in the PEA budget. A stratifying effect by heating due to absorption of light is not found in the presented study. Tides do not play a significant role in terms of stratification in the central Limfjord. The volume ratio of the inflowing North Sea water and the freshwater input measures 4:1, hence the salty inflowing water of about 30 psu will be thinned by 1/4. That is consistent with the mean salinity in the inner parts of the Limfjord of about 23 psu.

The stratifying effects of the differential advection benefit from the Limfjord's characteristics. It is quite uncommon to find a mean transport of oceanic water throughout a freshwater-dominated sound without significant tidal influence. Although there are not many systems like the Limfjord, the shown methods of analysing stratification and de-stratification can be adapted to other estuarine systems as well.

The presented study shows, that the PEA can be an indicator for rising oxygen depletion near the bed in regions with benthic living. A model setup for the Limfjord in adequate resolution as presented here could be used for local forecast for stratification, when the forcing from other forecast models is available. It would be possible to predict unfavourable conditions for the benthic shellfish community as well as favourable conditions for algal blooms, diminishing the water quality.

3 Numerical techniques for modelling stratified seas

3.1 Adaptive vertical coordinates

The section is organised as follows: First the concept of general vertical coordinates is briefly reviewed with respect to the primitive equations (section 3.1.1.1). Then, the grid adaptation strategies are derived (section 3.1.1.2). Afterwards, the numerical methods for solving the dynamical equations in the framework of the moving grids are discussed (section 3.1.1.3-3.1.1.8). In section 3.1.2, the implementation concept into the used 3D model are described. These methods are then compared and investigated in detail for four different idealised model scenarios (section 3.1.3). Finally, the results are summarised and discussed (section 3.1.4).

3.1.1 Grid adaptation

3.1.1.1 The transformed model space

In order to increase the mathematical flexibility of a 3D ocean model, a general vertical coordinate transformation Γ following *Kasahara* [1974] and *Deleersnijder and Ruddick* [1992] is carried out which maps the physical space (t^*, x^*, y^*, z) , with the vertical coordinate z pointing upwards, into a transformed space spanned by the coordinates (t, x, y, γ) . The general vertical coordinate γ is assumed to be monotone with respect to z :

$$\gamma = \Gamma(t^*, x^*, y^*, z) \Leftrightarrow z = z(t, x, y, \gamma). \quad (3.1)$$

The following coordinate change is thus used:

$$t^* = t, \quad x^* = x, \quad y^* = y, \quad z = z(t, x, y, \gamma) \quad (3.2)$$

with the Jacobian of the transformation being simply $\partial_\gamma z$. γ can be chosen for convenience to vary between -1 at the bottom and 0 at the surface.

One of the simplest coordinate transformation of this type is the so called σ -coordinate transformation

$$\gamma = \sigma = \frac{z - \eta}{D}, \quad (3.3)$$

where η is the sea surface elevation (counted positive upwards from $z = 0$ at the reference surface) and $D = H + \eta$ is the total local depth (topographic depth H plus sea surface elevation)

The purpose of the present paper is to find some optimal way to define the function $z(t, x, y, \gamma)$. The adaptive coordinate must always and everywhere satisfy a non-vanishing Jacobian and total height conservation. Apart from these restrictions, the coordinate change is highly flexible and can therefore accommodate any desired treatment.

The dynamic equations in the physical space can then be integrated in the transformed, discretised space as presented in *Burchard and Petersen* [1997] or alternatively presented in *Lander et al.* [1994].

From here on, in order to simplify the numerical treatment, we try to find the non-uniform coordinate transformation $z(x, y, t, \sigma)$, where σ is uniformly distributed in $[-1, 0]$ corresponding directly to the discrete numerical vertical grid indices. From there the non-uniform γ distribution can be recovered by the definition

$$\gamma = \frac{z(\sigma) - \eta}{D} \quad (3.4)$$

The objective is to find the coordinate transformation

$$z = z(\sigma), \sigma \in [-1, 0] \quad (3.5)$$

which covers the domain $z \in [-H, \eta]$ in some optimal way.

3.1.1.2 Optimisation technique

Optimisations for general vertical coordinates are starting with generalising the sigma distribution to be zoomed towards bottom and surface, also called s-grid, in order to optimise the near-surface and near-bottom resolution. In *Fiedler* [2002], a grid adaptation by an empirical function depending on mixed layer depth is presented. The grid transformation strategy here should generally optimise the resolution of vertical gradients based on *a priori* minimisations (approach advocated in *Thompson et al.* [1985] and follow up of *Burchard and Beckers* [2004]).

One possibility is minimising the cost function \mathcal{I}_1 defined by

$$\mathcal{I}_1 = \int_{-H}^{\eta} (\partial_{\sigma} f) dz = \int_{-1}^0 \partial_z f (\partial_{\sigma} z)^2 d\sigma = \int_{-1}^0 w_1 (\partial_{\sigma} z)^2 d\sigma \quad (3.6)$$

for each individual water column in the model domain. Here the weight $w_1 = \partial_z f$ is obviously related to the rate of change of the function f or alternatively to the inverse length scale of the function variations.

Minimisation of (3.6) tries to find the coordinate change $z = z(\sigma)$ such that in the new coordinates, the gradients (with respect to the new coordinate) of f are uniform and small. The Euler Lagrange equation for fixed end points $z(-1) = -H$ and $z(0) = \eta$ and assuming the weighting function depending on the normalised coordinates: $w_1 = w_1(\sigma)$ writes as

$$\partial_{\sigma} (w_1 \partial_{\sigma} z) = 0 \quad (3.7)$$

However, in practice the weighting will rather be dependant on physical space coordinates since ultimately this is what is of interest to the modeller. This can be handled by using eq. (3.7) with a diffusion term for a discrete set of σ levels, but where w_1 must be updated at each change of z . Hence, (3.7) is essentially non-linear in that case. Another approach would be to accept the *a priori* dependence of w_1 on the physical space and to minimise instead

$$\mathcal{I}_2 = \int_{-1}^0 w_1(z) (\partial_{\sigma} z)^2 d\sigma \quad (3.8)$$

which lead to the same Euler-Lagrange equation as (3.7). It can easily be shown that this approach minimises the error when assuming piecewise constant functions for a discrete set

of data points. Instead of solving the Euler-Lagrange equation exactly at each model time-step, we rather allow to move the grid towards this exact solution in a time-marching manner:

$$\partial_t z - \partial_\sigma \left(k^{grid} \partial_\sigma z \right) = 0 \quad (3.9)$$

with the grid-related diffusivity k^{grid} and $\sigma \in [-1, 0]$ and boundary conditions for z from $z(-1) = -H$ and $z(0) = \eta$.

According to *Burchard and Beckers* [2004], the grid diffusion coefficient k^{grid} (which has the physical unit s^{-1}) is calculated as

$$k^{grid} = \frac{D}{t_{grid}} \left(c_{N^2} K_{N^2}^{grid} + c_{S^2} K_{S^2}^{grid} + c_d K_d^{grid} + c_b K_b^{grid} \right) \quad (3.10)$$

with the stratification-related component

$$K_{N^2}^{grid} = \frac{\max(0, \partial_z \rho)}{\Delta \rho}, \quad (3.11)$$

the shear-related component

$$K_{S^2}^{grid} = \frac{|\partial_z v|}{\Delta v}, \quad (3.12)$$

the near-surface component

$$K_d^{grid} = \frac{1}{d + d_0}, \quad (3.13)$$

and the background component

$$K_b^{grid} = \frac{1}{D}. \quad (3.14)$$

Here, $\Delta \rho$ is a reference density difference and Δv a reference velocity difference. The grid diffusion time scale is denoted by t_{grid} . d is the distance from the surface, d_0 is a variable determining the intensity of the near-surface grid zooming and the coefficients c_X are the diffusion weights. For the discretised version see *Burchard and Beckers* [2004], where this approach is applied for a 1D water column model.

The optimisation technique to minimise the integral of layer-related, vertical gradients in the model grid as presented above is easy to implement in an ocean model. The minimisation distributes the state variables and the velocity fields onto the vertical grid to be represented uniformly. It is easy to ensure a positive Jacobian and boundary fitting, because it is a valid transformation in that sense. However, the minimisation does not give a direct link between adjacent verticals in the horizontal model grid. The only link is the continuity of the physical fields to which the adaption is done. The horizontal filter methods presented in the sections 3.1.1.4-3.1.1.5 below will supply a link between neighbouring water columns. For application in ocean models, the choice of diffusion weights c_X is not unique and will depend on the objective of the model study.

3.1.1.3 Vertical discretisation

For the discretisation, the physical space is vertically divided into N layers. This is done by introducing internal surfaces z_k , $k = 1, \dots, N - 1$ which do not intersect, each depending on the horizontal position (x, y) and time t :

$$-H(x, y) = z_0(x, y) < z_1(x, y, t) < \dots < z_{N-1}(x, y, t) < z_N(x, y, t) = \eta(x, y, t) \quad (3.15)$$

with the local layer depths

$$h_k = z_k - z_{k-1}. \quad (3.16)$$

for $1 \leq k \leq N$, the local bottom coordinate, $H(x, y)$, and the sea surface elevation, $\eta(x, y, t)$. The objective of the grid adaption is to find a distribution of the vertical location of interfaces z_k so as to place a given number of discrete grid points in an optimal way in terms of the specified optimisation parameters. This is leading to the height of the grid layers of $h_k = z_k - z_{k-1}$ with $\sum_k h_k = H + \eta$ if the grid is formed correctly with $z_0 = -H$, $z_N = \eta$ and $z_k > z_{k-1}$.

The horizontal transports are calculated from the hydrostatic Reynolds-averaged Navier-Stokes equations in the physical model space. The vertical velocity equation reduces for hydrostatic flow to the hydrostatic balance,

$$\partial_z p = -g\rho, \quad (3.17)$$

such that for incompressible flow the vertical velocity w is calculated by means of vertically integrating the incompressibility condition

$$\partial_x u + \partial_y v + \partial_z w = 0 \quad (3.18)$$

where p is the pressure, g the gravitational acceleration and (u, v, w) are the components of the velocity vector. The discretisation of (3.18) is of the following form:

$$\bar{w}_k = \bar{w}_{k-1} - \partial_t h_k - \partial_x p_k - \partial_y q_k, \quad (3.19)$$

with the grid-related vertical velocity

$$\bar{w}_k = \partial_t z_k - u|_{z_k} \partial_x z_k - v|_{z_k} \partial_y z_k \quad (3.20)$$

and the layer-integrated transports

$$p_k = \int_{z_{k-1}}^{z_k} u \, dz, \quad q_k = \int_{z_{k-1}}^{z_k} v \, dz, \quad (3.21)$$

see *Burchard and Petersen [1997]* for details.

3.1.1.4 Horizontal filtering of interface positions

The independently adapted vertical coordinates can be homogenised horizontally by having similar vertical positions for the same levels on σ . However, the truncation error in the calculation of horizontal gradients in a horizontally non-aligned vertical coordinate system is indicated to be small for a small value of

$$A_{hc} = \frac{|\partial_x z_k|}{h_k / \Delta x}, \quad (3.22)$$

where $A_{hc} \geq 1$ if the hydrostatic consistency is violated and extrapolations are expected. In our case with arbitrary small h_k , the potential errors can be reduced by a horizontal diffusion of the vertical position for each discrete level on the numerical grid σ . The filtering can be defined as

$$\partial_t z_k = \partial_x (\mathcal{A}_i \partial_x z_k) + \partial_y (\mathcal{A}_i \partial_y z_k) \quad (3.23)$$

where x and y are the spatial coordinates of the numerical grid and the diffusivity \mathcal{A}_i scales with $\alpha_{hor} \frac{\Delta x^2}{4\Delta t_f}$. Δt_f is a timescale for the horizontal filtering, which is the baroclinic timestep in the shown experiments, and α_{hor} is a number between $[0, 1]$ and defines the strength of the horizontal filtering of interface positions.

The horizontal filtering of interface positions is a control on the horizontal regularity of the grid and it is easy to implement. For the resulting two-dimensional elliptic equation, no extrema may exist. If a local extrema exist in a specific vertical, the filtering in the whole model domain may result in a non-unique coordinate change. The filtering may also lead to negative Jacobians and interface depths below topography. Hence an enforcing of well-defined grid is required afterwards (see section 3.1.1.8).

At the lateral boundaries, Dirichlet or Neumann-type conditions could be applied.

3.1.1.5 Advection of z , Lagrangian approach

The incompressibility condition (3.19) can be rewritten as

$$\partial_t h_k + \partial_x p_k + \partial_y q_k = \bar{w}_{k-1} - \bar{w}_k. \quad (3.24)$$

The transformed vertical velocity \bar{w} relative to the moving grid is defined such that fluxes across coordinate surfaces are zero if this velocity is zero. For pure Lagrangian-type models, $\bar{w} = 0$ is defined. Normally, equation (3.24) is used to diagnose vertical velocities from prescribed changes in the grid and divergence of the velocity field as presented in the model description for the model used here.

But it can also be used to enforce Lagrangian movements of the grid by solving the equation for h_k imposing zero relative vertical velocity:

$$\partial_t h_k = -\partial_x p_k - \partial_y q_k \quad (3.25)$$

will give a first guess for new positions \tilde{h}_k^{n+1} from which the new values can be calculated by any further re-gridding strategy. The Lagrangian-type guess for the new layer heights is

$$\tilde{h}_k^{n+1} = h_k^n - \alpha_{lag} \Delta t (\partial_x p_k + \partial_y q_k) \quad (3.26)$$

where the upper indices denote the time step numbers. For values $\alpha_{lag} = 1$, the vertical discretisation change (3.26) is fully Lagrangian and values $\alpha_{lag} < 1$ are introducing a Lagrangian tendency only. The Lagrangian approach decreases the grid-related vertical transports and thus the numerical mixing resulting from vertical advection of vertical tracer and momentum gradients. However, the grid-related vertical velocities are calculated after the grid adaption using equation 3.19.

The Lagrangian tendency minimises vertical advection and associated numerical mixing since strong vertical gradients moving with the vertical flow velocity are typical in oceanic applications. It is easy to implement if the grid adaption is placed correctly into the model loop. Nevertheless, the Lagrangian tendency may lead to invalid grids and layer interfaces below topography or above sea level. If an initial distribution of layers is defined, a pure Lagrangian advection of layers cannot control the grid regularity, especially not, if open boundaries are included in the model domain.

3.1.1.6 Horizontal filtering of layer thicknesses

Violating the hydrostatic consistency in the model grid discretisation indicates possible truncation errors, which feed into the calculation of the internal pressure gradient. *Song* [1998] estimates the error for the pressure gradient calculation over a vertical extent of a single cell scales with $\delta_x(\delta_\sigma z)$ (in our notation: $\delta_x h_k$) for a buoyancy field which can be represented by second order polynomials in the vertical.

Beside that, the magnitude of the pressure gradient error is depending on the pressure gradient formulation (PGF) itself. Higher order terms for the representation of the buoyancy field will result in higher order terms for the error in the PGF. According to *Song* [1998], the discretisation error disappears for

$$\delta_x h_k = 0, \quad (3.27)$$

a condition, which can be approached by applying a horizontal diffusion of layer thickness. The diffusion of layer thickness writes as

$$\partial_t h_k = \mathcal{A}_h (\partial_{xx} + \partial_{yy}) h_k, \quad (3.28)$$

where \mathcal{A}_h scales with $\alpha_{dif} \frac{\Delta x^2}{4\Delta t_f}$ and α_{dif} is a number between $[0, 1]$ and defines the strength of the horizontal filtering of layer thicknesses.

Next to the reduction of PGF errors, the horizontal diffusion of layer height is an additional control for the horizontal regularity of the grid. Drastical changes between adjacent water columns are smoothed. The iterative process of the vertical optimisation technique and the horizontal filtering of layer thicknesses tends to create “iso-gradient” layers, which are locally similar to isopycnal layers for small isopycnal slopes and distant to the bottom and the surface.

The horizontal filtering of layer thicknesses can have the same effect as the horizontal filtering of layer heights for special scenarios. For a horizontally varying, vertical optimisation effect or bathymetry, both filters will act differently.

However, in addition to the diffusion of layer height h , the conservation of total depth may be violated (similar problems as with the horizontal bolus velocity in isopycnal models (see *Gent and McWilliams* [1990])). The conservation of total depth has to be enforced separately as suggested in section 3.1.1.8. Thus the effect of minimising the pressure gradient error is limited. At least in a pure σ -coordinate grid, the effect of horizontal diffusion of layer height is compensated by the depth conservation.

3.1.1.7 Isopycnal tendency

The objective for this aspect of the grid adaption strategy is to place z_k to be on user-defined ρ surfaces. Special treatments are needed at the bottom, the surface and for interleaving layers in pure isopycnal models, when isopycnals disappear or new layers have to be added. Therefore, the objective is move in time the point from z_k^n into a position z_k^{n+1} where the density has a given value ρ_k^* . This can be achieved by observing that

$$\rho(z^{n+1}) \sim \rho(z^n) + (z^{n+1} - z^n) \partial_z \rho. \quad (3.29)$$

So that the best guess for the update would be

$$z_k^{n+1} = z_k^n + \frac{\rho_k^* - \rho(z_k^n)}{\partial_z \rho}, \quad (3.30)$$

meaning that one can add the following tendency term

$$z_k^{n+1} = z_k^n + \alpha_{iso} \frac{\rho_k^* - \rho(z_k^n)}{\partial_z \rho} \quad \alpha < 1 \quad (3.31)$$

where $\alpha_{iso} = 1$ is strong isopycnal tendency and $\alpha_{iso} = 0$ is no isopycnal tendency.

ρ_k^* , the target isopycnal value for level k can be prescribed *a priori* like in isopycnal models, but it could be more flexible to let the model calculate the target densities from the density distribution itself. This can be achieved iteratively by assigning to ρ_k^* a mean value of all ρ_k from surrounding water columns. The stencil for the averaging can be large if some basin scale "isopycnals" are thought. Averaging only over subbasin scales also allows different "isopycnals" to be used in physically different regimes. In section 3.1.2 an example method for calculating the ρ_k^* values is given as used for the examples.

Of course, instead of pushing given discrete levels to prescribed isopycnal levels, one could also attract them in a similar way to prescribed z level, oxygen values or any other *a priori* distribution. A pure grid adaption towards prescribed z levels will create a hybrid grid between s -coordinate and z -level grids.

The advantage of using such an isopycnal tendency (coupled possibly with the Lagrangian tendency) compared to purely isopycnal models is that the grid does not stick on preserving certain density values. Hence, the well tested model techniques for calculating the vertical mixing and handling the non-linear effects of the equation of state (such as cabbeling) can kept the same. Furthermore, if the physical situation precludes efficient use of purely isopycnal models (for example during deep water formations), the adaptive grid method simply will move grid points in a non-isopycnal way.

The method also could allow to prescribe different isopycnal levels (to which grid points are attracted) in different basins, with transition zones. Again, the numerical grid, since it is absolutely arbitrary, does not need to adapt physical parameterisations as they are already included in the primitive equation model. The advantage of trying to follow isopycnals simply lies in the fact that if the physical processes are isopycnal, then the numerical grid allows a better representation of those processes as they are aligned with the grid.

Again, the isopycnal tendency may lead to invalid grids and interface depths below topography so that total depth conservation has to be ensured. If there is noise in the isopycnal depths, it will be transferred to the numerical grid by the isopycnal tendency, which may have impacts on the horizontal resolution of the flow field.

3.1.1.8 Enforcing well defined grids

Working with the layer heights h_k allows easy diffusion of h , but it may lead to a "conservation" problem of the local total depth for the adapted grid. Working with the interface positions z_k might result in negative layer heights. For a well defined grid, it has to be ensured that $z_0 = -H$ and $z_N = \eta$. Additionally it has also to be enforced that $z_{k+1} > z_k$.

If the approach is based on layer thickness tapering or horizontal diffusion of z -levels, one must always include the constraint

$$\sum_k h_k = H + \eta \quad (3.32)$$

and $h_k > 0$. We aim for a single step correction (or at least a finite (known and proportional to N) number of steps) in order to control the computing cost.

The implementation is to always check for positive layer heights and enforce the layer heights to be larger than a specified minimum depth. Finally, the adapted, uncorrected grid \tilde{h}_k is corrected to match the local depth by

$$h_k = \left(\alpha_k \frac{H + \eta}{\sum \alpha_k \tilde{h}_k} \right) \tilde{h}_k, \quad (3.33)$$

where the correction weights α_k can be also used to concentrate even more levels where needed (see *Liseikin* [1999]). Here we use $\alpha_k = 1$ to apply a global compression/expansion to fit the total depth.

3.1.2 Implementation

3.1.2.1 Implementation of the grid adaption in the model loop

The grid adaption is part of the baroclinic mode calculation in the main model loop of GETM. The main order in the loop of the baroclinic mode is

1. updating the horizontal transports
2. updating the grid (which is the grid adaption in case of adaptive grids) and the grid-related vertical velocities
 - a) The pseudo-Lagrangian adaption (equation (3.26) in section 3.1.1.5) and the horizontal diffusion of layer height (equation (3.28) in section 3.1.1.6) and additionally an enforcing of well behaved grid is called (see section 3.1.1.8). The horizontal diffusion of layer heights is not activated between land and water cells and outside the model domain at the open boundaries.
 - b) The vertical refinement of the grid by horizontal filtering of interface positions (equation (3.23) in section 3.1.1.4) and the isopycnal tendency (equation (3.31) in section 3.1.1.7): The horizontal filtering of interface positions is switched off for thin layers (if the layer height less than the specified minimum depth) and between land and water cells. The distance of interface movement by the isopycnal tendency is limited to be less or equal the layer height in order to avoid pathologic grids when strong along-layer gradients are existing (e.g. near a plume front or steep slopes). The isopycnal tendency is calculating its reference densities by averaging over a given horizontal stencil of 5x5 grid points within the specific model layer:

$$\rho_{i,j,k}^* = \frac{1}{\sum_{i',j'=i-2,j-2}^{i+2,j+2} m_{i',j'}} \sum_{i',j'=i-2,j-2}^{i+2,j+2} m_{i',j'} \cdot \rho_{i',j',k}, \quad (3.34)$$

where i, j, k are the grid cell indices in the 3D model grid and m is a land mask with $m = 0$ for land cells and $m = 1$ for water cells. Again the enforcing of a well behaved grid is called.

- c) The grid adaption to stratification, shear and distance to bottom and surface (equation (3.9) in section 3.1.1.2). A background adaption towards an equally spaced vertical grid is calculated for the sum of the four related tendencies equalling

one. The different tendencies could be combined locally weighted, depending on depth, velocity, sub-basin averaged stratification for example. In our case, the weights are specified constant in time and space. The vertical diffusion in the grid adaption is calculated implicitly.

d) The grid related vertical velocities are calculated from equation (3.19).

3. evaluating the turbulent mixing quantities
4. updating temperature, salinity and finally density distributions

For the final moving of data when grid points have been adapted, a high-order advection scheme is needed (*Iselin et al.* [2002]). The updated distribution of tracers and transports is calculated by means of the chosen advection scheme based on the grid-related vertical velocities, calculated after the grid handling in the model loop. Thus, a specific remapping of tracer and velocity fields as presented in *White and Adcroft* [2008] is not necessary here. In addition, with the present approach tracer conservation is ensured by the advection scheme. It should be noted that due to the tracer re-distribution by the high-order advection schemes, filtered gridding is not leading to filtered tracer distributions.

The grid adaptation must be done just before mass conservation in the model loop, which is assured in our model by the calculation of the grid-related vertical velocity.

The different parameters of the grid adaption are listed as follows:

α_{hor}	factor for horizontal filter of interface positions
α_{lag}	factor for Lagrangian tendency (see 3.26)
α_{dif}	factor for horizontal filter of layer heights h_k
α_{iso}	factor for isopycnal tendency (see 3.31)
c_{N^2}	diffusion weight related to stratification
c_{S^2}	diffusion weight related to shear
c_d	diffusion weight related to distance from surfaces
d_{surf}	norm for distance related to c_d
d_{min}	minimum height for enforcing well defined grids
t_{grid}	grid adaption time scale

The diffusion weights from (3.10) should add up to $1 = c_{N^2} + c_{S^2} + c_d + c_b$. Hence, the diffusion weight related to the background σ -layer distribution is calculated accordingly and is excluded from the list of free parameters. Typical sets of these grid adaption parameters are given in the examples, discussed in the next section. A visualisation of the horizontal filters is provided in fig. 3.1.

It is possible that linking of parameters will be practical in realistic studies, for example linking the Lagrangian and isopycnal tendency in order to get isopycnal-type coordinates. Also α_{dif} might be linked to the diffusion weights and the minimum layer height in order to force the horizontal smoothing, when potentially distorted grids are expected.

The computational overhead by the grid adaption is mostly determined by an additional call to the implicit solver for the vertical grid diffusion and the calculation of the running mean of the density for the isopycnal tendency. Therefore, the calculation of the running mean of the density is skipped if α_{iso} is zero.

For a flexible initialisation of the vertical coordinate discretisation, three options are implemented in the model code:

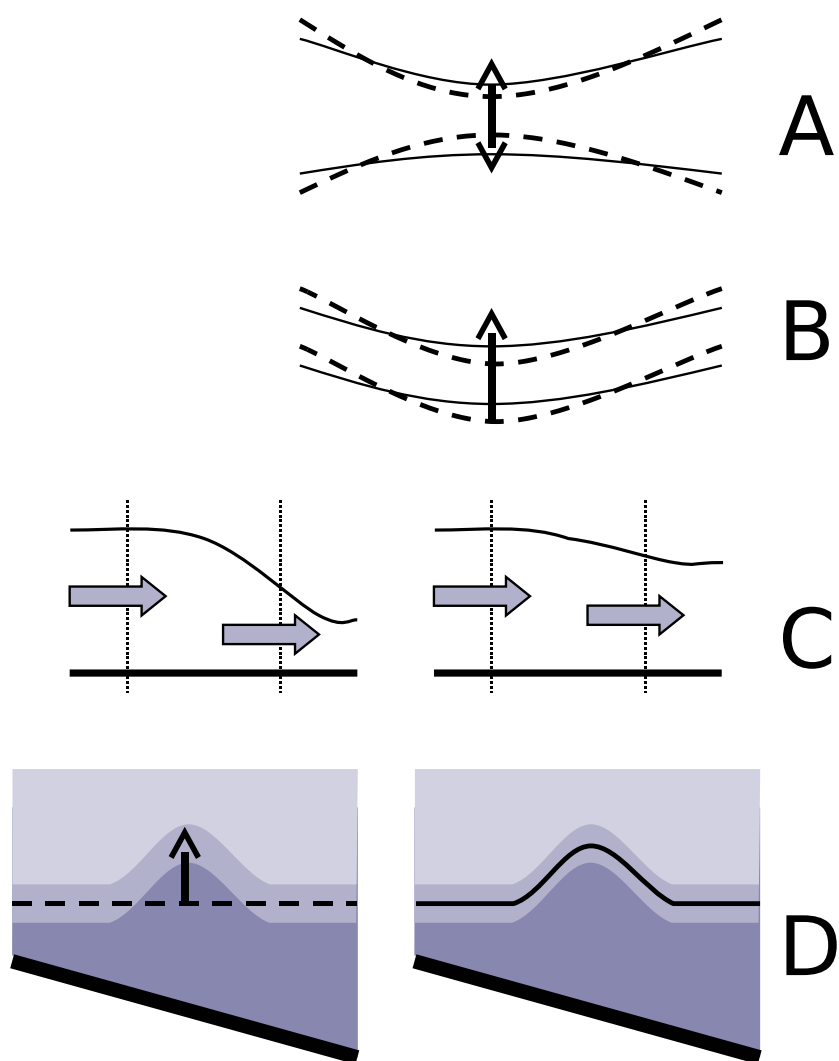


Figure 3.1: The horizontal filters as implemented for the grid adaptation: A - filter for layer heights, B - filter of interface positions, C - Lagrangian tendency, D - isopycnal tendency

- a) Starting with predefined distributions for temperature and salinity without any velocities, and a sigma-type layer distribution, the grid adaption is expected to take place during the model run.
- b) starting with predefined distributions for temperature and salinity without any velocities and pre-adaption of the grid to the density distribution and the bathymetry. During the pre-adaption process, only vertical transport through the layer interfaces is allowed. After the pre-adaption, a balance between adaption to stratification and bathymetry should be approached, in order to avoid a strongly moving grid at the beginning of the simulation. The initial temperature and salinity fields are re-interpolated onto the pre-adapted model grid afterwards.
- c) starting in hotstart mode, which continues an existing simulation. The information, which is needed at the beginning of a simulation loop is read from a file during initialisation.

3.1.3 Examples

The examples in the following will investigate the performance of the grid adaption in terms of numerical mixing (internal seiche (section 3.1.3.1) and multi-basin overflow (section 3.1.3.2) examples) and in terms of pressure gradient errors for experiments with an oceanic seamount (section 3.1.3.3). In a coastal upwelling experiment (section 3.1.3.4), the grid adaption is applied to a more realistic scenario. In all of the examples, the best-practice model techniques of GETM are used. A third-order, monotonic TVD scheme is used for advection of density and velocity and in general a high-order internal pressure gradient scheme (*Shechetkin and McWilliams* [2003]) is adopted.

Mixing is quantified here as the tracer variance decay, which can be evaluated for the numerically and physically induced mixing as presented by *Burchard and Rennau* [2008]. The tracer variance decay by physical mixing D^{phys} is estimated by the decay term in the budget equation for the square of the mean tracer s due to turbulent diffusion

$$D^{phys} = 2K_v (\partial_z s)^2 \quad (3.35)$$

where K_v is the vertical component of the turbulent diffusivity. Contributions from the horizontal diffusivity are neglected, because it is switched off in the following examples. D^{phys} can be directly compared to the tracer variance decay due to numerical mixing, which can be calculated by the difference between the advected amount of the squared tracer and the squared amount of the advected tracer divided by the time step Δt (see *Burchard and Rennau* [2008]). The tracer variance decay due to numerical mixing D^{num} for a certain model grid cell i at a certain time step number $n + 1$ writes as

$$D_i^{num} = \frac{A \left\{ (s_i^n)^2 \right\}_i - (A \{s_i^n\}_i)^2}{\Delta t} = \frac{A \left\{ (s_i^n)^2 \right\}_i - (s_i^{n+1})^2}{\Delta t}. \quad (3.36)$$

where $A \{ \dots \}_i$ is the tracer concentration resulting from a pure advection step and Δt is the time step. The tracer concentration s_i^{n+1} is obtained after the advection step in cell number i . Equation (3.36) can be integrated in the discrete model space with grid cell heights h_i^{n+1} as

$$\Delta t \sum_i h_i^{n+1} D_i^{num} = \sum_i h_i^{n+1} A \left\{ (s_i^n)^2 \right\}_i - \sum_i h_i^{n+1} (s_i^{n+1})^2. \quad (3.37)$$

Since the advection schemes used here are conservative, for closed domains without boundary fluxes, (3.37) can be written as

$$\Delta t \sum_i h_i^{n+1} D_i^{num} = \sum_i h_i^n (s_i^n)^2 - \sum_i h_i^{n+1} (s_i^{n+1})^2. \quad (3.38)$$

Hence, the difference of the tracer variance in a closed domain before and after the advection step is given by the domain-wide integral of the value D_i^{num} .

Riemenschneider and Legg [2007] showed that in basin-scale overflow simulations the expected mixing of tracers is covered exhaustively by the numerical mixing. Hence, the simulated tracer mixing was depending on the model resolution, which is unsatisfactory for a physical description of the mixing processes. The numerical mixing is needed for the monotonicity of the advection scheme. It has to be reduced as much as possible within this requirement by the model numerics in order to get a physically based description of the mixing by a turbulence model. It is expected here that the physical mixing parameters in the model are represented in a quantitatively realistic way by properly implemented turbulence closure models (see, e.g., the one-dimensional model-observation comparison studies by *Burchard et al. [2002]*, *Simpson et al. [2002]*, *Arneborg et al. [2007]*, *Souza et al. [2008]*, *Peters and Baumert [2007]*, or the three-dimensional model study by *Ilicak et al. [2008]*). The physical and numerical mixing contributions always compete in reducing the tracer variance in the model domain. It is thus expected that a reduced numerical mixing could increase the amount of physical mixing with the same turbulent diffusivity but acting on stronger gradients.

3.1.3.1 Internal seiche

This two-layer flow scenario will demonstrate that the Lagrangian approach indeed allows to move grid points passively with the vertical velocity field. It will further be shown that grids which are directly adapted to the changing vertical stratification substantially reduce numerical mixing and perform similarly to Lagrangian grids. We will further show that in contrast to these adaptive grids a fixed grid will cause strong numerical diffusion with the effect that the seiche period is overestimated.

For this test case which is based on a two-dimensional closed flat bottom domain with a length of $L = 64$ km and a mean depth of $H = 20$ m, friction and mixing are neglected in order to allow for an analytical solution. The two layers have a density difference of $\Delta\rho = 3.9 \text{ kg m}^{-3}$. The initial interface between the two layers is located at

$$z^* = -\frac{H}{2} \left(1 - \epsilon \sin \left(\pi \frac{x}{L} \right) \right), \quad (3.39)$$

for $x \in [-\frac{1}{2}L, \frac{1}{2}L]$, where $x = 0$ is the basin centre. The relative amplitude ϵ , is also a measure for the non-linearity of the scenario. Initial velocities are zero, the initial sea surface elevation is set to

$$\eta = -\frac{g'}{g} \frac{H}{4} \epsilon \sin \left(\pi \frac{x}{L} \right) \quad (3.40)$$

with the reduced gravitational acceleration

$$g' = \frac{\Delta\rho}{\rho_0} g. \quad (3.41)$$

grid	α_{lag}	α_{dif}	c_{N2}	c_{S2}	c_b	d_{min}	t_{grid}
fully Lagrangian	1.0	0.0	0.0	0.0	0.0	0.1 m	1 h
adaption to stratification	0.0	0.5	0.5	0.0	0.5	0.1 m	1 h
adaption to shear	0.0	0.5	0.0	0.5	0.5	0.1 m	1 h

Table 3.1: Parameters for the grid adaptations in the internal seiche experiments

In this case, the linearised solution from *LeBlond and Mysak [1978]* for small density differences can be decomposed in the barotropic and baroclinic modes. Hence the solution for the interface position is

$$z^* = -\frac{H}{2} \left(1 - \epsilon \cos(\omega t) \sin\left(\pi \frac{x}{L}\right) \right) \quad (3.42)$$

and

$$\eta = -\frac{g' H}{g} \frac{\epsilon}{4} \sin\left(\pi \frac{x}{L}\right) \cos(\omega t) \quad (3.43)$$

for the sea surface elevation η with the frequency

$$\omega = \frac{1}{2} \sqrt{g' H} \frac{\pi}{L}. \quad (3.44)$$

The analytical solution for $\epsilon \rightarrow 0$ for the upper layer velocity u^+ and the lower layer velocity u^- is

$$u^+ = -u^- = \frac{\epsilon}{2} \sqrt{g' H} \sin(\omega t) \cos\left(\pi \frac{x}{L}\right). \quad (3.45)$$

The discretisation for this scenario is carried out with a horizontal resolution of $\Delta x = 500$ m, a barotropic timestep of 15 s, a baroclinic timestep of 150 s and $N = 20$ vertical layers. In order to avoid interpolation of the initial density distribution into the numerical grid, the initial vertical grid is constructed such that the middle layer is aligned with the density interface and the remaining layers are distributed with equidistant spacing between the bottom and the interface and the interface and the surface, respectively:

$$h_k = \begin{cases} \frac{-z^* + \eta}{\frac{1}{2}N}, & k = \frac{1}{2}N + 1, \dots, N \\ \frac{H + z^*}{\frac{1}{2}N}, & k = 1, \dots, \frac{1}{2}N \end{cases} \quad (3.46)$$

with the density jump between $k = \frac{1}{2}N$ and $k = \frac{1}{2}N + 1$.

In the upper panel of figure 3.2 the solutions for the normalised lower layer velocity u^- at $x = 0$ for four different grid types and a non-linearity of $\epsilon = 0.2$ are compared to the analytical linear solution (3.45): the fully Lagrangian grid, the adaptation to stratification, the adaption to shear and the grid fixed to the initial grid with fitting to the changing water depth, only. In order to enable a fully Lagrangian grid, the background diffusivity c_b is exceptionally set to zero. The parameters for the grid adaptations are listed in table 3.1, unmentioned parameters equal zero for all experiments.

It is clearly seen that the Lagrangian grid and the adaptive grids based on vertical optimisation are close to each others and also close to the linear analytical solution. In contrast

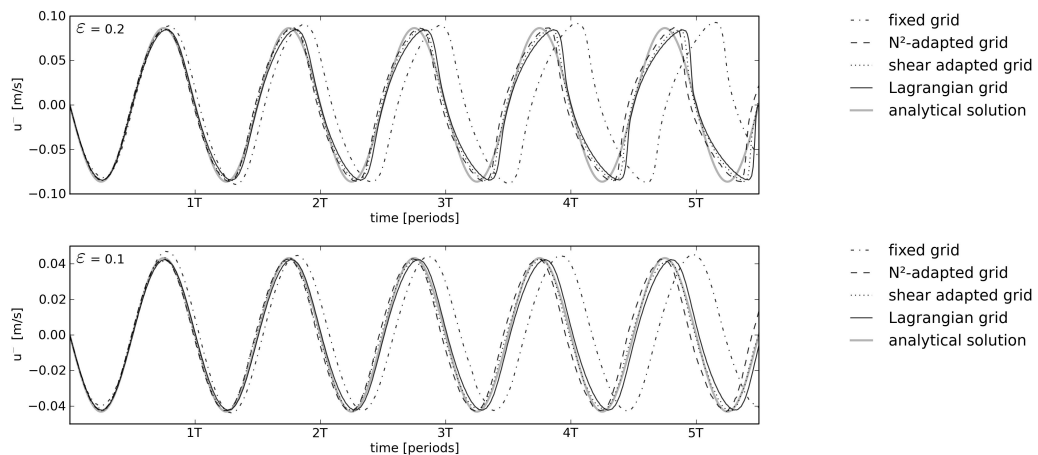


Figure 3.2: The lower layer velocity in the seiche experiment for four different grid types compared to the analytical solution from (3.45). The upper panel results are for a non-linearity of $\varepsilon=0.2$ and the lower panel for a non-linearity of $\varepsilon=0.1$.

to this, the solution with the fixed grid strongly deviates from the other solutions, both, in period and amplitude.

Figure 3.3 shows layer and density distribution for the fixed grid and the grid adapted to stratification after half of a period of oscillation. It can be clearly seen that the result with the fixed grid is highly diffusive and the solution thus is inaccurate.

In order to prove that the normalised Lagrangian solution (as well as the adaptive-grid solutions) converges towards the normalised linear analytical solution for $\varepsilon \rightarrow 0$, simulation results for $\varepsilon = 0.1$ are shown for the adaptive grids and the fixed grid in the lower panel of figure 3.2. The solutions for the adaptive grids are indeed close to the analytical solution again, whereas the fixed grid solution strongly deviates from it.

3.1.3.2 Multi-basin overflow

A second example showing a reduction of numerical mixing by the adaptive vertical coordinates is a marginal sea overflow scenario as studied intensively already by *Burchard and Rennau* [2008] in terms of numerical mixing. The bathymetry is a simplified transect through the Baltic Sea, following the major inflow events discussed in e.g. *Feistel et al.* [2006]. The model domain (see figure 3.4) has a horizontal resolution of 2100 m, 40 vertical levels and is closed at both sides of the horizontal axis. The density field does only depend on salinity here and a lock-exchange type inflow is generated by initialising the salinity to be 25 psu for $x \leq 125$ km and 8 psu elsewhere. The induced horizontal pressure gradient forces a dense bottom current over the sills into the subsequent basins (according to the Baltic Sea from left to right: Arkona Sea, Bornholm Sea, Stolpe Furrow, Gotland Deep). Meteorological forcing and earth rotation are neglected in the simulation. Figure 3.4 shows the salinity distribution after 20 days, when the basins are partially filled and the residual part of the inflow has to propagate above the already denser water in the basins.

The adaptive coordinates configured by the parameters in table 3.2 help here to reduce the vertical advection through the layer interfaces by moving the layer interfaces with stratification. After the basins are partially filled, the overflow will detach from the sea bed and will intrude into its density horizon. The vertical grid adaption aligns the coordinates along the

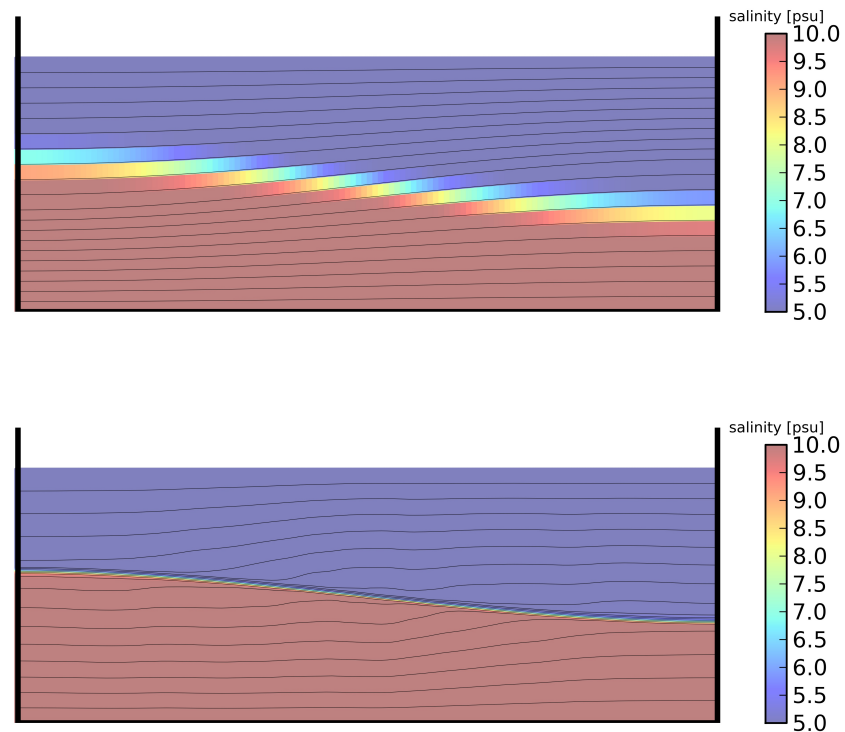


Figure 3.3: The salinity distribution for the fixed grid (upper panel) and the adaptive grid (lower panel) after half of a seiching period. The black lines denote the positions of the layer interfaces.

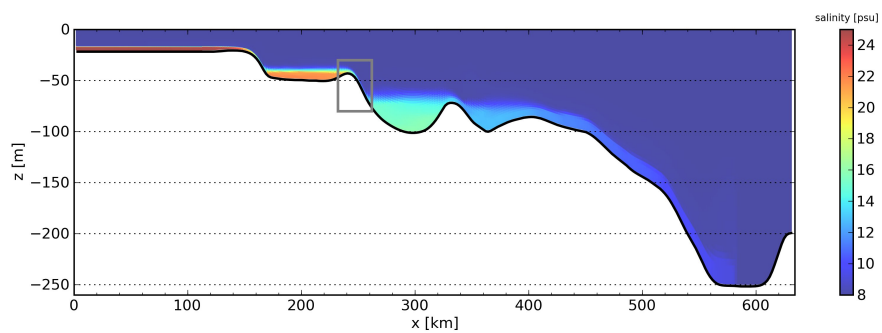


Figure 3.4: Salinity distribution for the two-dimensional overflow experiment after 20 days of simulation. The region within the gray rectangle will be investigated in more detail in figures 3.5 and 3.6.

α_{hor}	α_{lag}	α_{dif}	α_{iso}	c_{N^2}	c_{S^2}	c_d	d_{surf}	d_{min}	t_{grid}
0.1	0.1	0.3	0.1	0.2	0.0	0.3	20 m	0.1 m	3 h

Table 3.2: Parameters for the grid adaption in the multi-basin overflow experiment

isopycnals, thus reducing the density gradient in flow direction.

In figure 3.5 the salinity, horizontal velocity, numerical mixing and physical mixing is shown for the outflow from the first basin (denoted in figure 3.4) in the simulation for sigma-coordinates. The overflow is resolved with few vertical layers and numerical mixing occurs within the overflow. The pycnocline is distorted in the basins due to the bottom-following coordinates and the coarse horizontal resolution. The numerical mixing is highest when the overflow reaches the denser water in the deeper basin, due to relatively large horizontal density gradients and horizontal as well as vertical velocities. Significant reduction of numerical mixing is obtained in the simulation with adaption to stratification and application of all horizontal filters. The important, horizontal filters are the isopycnal tendency and a small Lagrangian tendency here. The Lagrangian tendency reduces the vertical advection through the layer interfaces directly, the adaption to stratification will keep the resolution at the pycnocline and the isopycnal tendency aligns the coordinates along the pycnocline in the horizontal. Figure 3.6 shows a better representation of the density field and less numerical mixing in the overflow for the adaptive grid compared to the σ -grid. The high, numerical mixing at the position where the overflow plunges into the denser water in the deeper basin still occurs as a result of the vertical and horizontal advection in the already adapted grid. However, the numerical mixing at the slope reduces to a thin band of diffusive and anti-diffusive fluxes due to the slightly moving density interface.

Burchard and Rennau [2008] evaluated the vertical integral of the tracer variance decay for the physical and the numerical mixing as measure for the influence of model numerics onto the simulation results. Figure 3.7 shows that adaptive coordinates reduce the amount of numerical mixing in the simulation by more than 45%. The physical mixing is slightly increased because of stronger, remaining density gradients with decreased numerical mixing. In the simulation with the adaptive vertical coordinates, the largest contribution to the overall mixing is shifted from numerically induced to physically induced mixing.

3.1.3.3 Seamount test case

The seamount problem (similar to *Beckmann and Haidvogel [1993]*) is the standard scenario for evaluating pressure gradient errors in non-aligned vertical coordinate systems (*Chu and Fan [2003]*, *Mellor et al. [1998]*, *Song and Wright [1998]*, *Shchepetkin and McWilliams [2003]*). It is a simulation of a horizontally homogeneous stratification in a 5000 m deep ocean with a Gaussian-shaped seamount of 4500 m height (see Fig. 3.8 for an overview). The domain of 66x66 equidistant grid points and a horizontal resolution of 8 km is closed at the horizontal boundaries here and no external forcing is applied. The density variations are only depending on temperature variations here and the initial temperature profile is given by

$$T(z) = 5 + 15e^{z/\delta}, \quad -H \leq z \leq 0, \quad (3.47)$$

where $\delta = 1000$ m and $H = 5000$ m.

The mean kinetic energy of the system

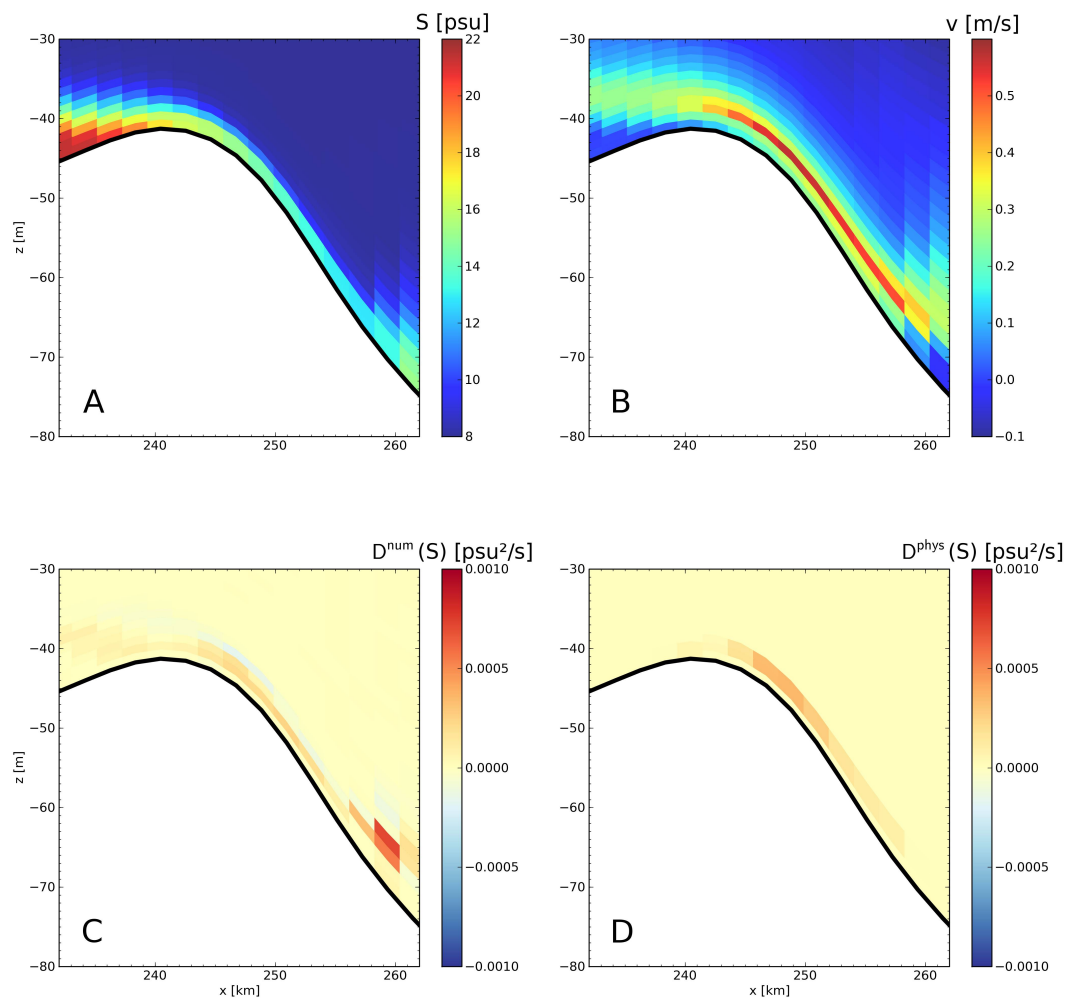


Figure 3.5: Analysis of effective mixing processed inside the small subdomain in figure 3.4 for the simulation with a fixed σ -grid. Panel A: salinity, panel B: horizontal velocity, panel C: numerical salinity variance decay, panel D: physical variance decay. The physical tracer variance decay has been interpolated onto the tracer grid, given as coloured polygons.

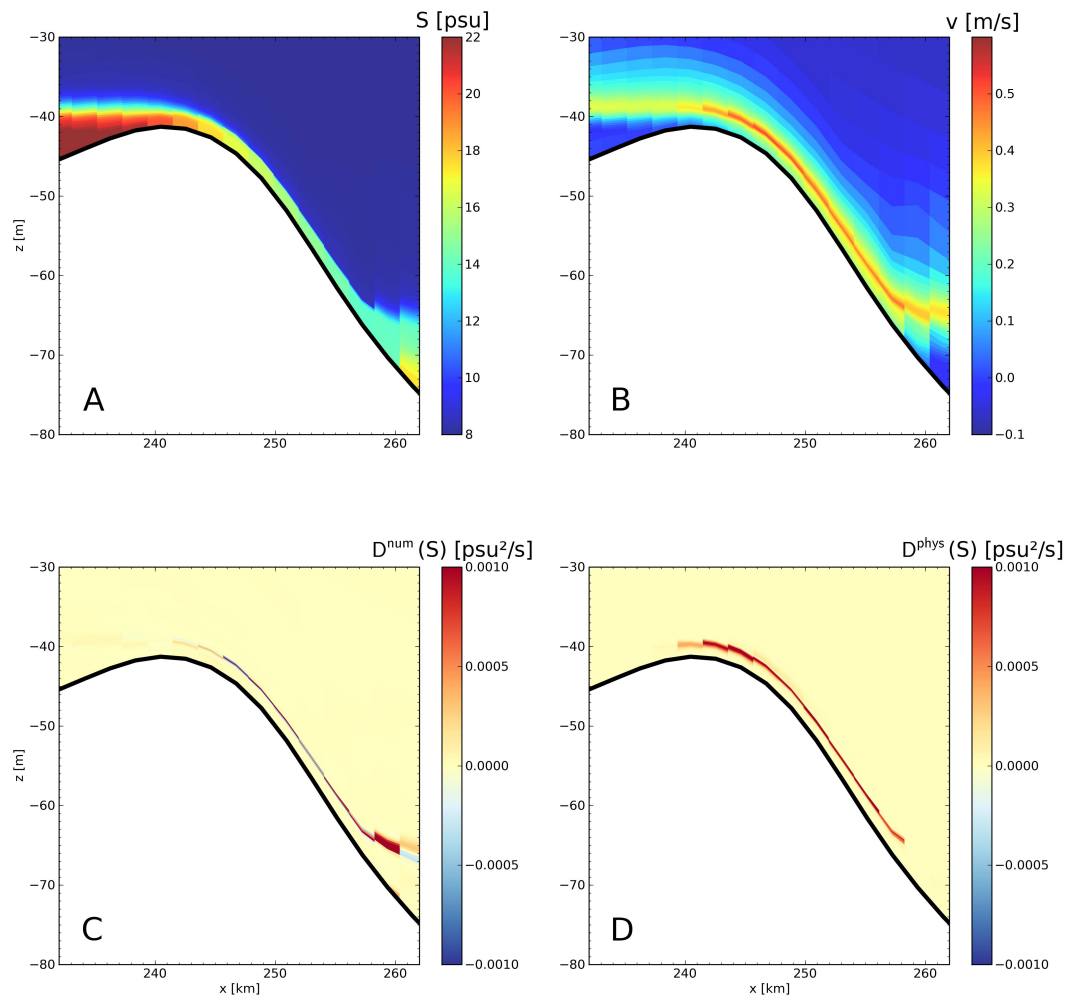


Figure 3.6: As figure 3.5 but for the simulation with an adaptive vertical grid.

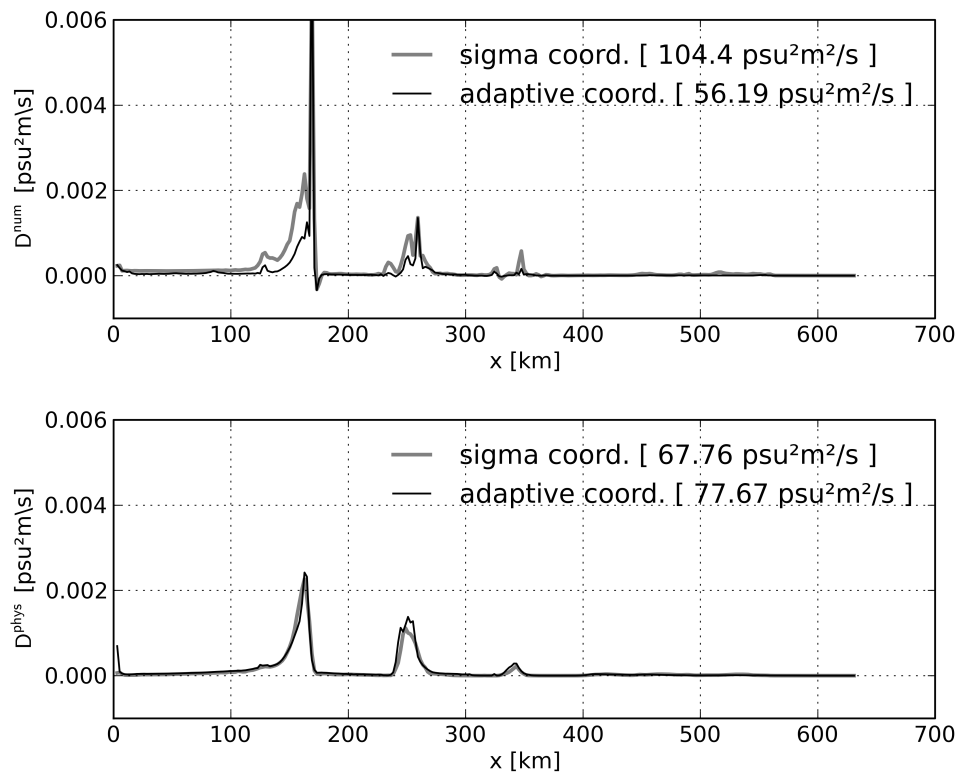


Figure 3.7: Horizontal distribution of vertically integrated and temporally averaged numerical salinity variance decay in the upper panel and physical salinity variance decay in the lower panel. For a quantitative comparison, the spatially integrated and temporally averaged salinity variance decay is given as number in the legends.

$$E_{kin} = \frac{1}{2V} \sum_{i,j,k} [\Delta V_{i,j,k} (u_{i,j,k}^2 + v_{i,j,k}^2)] \quad (3.48)$$

is calculated as measure for the pressure gradient error, where $\Delta V_{i,j,k}$ are the grid cell volumes, where i, j, k denote the grid cell numbering in both horizontal and the vertical direction, $u_{i,j,k}$ and $v_{i,j,k}$ are the cell-mean velocities and V is the total volume of the domain. The evolution of the mean kinetic energy is then shown for 10 days of a full baroclinic simulation, as an indirect measure of the pressure gradient error. The simulation period is kept short in order to have only a small impact by other model techniques as the advection and turbulent mixing schemes. Besides, the grid adaption is expected to reduce the initial error in the pressure gradient calculation without having a direct influence on reducing the long-term evolving vorticity error.

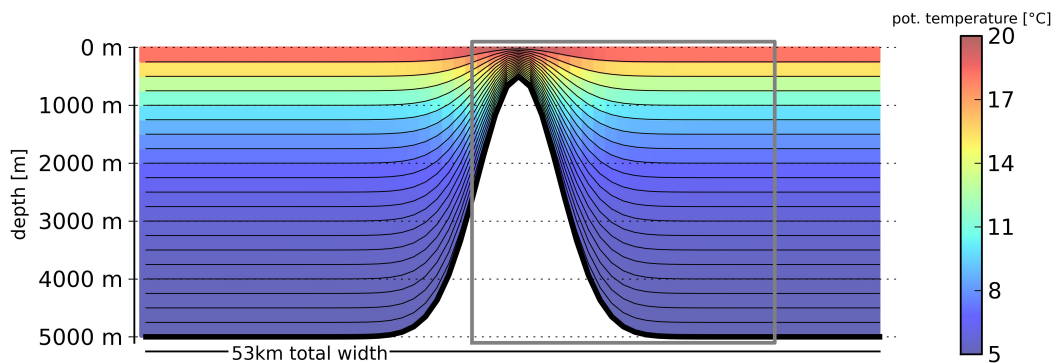


Figure 3.8: The initial temperature distribution for the seamount experiment with 20 vertical σ -layers. The black lines denote the layer interfaces. In further plots, the part of the domain denoted by the gray box is shown.

Different vertical coordinate systems are applied to the system: A σ -grid, a s -grid with zooming to the surface and a set of adaptive grids. For the experiments the pressure gradient formulation (PGF) by *Shchepetkin and McWilliams* [2003] (labelled as ShMcW03 in the following) is applied, since it is widely used in the ocean modelling community. The sigma grid experiment is additionally set up with a standard Jacobian PGF (*Mellor et al.* [1994]) in order to show differences due to an improved PGF.

For all the grid adaptations, the Lagrangian and isopycnal tendency are switched off, but filters for layer heights ($\alpha_{dif} = 0.2$) and interface positions ($\alpha_{hor} = 0.5$) are applied. Both filters allow for a smooth layer interface distribution. A strong filtering of interface positions is assumed to reduce the pressure gradient errors significantly, but will continuously lift the interface of the bottom layers around the seamount. Only a small amount of interface position filtering is applied to keep realistic vertical resolutions here. The table 3.3 shows the parameters used for grid adaptations in the seamount experiments.

The adaptive grids are pre-adapted for the first 50 time steps, starting from a sigma grid, in order to avoid kinetic energy contributions due to an initial movement of the whole grid towards a balanced, initial layer distribution in terms of the adaption. The pre-adaption creates a balance of the impacts by the initial density profile and the bathymetry. The initial

adaption to	c_{N^2}	c_{S^2}	c_d	d_{surf}	α_{hor}	α_{dif}
only filtered interf. position	0.0	0.0	0.0	200m	0.2	0.5
zooming to surface + filter	0.0	0.0	0.3	200m	0.2	0.5
N^2 + filter	0.05	0.0	0.0	200m	0.2	0.5
N^2 + zooming + filter	0.05	0.0	0.3	200m	0.2	0.5
N^2 + strong zooming + filter	0.05	0.0	0.6	200m	0.2	0.5

Table 3.3: Parameters for the grid adaptations in the seamount experiments

temperature profile is interpolated onto the model grid afterwards, as also done for the sigma and the zoomed, but fixed grid.

Classical setup Figure 3.9 shows the layer distribution for the different experiments. For the adaptive grids, the lower layers congregate at the top of the seamount and are released from the sea bed successively with depth as a result of the filter for interface positions. The evolution of kinetic energy in figure 3.10 shows a range of 3.5 orders of magnitude. The highest kinetic energy is found in the sigma coordinate system with the standard Jacobian PGF. A decrease of two orders of magnitude is obtained by using the ShMcW03 PGF. By applying a zooming towards the surface, the kinetic energy is decreased slightly again. The adaptive grids show a generally but only slightly higher kinetic energy than the sigma coordinate experiment with the same PGF, which is mainly related to the model reaction at the surface. The adaption to stratification needs a strong zooming towards the surface to keep resolution at the surface. The vertical optimisation is limited here because there are not enough layer interfaces close to the surface for the initial sigma grid. A good adaptive grid with even less kinetic energy after 10 days of simulation is created by just a zooming towards the surface and the horizontal filtering. The resolution is higher at the surface but still sufficient in the deeper parts of the ocean compared to the adaption to stratification. Compared to the fixed, zoomed grid, the filtering in the adjusted the layer interfaces horizontally, which turns out to be beneficial. In the classical setup, strong pressure gradient errors occur in the surface layer. Although the layer interfaces are not as steep as next to the seamount, the implied along-layer density gradient is strong, due to the exponential temperature profile. A strong vertical density gradient exists by definition in the surface layer, which is not resolved by the model grid.

Mixed-layer setup The standard seamount experiment showed that zoomed, but fixed grids have good performance without the grid adaption overhead, if the region of interest is located at the surface or the bottom. A second experiment with an expanded mixed layer will show the advantages of the grid adaption in such a scenario. The mixed layer is extended to the upper 450 m in the domain in the second experiment. The grid adaption will include now alignment of the grid layers with the thermocline, which cannot be achieved with a zooming to the surface only. Figure 3.11 shows the same experiments as for the standard setup but with a mixed-layer initial temperature profile. Without including a zooming towards the surface for the adaptive grids, the mixed layer is resolved with very few grid layers only. This does not constrain the density profile by the layer distribution, but the grid is pathologic in terms of realistic ocean modelling, when air-sea interactions are expected.

In the temporal evolution of the kinetic energy in figure 3.12, higher kinetic energies can be found due to the pressure gradient error by sloping coordinates at the pycnocline. The

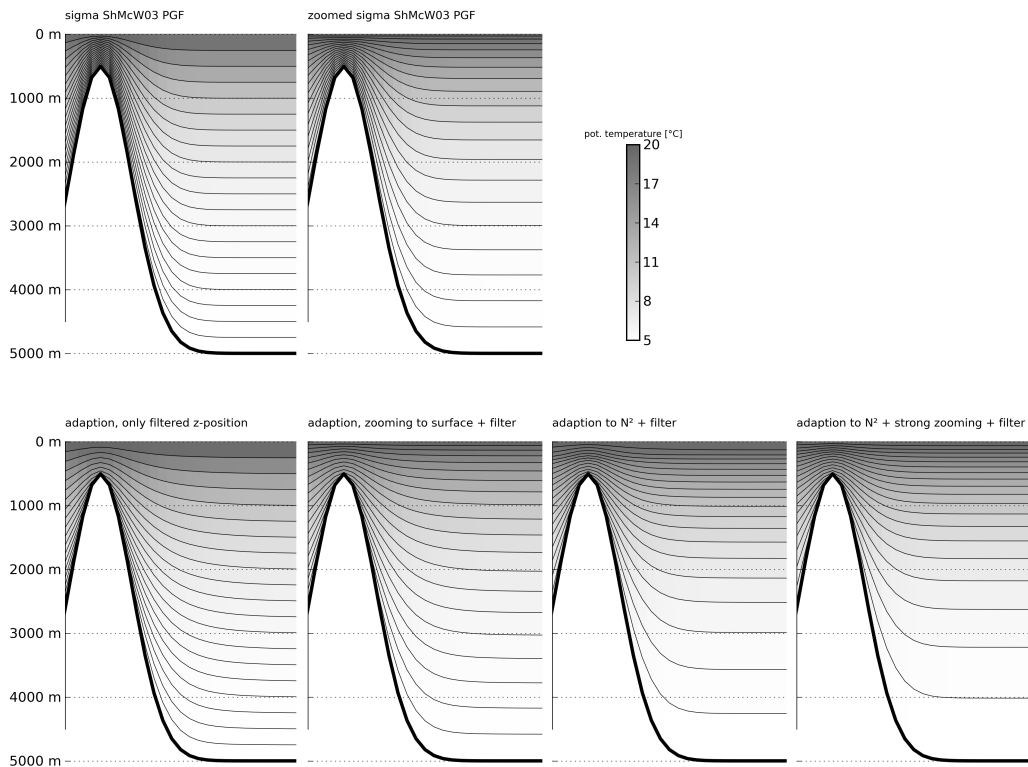


Figure 3.9: The layer distribution (black lines) and the temperature (grayscale) for the different vertical discretisations in the classical seamount experiment.

advantage by zooming towards the surface is insignificant in terms of kinetic energy evolution for the fixed grids. The kinetic energies are still reduced by one order of magnitude with applying a higher-order pressure gradient scheme compared to the standard Jacobian scheme. By applying the grid adaption, a reduction of kinetic energy by again up to almost one order of magnitude can be found. The pure horizontal filtering again induces less kinetic energy than the fixed grids, but the adaption to stratification in addition with the zooming towards the surface is most beneficial here. In the scenario, where a pure zooming to the surface cannot improve the pressure gradient calculation, the adaptive vertical grids show an improvement compared to fixed grids, when adapting the coordinates to stratification. The horizontal filtering is then used as control on the regularity of the grid. Additionally, the resolution at the pycnocline is improved such that all the physical processes at the pycnocline will also benefit in realistic simulations.

3.1.3.4 Coastal upwelling

A last experiment shows the interaction of different processes and the performance of vertically adaptive coordinates in a full-physics scenario. The model domain is an infinitely long channel of parabolic shape and initialised with a horizontally homogeneous temperature stratification. Figure 3.13 shows the temperature distribution for a cross channel slice. At a latitude of 55°N , a wind stress of 0.2 Pa (constant in space and time) in along channel direction is applied at the surface, which causes upwelling at the left hand side of the shown

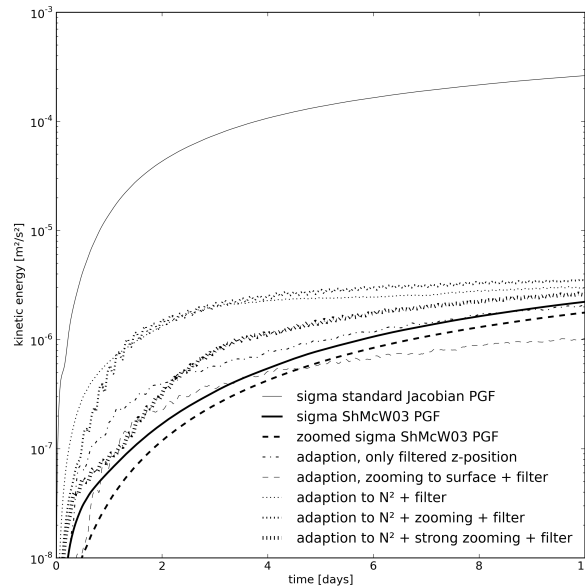


Figure 3.10: The temporal evolution of mean kinetic energy for the different vertical discretisations in the classical seamount experiment.

grid no.	α_{hor}	α_{lag}	α_{dif}	α_{iso}	c_{N^2}	c_{S^2}	c_d	d_{min}	t_{grid}
A)	0.0	0.0	0.3	0.0	0.2	0.1	0.0	0.05 m	1 h
B)	0.0	0.0	0.3	0.0	0.2	0.1	0.0	0.05 m	2 h
C)	0.0	0.0	0.3	0.0	0.0	0.1	0.0	0.05 m	2 h

Table 3.4: Parameters for the grid adaptations in the upwelling experiments

channel slice.

For having an infinite long channel, the model is configured to simulate a minimal set of two tracer and two velocity points in along-channel direction and periodic boundary conditions connecting the down- and up-stream side of the domain. The grid adaption is expected to resolve the temperature stratification well and follows the vertical displacement of the pycnocline. On the other hand, resolution should not be lost at the surface, when the wind-induced surface shear has to be resolved as long as the wind is active. The main goal is to increase the resolution at the pycnocline as well as at the surface such that the numerical mixing is reduced. In the adaptive grid mode, a pre-adaption of the layers to the initial condition of 50 iteration steps was applied. The three discussed adaptive grids are A) adaptive to shear and stratification with a grid timescale of 1 h, B) like A), but with a grid timescale of 2 h C) adaptive to shear only with a grid time-scale of 2 h, with the parameters as listed in table 3.4

In figure 3.14, the mean numerical and physical tracer variance decay are shown for different vertical discretisations. The temperature distribution looks similar for the different vertical discretisations, so that the evaluation of the numerical mixing shows the real advan-

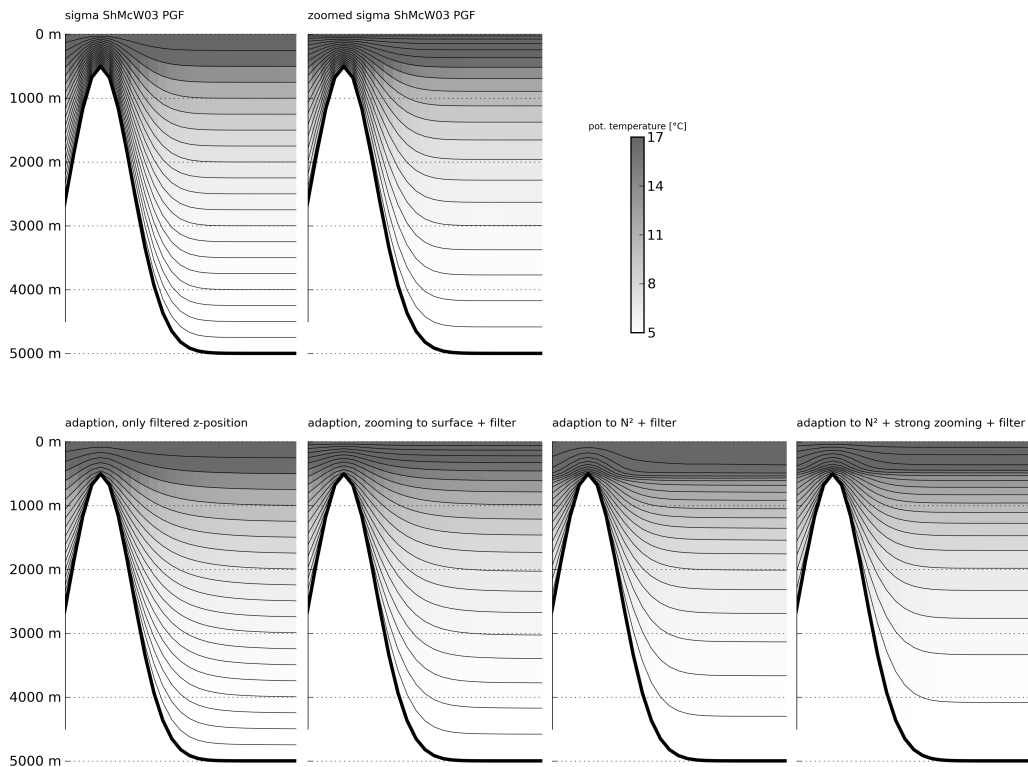


Figure 3.11: The layer distribution (black lines) and the temperature (grayscale) for the different vertical discretisations in the extended mixed layer seamount experiment.

tages regarding long integration periods for realistic simulations.

Most of the curves of the numerical mixing show a characteristic profile as denoted with a)-d) in figure 3.14. In addition, the vertical profiles of the temperature in the centre of the channel are shown with the cross-channel resolution in figure 3.16. The adaptive grid shows a very similar vertical profile, meaning the same physics, as the simulation with the fixed grid.:

- a) During the first 3 hours, the currents due to the onset of wind are developing without generating strong cross-channel flow near the bed. The numerical mixing remains weak in that period. The adaptive grids are further zooming towards a balanced state of grid adaption for the initial density distribution. The used third-order TVD scheme even enhances the gradients by numerical un-mixing with gaining resolution at the pycnocline. The anti-diffusive part of the advection scheme (depending on the choice of the limiter) is adding up to a global un-mixing for a short period at the beginning of the simulation. At the same time, numerical mixing started with the zooming of the layers towards the wind induced shear region near the surface. The integrated effect of the initial layer redistribution is adding up back to zero after 3-4 hours of simulation and can further be compared with the fixed grid simulations. Also *Burchard and Rennau [2008]* found that TVD schemes can increase the integrated tracer variance.
- b) When the cross-channel currents are developing due to rotation and the upwelling is starting, then the dense water is advected in along-layer direction in the near bed

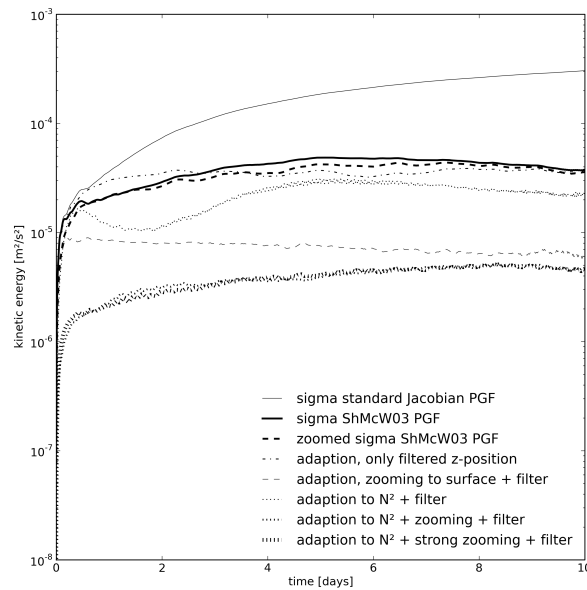


Figure 3.12: The temporal evolution of mean kinetic energy for the different vertical discretisations in the extended mixed layer seamount experiment.

layers. This causes a huge amount of the overall numerical mixing and cannot be decreased by the usage of adaptive vertical grids.

- c) After 12 hours, when geostrophical adjustment is almost established (note that the inertial period is 14.6 h), the upwelling builds an internal pressure gradient balancing the barotropic pressure gradient and mainly turbulent mixing takes place, see times 12.5 h and 15 h in figure 3.15. The numerical mixing is very low during the physical mixing process, thus the temporal mean is decreased slightly.
- d) After 17 hours, the mixing and re-circulation on the shallow, left-hand side of the channel reduces the internal pressure gradient and forces a further movement of dense water with strong vertical component. The numerical mixing increases again for the fixed grid, whereas the grid-adaption follows the vertical movement and additional, significant numerical mixing is avoided. The double resolution, fixed grid also shows only a very small amount of additional numerical mixing.

The fixed grid in double vertical resolution reduces the mean numerical mixing for the shown period by 25%. With grid adaption at the lower vertical resolution, the numerical mixing is another 10% less than for the double vertical resolution. In figure 3.14, also the grid adaption to only current shear is shown partially. The resulting grid (not shown) looks promising, because the shear mostly occurs also at pycnoclines. But the grid adaption is moving the layer interfaces through the pycnocline at the beginning of the simulation, where only the surface shear is target of the vertical grid adaption. The numerical mixing does not destroy the pycnocline completely in this case, but for realistic applications with a multiple on-and off-set of wind events, a background stratification might be mixed up for long integration periods.

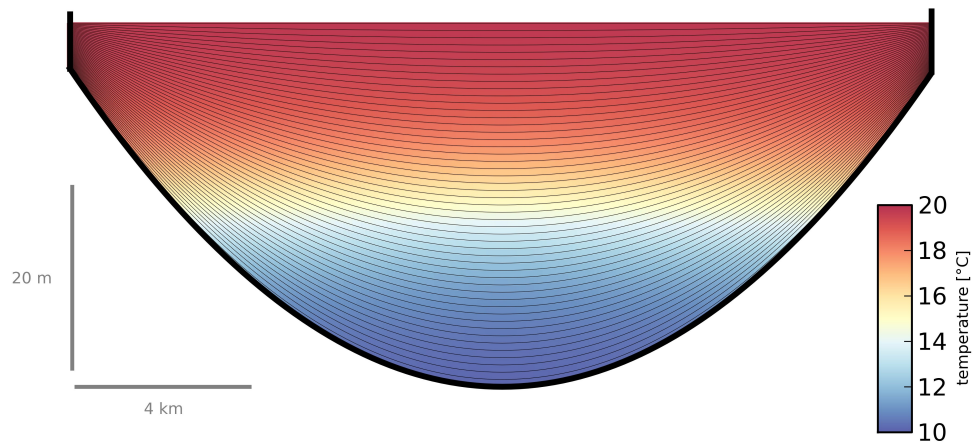


Figure 3.13: Cross-channel slice in the coastal upwelling experiment, showing the initial temperature distribution for 50 σ -layers.

Additionally to the numerical mixing, the mean physical mixing is evaluated for the different grids. All the curves show a similar evolution and are levelling out at about 97% of the overall mixing for the whole model domain. The differences due to the different vertical grids for the physical mixing are much higher than for the numerical mixing. Here, the model grid is determining the performance of the mixing scheme such that even less physical mixing is found for the adaptive grids. In spite of the lack of an analytical or observed solution, the result is still remarkable since the difference between the fixed and the adaptive grids grows when the density interface is displaced.

The coastal upwelling experiment shows the performance of the grid adaption in a full physics simulation. The integration time of 24 hours is short, but the analysis of the numerical mixing shows that the grid adaption reduces the numerical mixing even more than the doubling of the vertical resolution. The simulated physical scenario is not changed significantly by the grid adaption, but the resolution at the pycnocline is higher than for the fixed grid and the grid is following the stratification. This supports a good representation of the physical processes in the model such as mixing in a stratified regime and advection along isopycnals.

3.1.4 Summarising the adaptive vertical coordinates method

A method for using non-uniform adaptive vertical grids is presented here. It is easy to implement the technique into other ocean models than GETM, even for models with unstructured grids. In the latter case, it should be possible to combine horizontal and vertical grid adaption. All other model techniques such as advection, pressure gradient or turbulence closure schemes are not affected by the grid method. The computational overhead is 30-40% in average as calculated from model run time and refers to a compilation with standard optimisation settings running on a standard Linux PC. This is computationally less expensive than doubling vertical resolution of fixed coordinates and still reduces numerical discretisation errors more effectively.

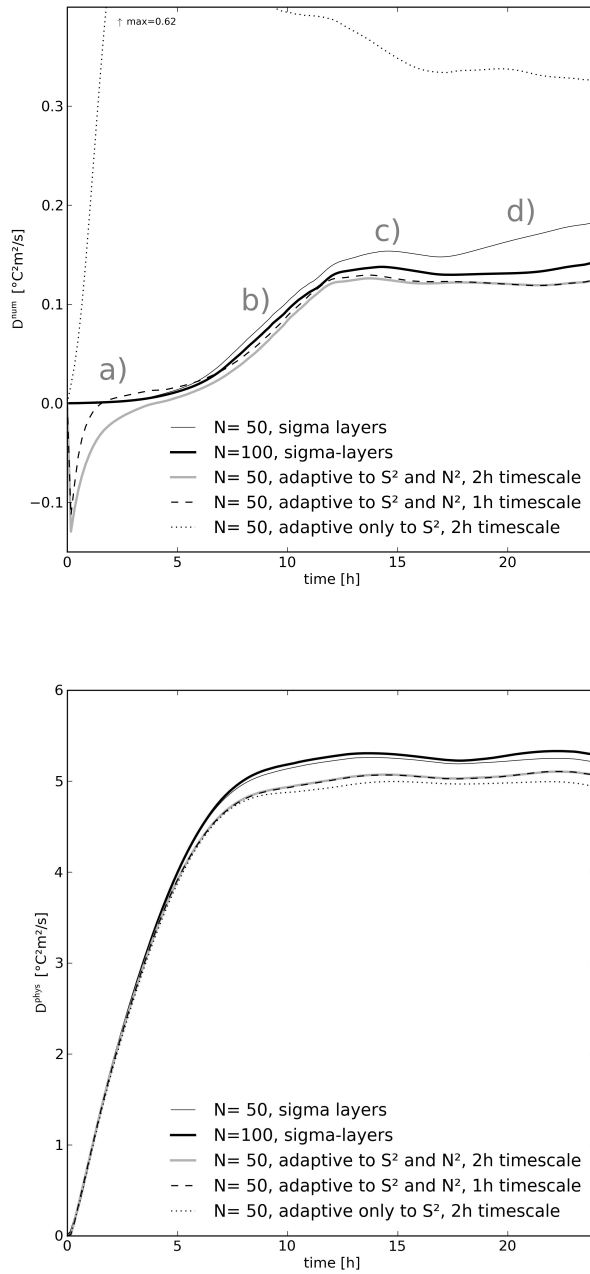


Figure 3.14: The cross-sectionally integrated, numerical (upper panel) and physical (lower panel) tracer variance decay averaged over time for different vertical discretisations for the upwelling experiment. The labels a)-d) denote characteristic periods, which are discussed in the text.

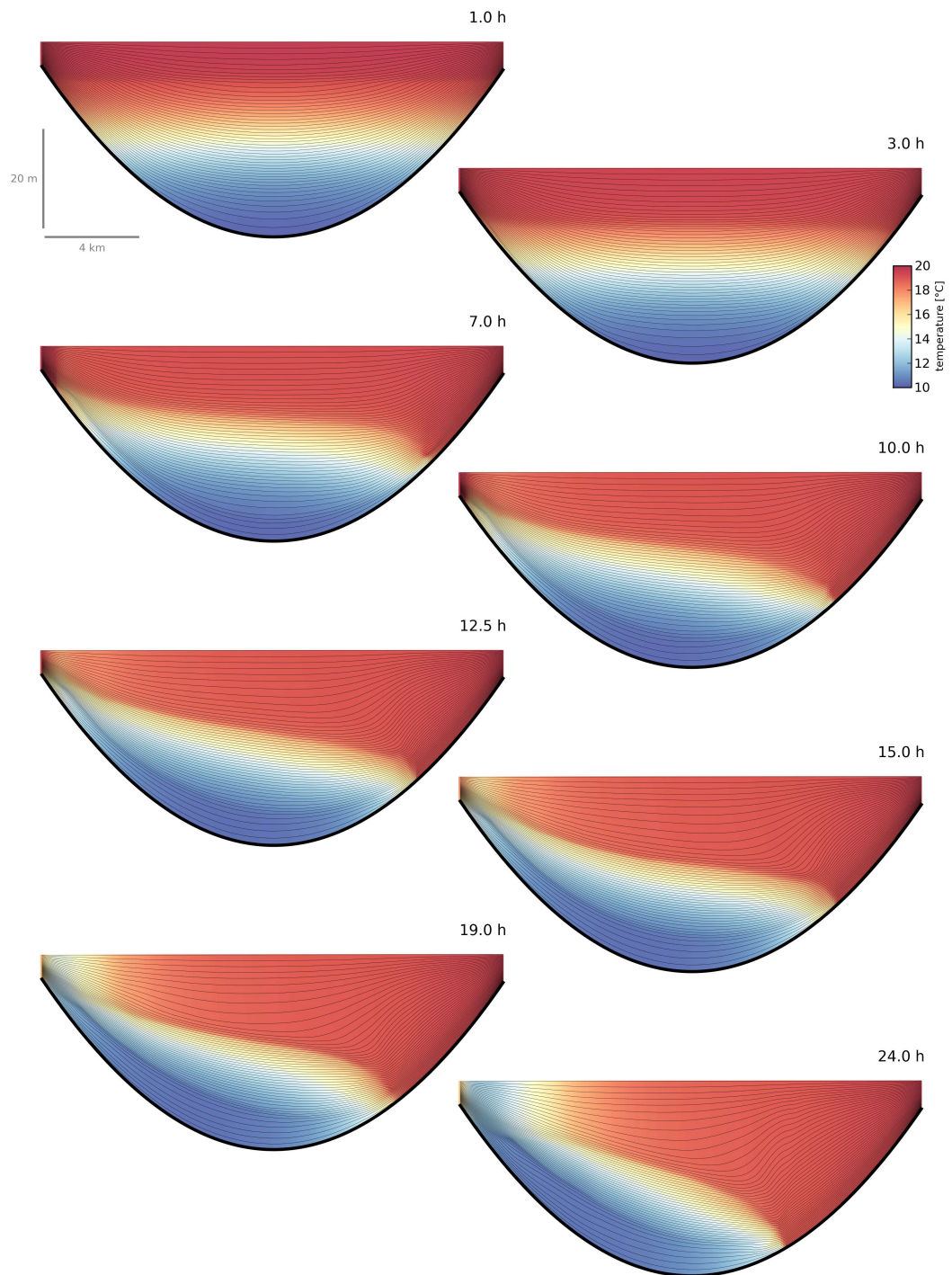


Figure 3.15: Cross-channel slices in the coastal upwelling experiment, showing the temperature distribution for 50 vertical layers and the best grid adaption in terms of the numerical mixing.

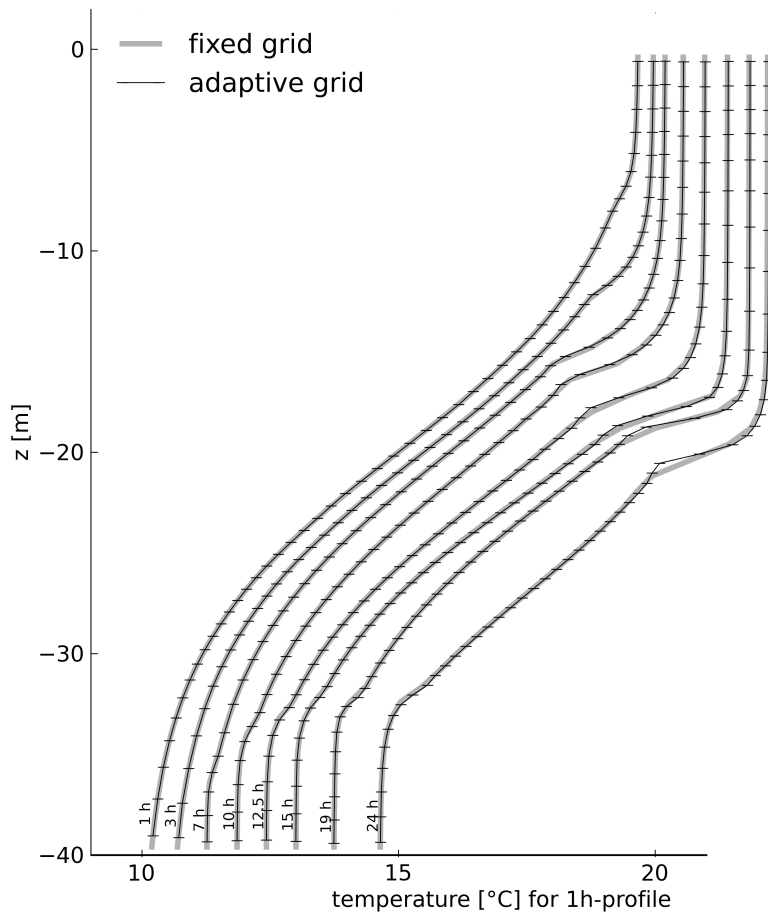


Figure 3.16: The vertical temperature profile for the deepest point in the channel is shown for the adaptive and fixed grid together with two vertical lines denoting the vertical positions of tracer points in the water column. The temperature axis is valid for the 1h profile, each further profile is shifted by 0.5 °C per profile.

It is shown that adaptive vertical grids are reducing the numerical mixing substantially for a set of idealised examples with respect to known problems in ocean modelling such as internal seiche in stratified basins or dense overflows. The physically-motivated tracer mixing in the model can be enhanced by a reduced numerical tracer variance decay. Generally, the numerical mixing is reducing the performance of the turbulent mixing schemes, which have been carefully calibrated by means of theoretical considerations, and field and laboratory data.

Further, one example shows that the pressure gradient error can be considerably reduced by the adaptive grid method. There is evidence that these benefits will reduce uncertainties in model results of stratified seas, which has to be shown for realistic cases in the future.

The optimal parameters controlling the grid adaption are varying depending on the scenario in the experiments shown here. This is due to the different horizontal and temporal scales in the experiments. It turns out to be beneficial to use mainly the grid adaption to stratification and the horizontal filter of grid layer heights. In dynamically active cases, a shorter timescale and Lagrangian tendency for the grid adaption are additionally advantageous in order to decrease the numerical mixing.

The parameter space for improvements of model results needs to be further explored by carrying out tests in realistic applications. The potential of the adaptive grid method is to provide new ways to improve model results for simulations where fixed (bottom-fitted) coordinates give only insufficient results. *Umlauf et al.* [2010] applied the presented grid adaption method presented here to strongly stratified shear flow in order to approach isopycnal coordinates in these parts of the model domain. There, non-isopycnally aligned coordinates give intolerable discretisation errors due to an aliasing between isopycnals and grid lines. For simulations with long integration periods, reduced numerical mixing due to adaptive grids helps to preserve the stratification near steep slopes.

The modeller's knowledge of the expected regimes in the simulation can be used for controlling the grid adaption. A changing regime such as a seasonally moving thermocline or substantial tracer variation due to fluxes through open boundaries results in a dynamical re-distribution of the grid towards the specified optimisation of the vertical resolution.

3.2 Evaluating the internal pressure gradient (PG) calculation

The internal pressure gradient (PG) calculation in non-isopycnal models underlies discretisation errors due to the resolution of the density distribution in the discrete, three-dimensional model grid. In isopycnal models, the simulated density distribution is defined by the discretisation such that any internal pressure gradient error can exist in these models¹.

Within GETM, several PG schemes can be tested in the same numerical environment. In the present section, an overview of the PG calculation of different calculation methods is given. The impacts on the simulation of stratified coastal seas (as e.g. the Baltic Sea or the Black Sea) will be estimated from idealised experiments, here.

In the algorithm suggested in *Stelling and van Kester* [1994] (SvK), the horizontal gradient of buoyancy is calculated with defining non-sloping control volumes of the number of vertical layers in each water column and evaluating the horizontal gradients at the intersections of neighbouring control volumes. For each intersection, the buoyancy gradient is evaluated by linear interpolation of the buoyancy profile in the neighbour column at the T-depth of each

¹Due to the density-class-wise resolution, isopycnal models have to deal with discretisation errors due to small scale diapycnal fluxes and instable stratification.

adjacent cell for both directions. The minimum of the buoyancy gradient for both directions is used then for the internal pressure calculation if both gradients have an equal sign. If both gradients point inconsistently in different directions, the buoyancy gradient in an intersection does not contribute to the internal pressure (as expected for violated hydrostatic consistency and strong stratification). Alternatively, *Slørdal* [1997] proposed to take the mean value of both buoyancy gradients instead of the minimum and reported about a better performance of the internal PG-calculation in idealised cases.

Shchepetkin and McWilliams [2003] categorised the second-order density-Jacobian methods for calculating the buoyancy gradient in the numerical grid before the vertical integration over the upper water column into a standard Jacobian (SJ) method (as proposed by *Blumberg and Mellor* [1987], *Mellor et al.* [1994]) and a weighted Jacobian method (as proposed by *Song* [1998]). These second-order methods for calculating the PG-gradient are common in coastal ocean modelling and computationally less expensive than higher-order methods. In GETM, both second-order methods are implemented; for the comparisons in the present thesis, the standard Jacobian (SJ) method will be used as well-known, but uncertainty-prone reference in the coastal ocean modelling community. A widely used method for calculating the internal PG force is proposed in *Shchepetkin and McWilliams* [2003] (ShMcW), who use a fourth-order approximation of the buoyancy distribution by monotone, cubic polynomials. *Shchepetkin and McWilliams* [2003] also provided a promising analysis of results in idealised simulations with their proposed PG scheme.

A common type of model experiment for estimating the PG errors is to evaluate currents and kinetic energy for homogeneous stratification over variable bathymetry (*Chu and Fan* [2003], *Mellor et al.* [1998], *Song and Wright* [1998], *Shchepetkin and McWilliams* [2003]). The kinetic energy after a reasonable simulation period is taken as measure for the strength of the pressure gradient errors. The contribution of the PG errors to density mixing is so far not well estimated. If the PG errors contribute largely to density mixing, then the resulting kinetic energy as used indicator may be limited since the potential for an erroneous PG acceleration is reduced. Especially in stratified coastal seas, mixing at pycnoclines possibly due to PG errors determines (and possibly misdetermines) the vertical transport of nutrients and oxygen as being crucial for describing the marine ecosystem.

For the simulation of the Baltic Sea (as presented in chapter 4), the internal PG has to be reduced such that the stratification is maintained and the dense bottom currents are accelerated realistically. Two idealised simulations are presented below in order to estimate the performance of pressure gradient errors in stratified regimes as found in the Baltic Sea.

3.2.1 Idealised Simulation of a sloping pycnocline

The internal PG calculation method from *Stelling and van Kester* [1994] will by definition underestimate the hydrostatic pressure below pycnoclines. For the simulations of dense bottom currents, an underestimation of the internal pressure gradient will result in a reduced speed of the gravity current. In the present experiment, the pressure gradient errors for a sloping pycnocline over continuously sloping bottom is evaluated for two different orientations of the pycnocline slope, sigma coordinates and adaptive vertical coordinates and a vertical change of salinity of 5 g/kg over a distance of 3 m and in a second set of experiments a distance of 10 m. For a used constant temperature of 0 °C, the salinity jump is equivalent to a density jump of 3.9 kg/m³. As measured by *Umlauf et al.* [2007], natural vertical gradients in the Baltic Sea can be even stronger than the present cases. In fig. 3.17, the salinity and layer distribution and the corresponding acceleration for different pressure gradient

schemes is shown for different vertical coordinate systems and different pycnocline slope orientations. The simulations with the adaptive coordinates do not contain the full adaptation, but a pre-adaptation with 200 iterations towards the vertical density gradient, the distance to bottom and surface and the horizontal filters for layer thicknesses and layer interface positions. Table 3.5 lists the used parameters for the grid adaptation. Since qualitative trends in the resulting acceleration should be evaluated here, the grid adaptation is set stronger than typically used in more realistic simulations. The implementation of the grid adaptation in the setup with a permanently sloping bottom does not allow for an isopycnal layer distribution here. The accelerations due to the pressure gradient are compared with the analytical solution in fig. 3.17, therefore a fully baroclinic simulation using the full grid adaptation is not possible.

α_{hor}	α_{lag}	α_{dif}	α_{iso}	c_{N^2}	c_{S^2}	c_d	d_{surf}	d_{min}	t_{grid}
0.2	0.0	0.5	0.0	0.4	0.0	0.4	10 m	0.2 m	0.5 h

Table 3.5: Parameters for the grid adaptations in the sloping pycnocline experiments

As expected, the SvK method is underestimating the bottom acceleration of the density field, which is not seen for the other PG methods. In the interface, all the different PG methods show discretisation problems as already indicated in the salinity distribution above. Due to the discretisation, the along-layer salinity distribution is not smooth in the model grid. For similar isopycnal and bottom slopes, the acceleration around the density interface widens up from 3 m to 6m for the SJ and ShMcW methods and even up to 10m for the SvK method. For a pycnocline sloping oppositely to the bottom, the SJ and ShMcW methods show overshoots of the acceleration above and below the density interface. Although the ShMcW method uses a higher-order scheme, the result is qualitatively the same and quantitatively similar to the SJ method. The SvK method is not showing an overshooting acceleration but is again underestimating the acceleration at the bottom. The overshoots as seen for the oppositely sloping pycnocline are accelerating an additional shear at the pycnocline, which will artificially enhance the mixing of the pycnocline (see in more detail below). The use of adaptive coordinates is improving the performance of the SvK scheme for both orientations of the pycnocline. The overshoots for the oppositely sloping pycnocline are reduced significantly by the grid adaptation when using the SJ and ShMcW methods. All the different methods tend to converge against a common solution for the acceleration in the adapted discretisation.

The results for a wider interface in fig. 3.18 shows that for all pressure gradient schemes, the acceleration in the discrete model grid tends to be closer to the analytical solution and closer to each other. Again the SvK method underestimates the PG acceleration at the bottom. Some qualitative differences can be found for opposite slopes of the pycnocline and the bottom: The overshoots of the SJ and ShMcW scheme are strongly reduced, which results in 50% stronger PG acceleration overshoot for the SJ scheme compared to the ShMcW scheme in panel C. Hence, the estimation of the PG error and the performance ranking of PG schemes is depending on the strength of the vertical density gradient (as found already in section 3.1.3.3 for the seamount experiments). Finally, panel D shows a convergence of the results of all the different PG schemes towards the analytical solution for the adaptive vertical grids.

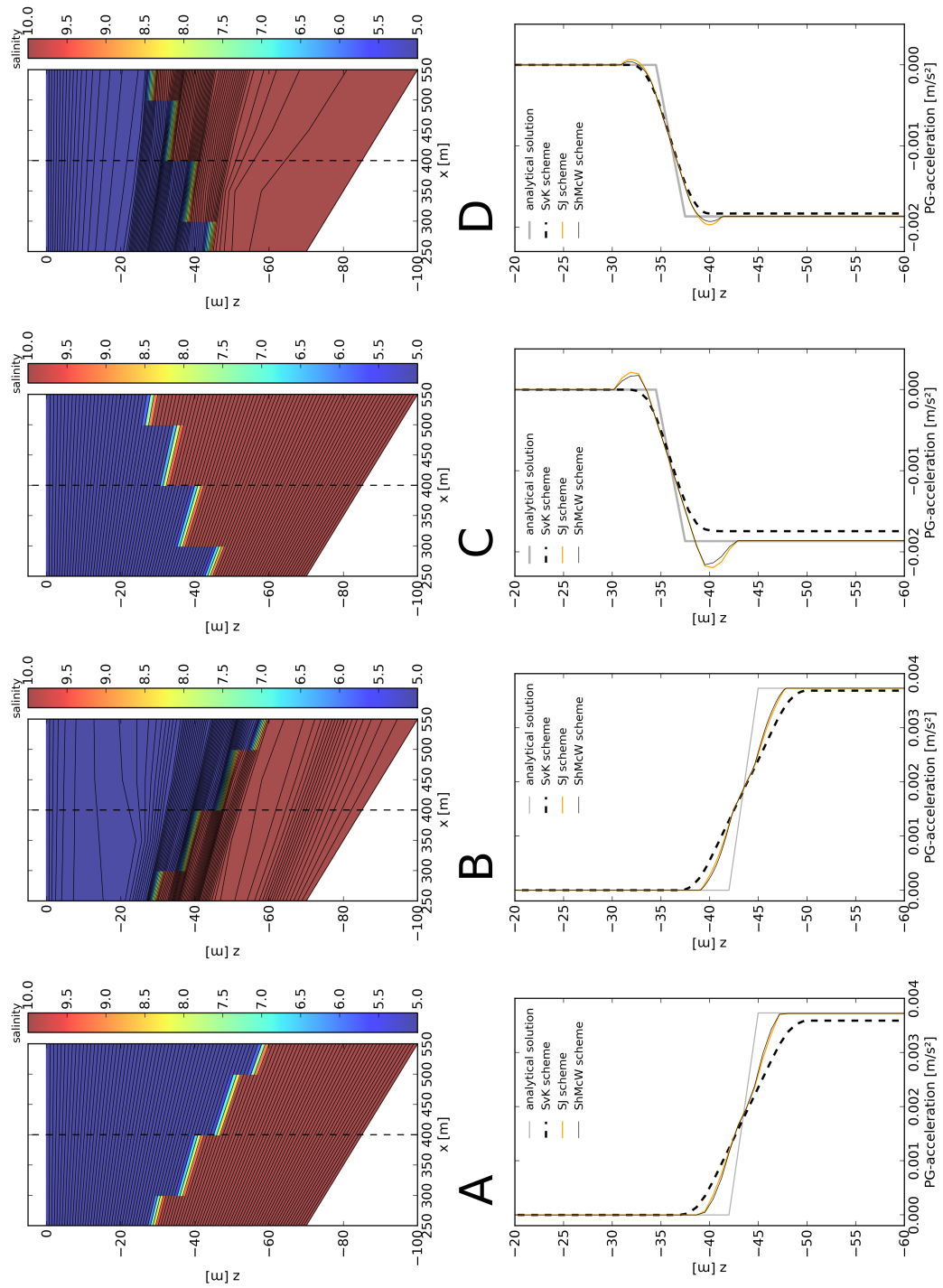


Figure 3.17: The salinity and layer distribution with a 3 m density interface and the corresponding acceleration for different pressure gradient schemes is shown for sigma coordinates (A,C) and adaptive coordinates (B,D). The isopycnal slope is oriented as the bottom slope for panels A and B and is oppositely oriented than the bottom slope for panels C and D. The lines in the corresponding, lower panels shows the PG acceleration from the analytical theory and for different PG schemes: *SvK method* as proposed by *Stelling and van Kester [1994]*, *ShMcW method* as proposed by *Shchepetkin and McWilliams [2003]* and *SĴ method* for the standard Jacobian (*Blumberg and Mellor [1987]*)

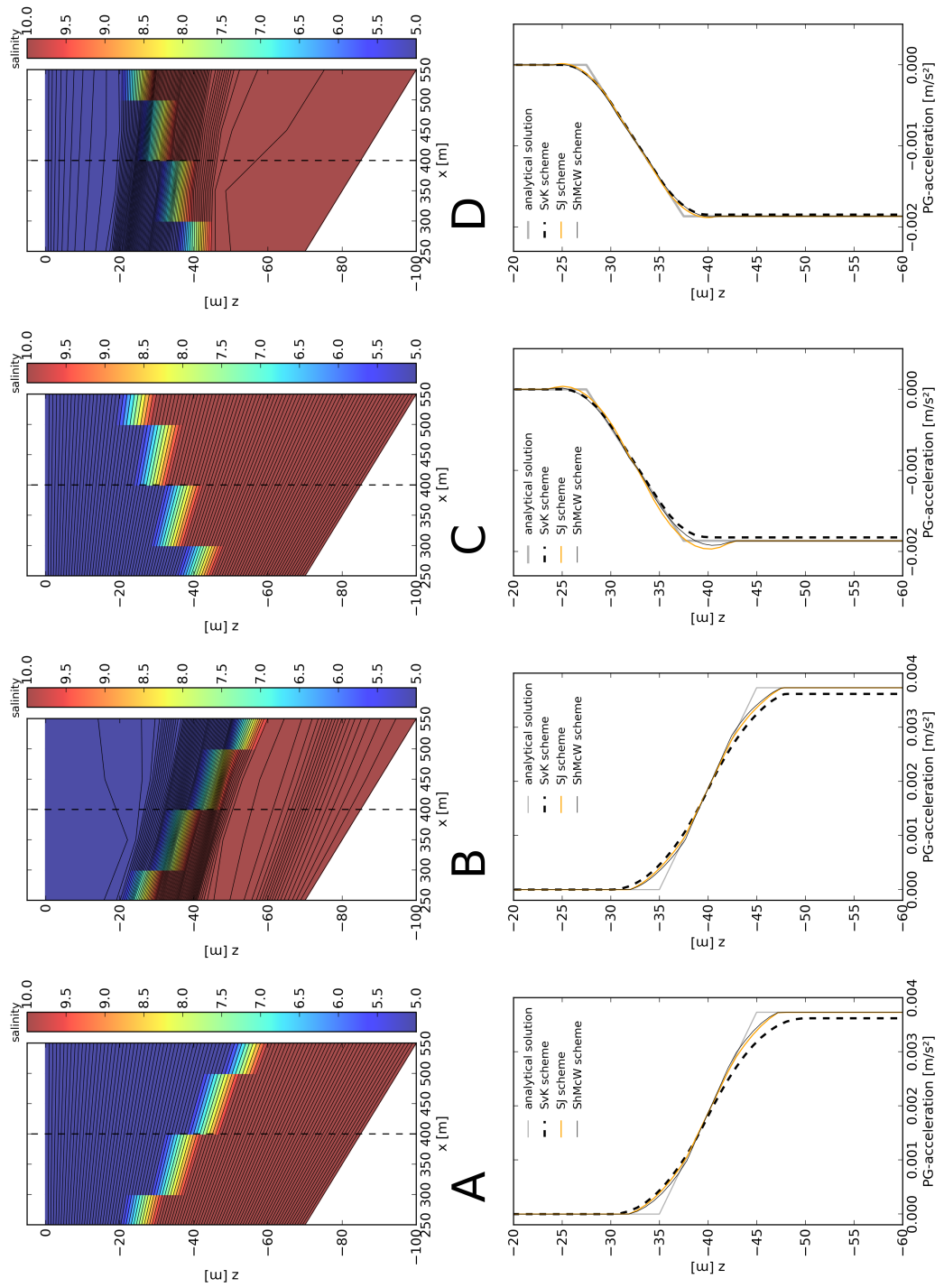


Figure 3.18: similar as fig. 3.17, but for a 10 m density interface

α_{hor}	α_{lag}	α_{dif}	α_{iso}	c_{N^2}	c_{S^2}	c_d	d_{surf}	d_{min}	t_{grid}
0.5	0.0	0.2	0.0	0.1	0.0	0.6	20 m	0.2 m	1 h

Table 3.6: Parameters for the grid adaptations in the idealised Gotland Basin experiment

3.2.2 PG errors during stagnation in an idealised Gotland Basin

A second simulation will evaluate the erroneous PG acceleration for horizontally homogeneous stratification in a partially realistic regime. The setup uses the bathymetry of the Gotland Basin in the Baltic Sea (see fig. 3.19), enclosed artificially at the borders of the model domain. The horizontal resolution is 1 nautical mile and the model resolves the domain vertically by 50 vertical layers, the same resolution as used in chapter 4 for the high-resolution, realistic hindcast simulation. In one of the experiments, pre-adapted vertical coordinates (50 iterations in the pre-adaptation) with the parameters as listed in table 3.6 are used. A climatological mean salinity profile is interpolated onto each water column, which results in a horizontally homogeneous density distribution for a used constant temperature of 10 °C. Analytically, no acceleration is expected for a homogeneous density distribution without external forcing, but due to discretisation errors, currents will be accelerated where the steep vertical layer interfaces are crossing the pycnocline.

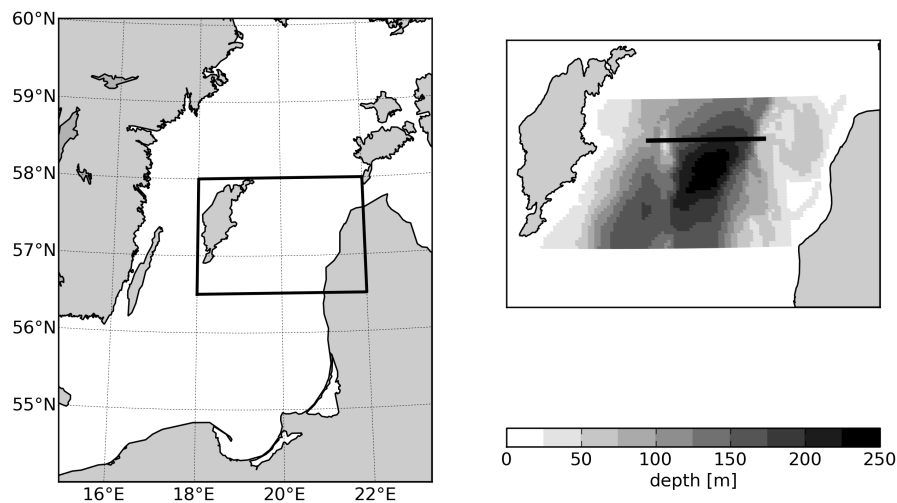


Figure 3.19: Location and bathymetry of the idealised Gotland basin model.

Fig. 3.20 shows the salinity distribution and the PG acceleration due to PG errors in the idealised Gotland Basin. Similar to the sloping pycnocline experiments above, the SJ and ShMcW PG schemes are forcing a shear flow at the pycnocline. The ShMcW scheme performs quantitatively better than the SJ scheme although both schemes show the same qualitative result. Additionally, the stronger accelerations are directed with the along-layer salinity gradient, which increases the potential for numerical mixing at the pycnocline. The results using the SvK scheme are not shown here, since the PG accelerations are one order of magnitude less than for the SJ and ShMcW scheme. Using adaptive vertical coordinates reduces the

pressure gradient errors as found consistently in the studies presented above. Again similar to the sloping pycnocline experiments, the shear flow acceleration is almost vanished for a better representation of the density field in the adapted grid. The stronger accelerations in the regions, where the pycnocline reaches the bottom cannot be reduced by the adaptive coordinates, since the bottom layer slope is always fitted to the bottom slope.

The numerical mixing and turbulent mixing can be evaluated as vertically integrated tracer variance decay using the definitions (3.36) and (3.35). The vertically integrated numerical tracer variance decay χ^{num} is calculated here as

$$\chi^{num} = \sum_{k=1}^N h_k D_k^{num}, \quad (3.49)$$

where k denotes the index over the N vertical layers with the layer heights h_k within the water column. The vertically integrated turbulent tracer variance decay χ^{phys} is calculated as

$$\chi^{phys} = \int_{-H}^{\eta} D^{phys} dz. \quad (3.50)$$

In the upper two panels in fig. 3.21, the numerical and turbulent mixing are plotted on a log scale as mean values over the first inertial period. The numerical mixing due to the acceleration of the density field by PG errors is 2-3 orders of magnitude larger than the induced turbulent mixing due to the increased shear at the pycnocline. However, the turbulent mixing shows a signature along the steep slopes, which contributes to the erosion of the pycnocline. The lower panel in fig. 3.21 shows the maximum magnitude of the velocity in each water column after one initial period of simulation. The currents induced by the PG errors reach values of up to 10 cm/s. During stagnation periods, the background circulation is measured to be less than 6 cm/s (*Hagen and Feistel [2004]*), hence the numerically induced currents are of the same order of magnitude as the realistic circulation or even larger.

3.2.3 Conclusion on internal PG errors

As found in the idealised experiments above, the internal PG-errors are impacting the coastal ocean simulation in three different ways:

artificial currents: For steep slopes and strong vertical density gradients, the accelerated artificial currents by the internal PG calculation can reach the magnitude of natural currents in non-tidal seas such as the Baltic Sea.

numerical mixing: The accelerated current is directed along a strong along-layer density gradient (see Fig. 3.20). Hence, strong numerical mixing is induced at the steep slopes not only due to upwelling dynamics but also due to PG errors.

induced, artificial turbulent mixing: The induced currents also induce an additional vertical shear at the pycnocline. The resulting turbulence is partially suppressed by the stratification. However, even a small turbulent diffusivity can produce a permanent erosion of the stratification.

Supporting the findings in section 3.1, the adaptive vertical coordinates improve the representation of the density field in the discrete model grid and reduce the pressure gradient errors significantly. Additionally, an adapted vertical discretisation shows a convergence of

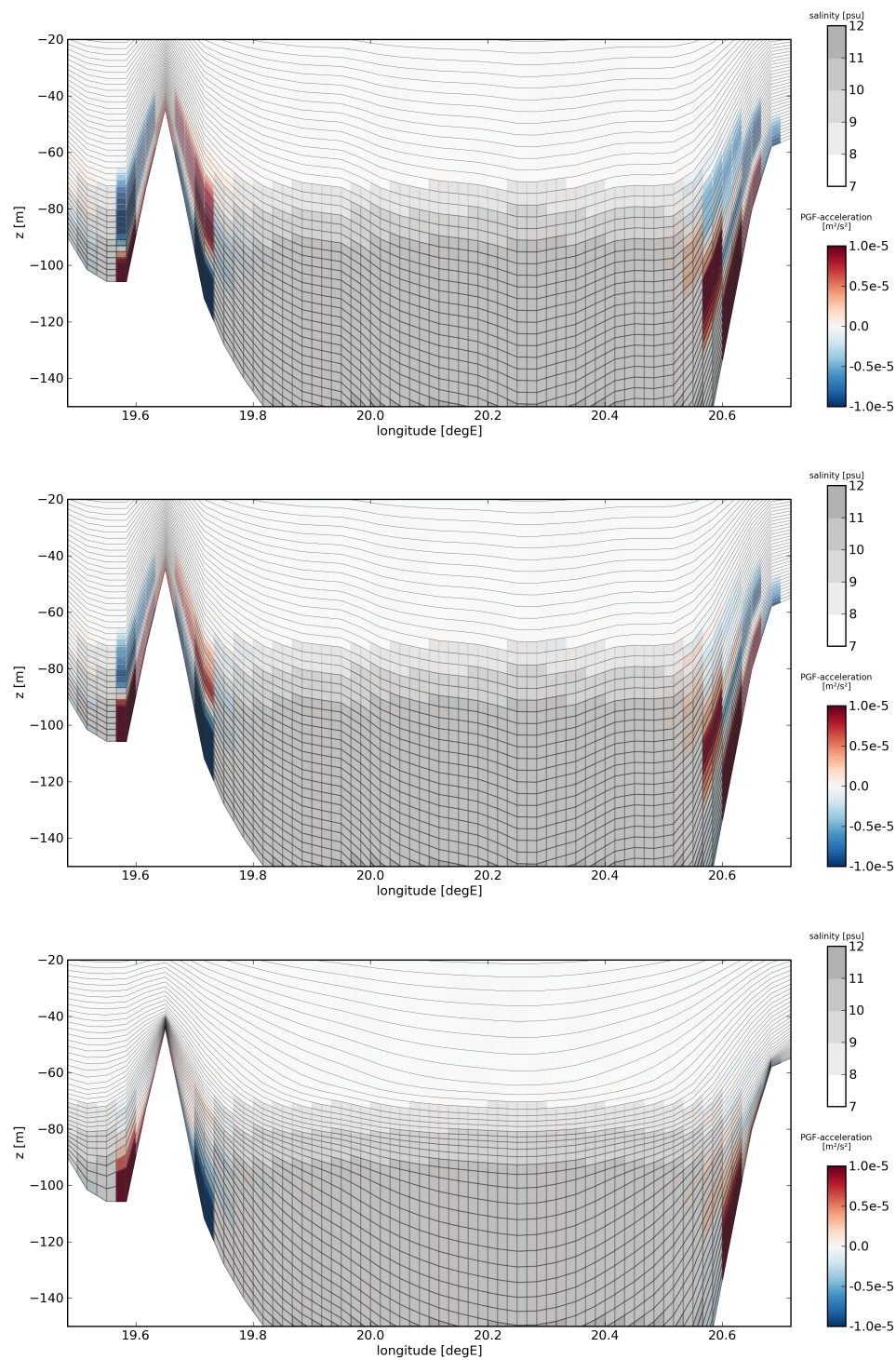


Figure 3.20: The acceleration due to the internal pressure gradient for a transect through the Gotland basin as shown in figure 3.19 for the SJ scheme (upper panel), the ShMcW scheme (middle panel), and the ShMcW scheme in an adapted grid (lower panel).

different PG schemes towards the real acceleration due to the internal PG. It is expected here,

that for the realistic hindcast study in the next chapter, the adaptive vertical coordinates will reduce the artificial mixing of the permanent stratification in the Baltic Sea. The idealised studies give evidence that the simulation of the deeper basins in the central Baltic Sea with sigma coordinates is subject to strong artificial tracer mixing.

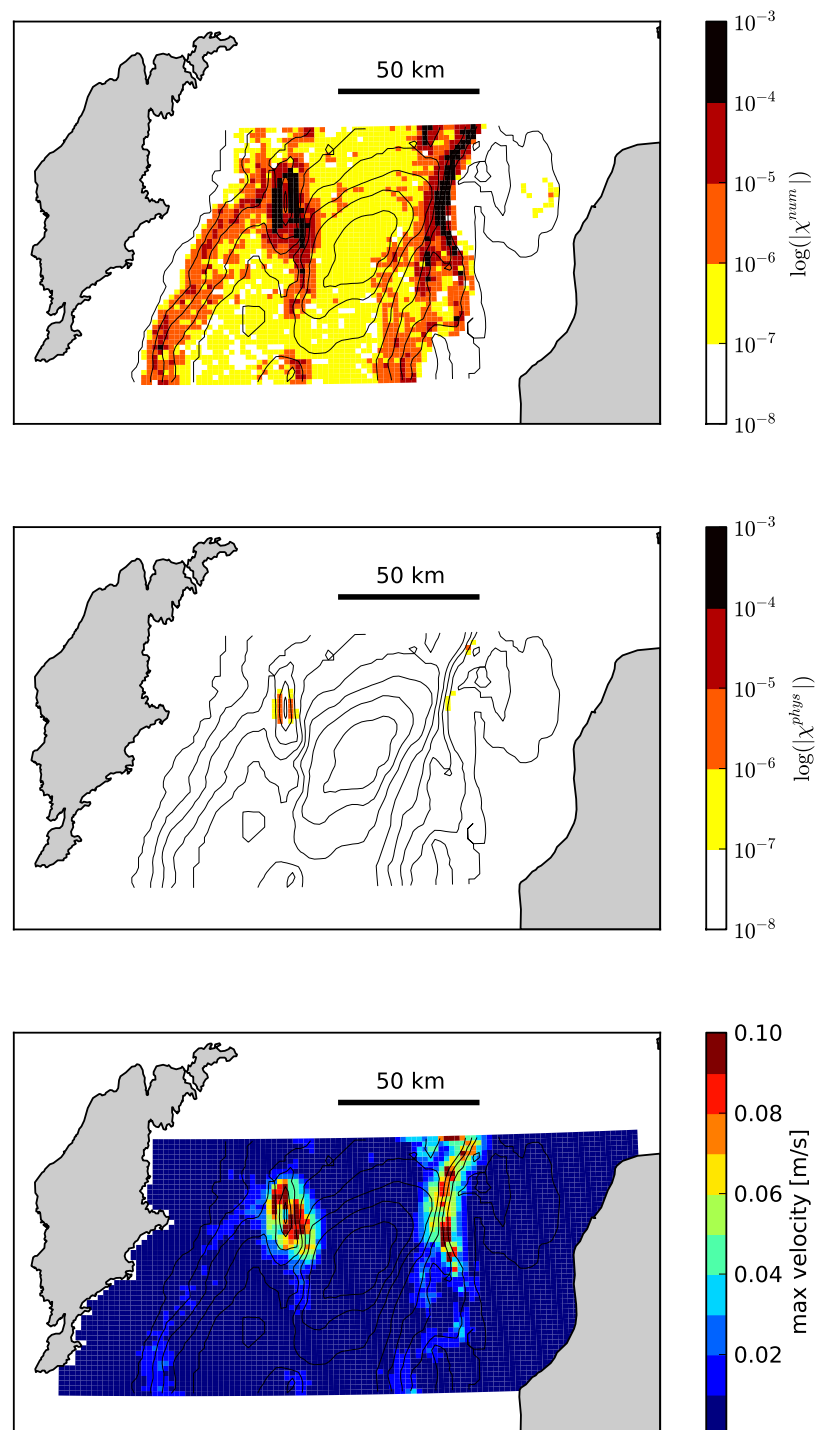


Figure 3.21: The vertically integrated numerical salinity variance decay (upper panel, temporal mean over the first inertial period), the vertically integrated turbulent salinity variance decay (middle panel, temporal mean over the first inertial period) and the maximum magnitude of the velocity vectors for each water column after one initial period (lower panel) for the simulation of horizontally homogeneous stratification in an idealised Gotland Basin.

4 Realistic modelling of inflows into the Baltic Sea

The aim of the present study is to apply the adaptive vertical coordinate method for realistic modelling of the major Baltic inflows in 2003 and evaluate the performance for two different horizontal resolutions against simulations with fixed sigma coordinates. Similar to *Rennau and Burchard* [2009], we want to compare physically-induced and numerical mixing, also in order to identify the mixing hotspots in the Baltic Sea. From the realistic simulations, as evaluated below, the hydrography of the major inflows in 2003 is presented. It is shown that the complex transverse dynamics of channelled gravity currents (as observed by *Paka et al.* [1998] for the Stolpe Furrow, by *Umlauf et al.* [2007] for the Arkona Sea and by *Reissmann et al.* [2009] for the Bornholm channel) is poorly resolved by fixed sigma-coordinates, in contrast to simulations with proper choices for vertically adaptive grids (see *Umlauf et al.* [2010]). A realistic scenario of gravity currents in channelised bathymetry is presented in the manuscript, which supports the findings for an idealised scenario from *Umlauf et al.* [2010].

4.1 Methodology

The experiments in this study are undertaken with the three-dimensional numerical model GETM (General Estuarine Transport Model, see *Burchard and Bolding* [2002]). The model is equipped with state of the art numerical schemes for tracer and momentum advection and the internal pressure gradients. It is important for the present study that the model has the recently developed adaptive vertical coordinate method (*Burchard and Beckers* [2004], *Hofmeister et al.* [2010b]) implemented together with the tracer mixing analysis method as proposed in *Burchard and Rennau* [2008]. For the Baltic Sea application we use the k - ε turbulence model with a steady-state Richardson number of 0.25 (*Umlauf and Burchard* [2005]) coupled to the second moment closure suggested in *Cheng et al.* [2002]. In the case of the higher resolution studies, it turned out that the simulation with adaptive coordinates showed a lack of mixing in the deep parts of the central Baltic Sea, which can be easily explained by non-parameterised internal mixing processes due to e.g. internal waves, eddies (*Reissmann et al.* [2009]) or possibly double-diffusive mixing (*Wieczorek et al.* [2008]). As a simple parametrisation, we applied a background turbulent kinetic energy level of $10^{-6} \text{ m}^2/\text{s}^2$ in the k - ε -model together with limiting the turbulent length scale by the stratification (see *Galperin et al.* [1988] and *Umlauf and Burchard* [2005] for details). The parametrisation feeds back into the turbulent diffusivity as a non-constant contribution depending on stratification (advocated in *Lass et al.* [2003] for analysing measurements and similarly used by *Meier* [2007] in Baltic Sea modelling). The used parametrisation leads to a vertical tracer diffusivity in the deep water of the Baltic Sea of about $7 \times 10^{-6} \text{ m}^2/\text{s}$, which is in accordance with estimations from measurements (*Matthäus* [1990], *Axell* [1998], *Lass et al.* [2003]).

One of the aims of the present study is to reproduce the dynamics of the major Baltic inflows reaching the deep basins. For that reason, the year 2003 is chosen since two well

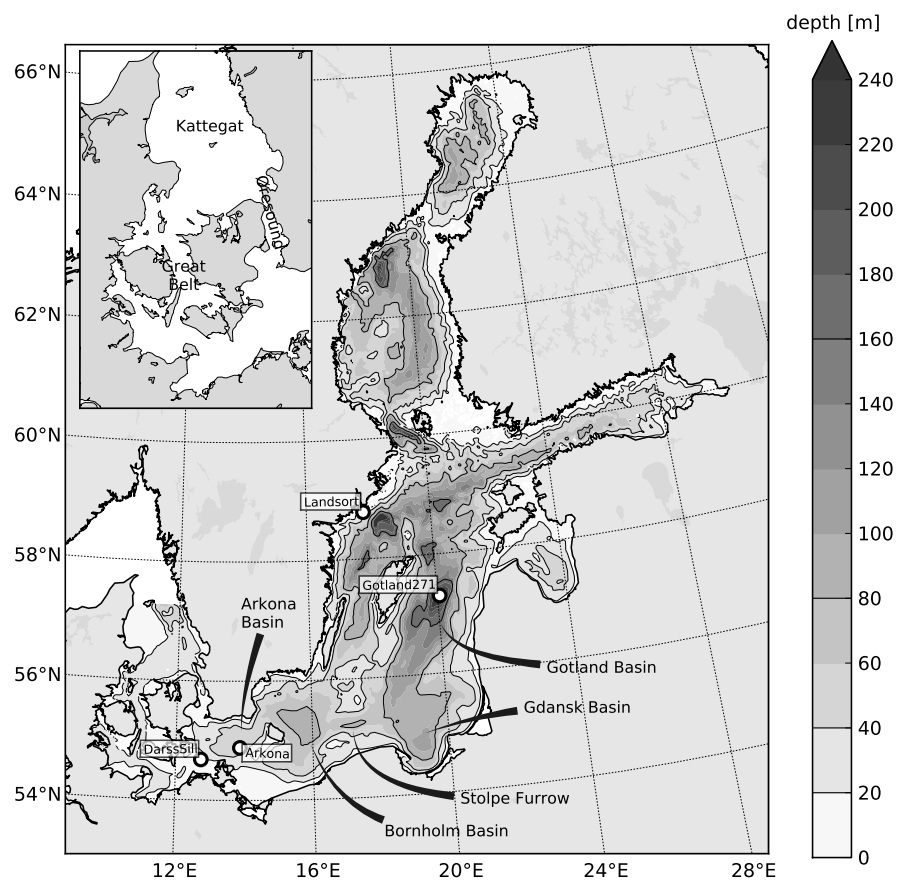


Figure 4.1: A map of the Baltic Sea including the bathymetry (for illustration purposes, the depth scale is clipped at 240 m) and the coastlines of the Belt Sea inserted as small map.

observed major inflows occurred (*Feistel et al.* [2004]): a major cold inflow starting in the first half of 2003 and a major warm inflow in the second half of 2003. The simulation period is extended towards September 2002 to spinup the model.

Two basic model setups are used here, one using 2 NM (nautical miles, $\Delta\phi = 1/30^\circ$, $\Delta\lambda = 1/15^\circ$) horizontal resolution and one using 1 NM ($\Delta\phi = 1/60^\circ$, $\Delta\lambda = 1/30^\circ$) horizontal resolution, which barely resolves the baroclinic Rossby Radius in the central Baltic Sea (*Fennel et al.* [1991]) in both cases. 50 terrain-following, vertical layers are used in both setups, which resolves the Arkona Basin with 1 m, the Bornholm Basin with 2 m and the Gotland Basin with 5 m in the vertical for an equidistant layer distribution. The bathymetry is based on the data from *Seifert and Kayser* [1995], where structures are filtered with a Gaussian filter and deep slopes are slightly reduced by the method suggested in *Martinho and Batteen* [2006]. The meteorological forcing is taken from the German Weather Service forecasting models in 7 km resolution for the Western Baltic and 50 km resolution for the rest. The high spatial resolution of the meteorological forcing, especially the wind forcing in the area of the Danish Straits, showed to give realistic results for the Western Baltic sea in the study of *Burchard et al.* [2009]. As initial conditions, temperature and salinity fields are interpolated from a climatology. The open boundary is placed in the Kattegat (see figure 4.1) and is forced with climatological data for salinity and temperature and a linear interpolation of the measured gauges in Ringhals (east coast of the Kattegat) and Frederikshavn (west coast of the Kattegat) for the sea surface elevation.

The fixed grid simulations are carried out with equidistant heights for the vertical layers in each water column, known as sigma coordinates. For the adaptive grid simulation, a combination of zooming towards stratification, towards bottom and surface and horizontal filtering of interface positions and interface heights is used. A complete list of parameters used for the adaptation is listed in table 4.1. *Hofmeister et al.* [2010b] showed for idealised cases that the combination of zooming towards stratification and horizontal filtering allows already for a coordinate distribution, which can reduce the numerical mixing by zooming towards the vertical density gradients and aligning with the isopycnals. The isopycnal aligning worked out such that an additional isopycnal tendency was switched off here for a reduction of the computation effort. Also, zooming is applied in the lower 20m of the water column in order to keep some resolution close to the bottom although not required for the resolution of the vertical density gradients. The horizontal filter for the layer heights is most important for the regularity of the grid; an additional filter of vertical positions reduces additionally the layers' slope for the reduction of numerical errors. The grid adaptivity is adjusted to be slow in terms of fluctuations within a few hours as expected from the forcing fields or the onset of turbulence.

The main strategy here is to compare simulations of major inflows into the Baltic Sea with different vertical model grids in terms of verification and mixing. Some aspects of the major, cold inflow in 2003 are investigated for the higher resolution simulation with adaptive coordinates, since it is well resolving the processes associated with the inflow.

4.2 Verification and comparison of different model techniques

The verification concentrates on sea levels and salinities in the western and central Baltic Sea, since the focus of the present study is the hind-cast of the major inflows in 2003. It is essential for the study that the major, cold inflow in the first half of 2003 reaches the Gotland Basin in about the same time and intensity as observed.

α_{hor}	α_{lag}	α_{dif}	α_{iso}	c_{N^2}	c_{S^2}	c_d	d_{surf}	d_{min}	t_{grid}
0.2	0.0	0.3	0.0	0.2	0.0	0.3	20 m	0.2 m	6 h

Table 4.1: Parameters for the grid adaptation as defined in *Hofmeister et al.* [2010b] in the Baltic Sea simulations.

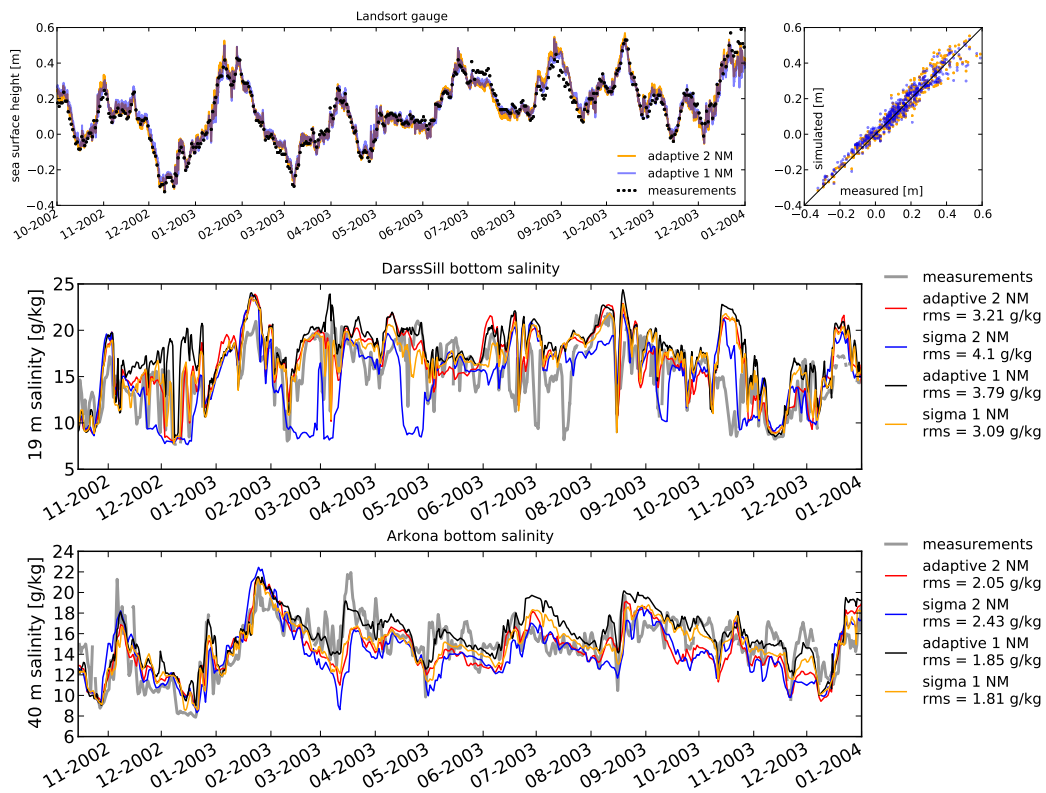


Figure 4.2: Time series of sea surface height in Landsort (top) and the bottom salinity at the Darss Sill (middle) and the Arkona station (bottom) for measurements and simulations with different vertical model grids, including the rms deviations between measurements and model results.

The gauge in Landsort as plotted in Fig. 4.2 for the simulations and measurements for the adaptive coordinates simulations, representative also for the barotropic mode of the fixed grid simulations, shows that the simulations are able to reproduce the filling state of the Baltic Sea. In the same figure, the near-bottom salinity time series are given for the Darss Sill and the Arkona station, both located in the western Baltic Sea. Although a horizontal resolution of 2 NM and even 1 NM is still not resolving all the bathymetric features in the Danish Straits, the time series show the major events of the measurements also in the simulation. Especially for the Darss Sill bottom salinity, the simulation with adaptive coordinates and 2 NM resolution is able to capture the salinity conditions western of the entrance to the Arkona Basin similarly as the simulation with fixed coordinates and a doubled horizontal resolution (see e.g. 15 Nov - 20 Dec 2002, and the months Feb-May 2003). The simulated bottom salinity in the Arkona Basin in the simulations are representing the stronger inflow events in November 2002, January and August 2003, which will propagate into the central Baltic Sea as known from the measurements reported by *Feistel et al.* [2004]. In March 2003, the bottom salinities are underestimated by all model simulations, which is probably a reaction of the simulated inflow-outflow characteristic to the applied forcing, such as mean river inflow and wind forcing in the still coarsely resolved Danish Straits. Also for the Arkona Station, the coarser resolution results for the adaptive coordinates are partially close to the higher resolution results with fixed coordinates (January to June 2003). The adaptive coordinates simulation in 1 NM horizontal resolution is generally overestimating the bottom salinity at the Darss Sill station for the same bathymetric setup of the Belt Sea as necessary for a realistic sigma coordinates simulation. Also at the Arkona station, there is the period from end of June to end of July 2003, and the second half of December 2003, where the higher resolution simulation overestimates the bottom salinity. Besides these periods increasing the rms difference to measurements, the events and variation in 2003 are reproduced in more detail than the fixed grid simulations. The results are suggesting that the bathymetry approximation in the model grid has to be done differently for different choices of terrain-following coordinate distributions.

In Fig. 4.3, time series of the vertical profile in the Gotland Deep are shown for the simulations and a few vertical profile measurements available in 2003 from monitoring measurements. The temporal interpolation of the measured profiles gives only an incomplete picture of the reality, nevertheless the major inflow in early 2003 is measured to arrive in March to May 2003. Measurements in July and October 2003 indicate that the salinity isolines are shifted further upward due to a following inflow activity from the filled Bornholm Basin and Gdansk Basin. The simulation results of the fixed grid simulations in the coarser horizontal resolution show an inflow in May 2003, but a downward shifted 12 g/kg isoline in the second half of 2003. The simulations using the adaptive grids in coarser horizontal resolution show an about 1 g/kg stronger inflow in May 2003 and the upward shifted salinity isolines due to inflow activity in the second half of 2003. In the higher resolution studies using the internal mixing parameterisation, the stratification obtained with the fixed grid is strongly diffused and does not show any clear inflow signal. In contrast to the fixed grid simulation, the adaptive grid simulation shows a stronger and therefore earlier inflow in March 2003. The results suggest that even with an internal mixing parameterisation, the horizontally higher resolved simulations with adaptive coordinates seem to lack entrainment of the inflows in the central Baltic Sea. A closer look onto the hydrography of the inflows (see section 4.3) will clarify that the inflows are better resolved in terms of the physical processes for the adaptive grids. As presented below in more detail, the reduced numerical mixing and pressure gradi-

ent errors result in an overall reduced mixing in the deep Baltic Sea. Although the adaptive grid results for the 2 NM horizontal resolution are quantitatively better, the 1 NM resolution simulation is open for an additional implementation of physically justified processes, which are not yet fully included into the model. Also a reduced bathymetry smoothing could result in a higher entrainment rate during the inflow into the central Baltic Sea. Still, in order to compare the different grid techniques, the same bathymetry is used for the fixed and adaptive grid simulations.

For a realistic, numerical representation of the physics during the Baltic inflow periods, the amount of uncertain and artificial contributions in the numerical model, such as internal pressure gradient errors or spurious mixing have to be reduced. *Hofmeister et al.* [2010b] showed for an idealised case that using a high-order pressure gradient scheme and using a vertical grid adaptation to the vertical density gradients, internal pressure gradient errors can be reduced substantially. In contrast to the internal pressure gradient errors, which cannot be estimated profoundly in a realistic simulation, the spurious mixing can be calculated exactly using the technique by *Burchard and Rennau* [2008]. The numerical mixing is calculated here as vertically integrated salinity variance decay due to the discretisation of the 3D-advection for an arbitrary vertical discretisation using N model layers in each position in the model domain. The model layer heights h_k , $k = 1, \dots, N$, are calculated as the distance between the vertical model layer interface positions z_{k-1} and z_k with

$$-H = z_0 < z_1 < \dots < z_{N-1} < z_N = \eta \quad (4.1)$$

covering the water column from mean depth H to the sea surface η such that the water depth

$$D = H + \eta = \sum_{k=1}^N h_k. \quad (4.2)$$

It should be noted here that for sigma coordinates, the layer heights h_k are constant over depth for a single water column, varying in time only with the water depth, whereas the layer heights for the adaptive coordinates are varying in time depending on the adaptation mechanism (see *Hofmeister et al.* [2010b] for details) even for constant water depths. The vertically integrated tracer variance decay due to numerical mixing, χ^{num} for a certain water column i at a certain time step number $n + 1$ writes as

$$\chi_{i,n+1}^{num} = \sum_{k=1}^N h_{i,k} \frac{A \left\{ \left(s_{i,k}^n \right)^2 \right\}_{i,k} - \left(A \left\{ s_{i,k}^n \right\}_{i,k} \right)^2}{\Delta t} = \frac{A \left\{ \left(s_{i,k}^n \right)^2 \right\}_{i,k} - \left(s_{i,k}^{n+1} \right)^2}{\Delta t}, \quad (4.3)$$

where s denotes a tracer concentration here, Δt is the time step used for the advection step and $A \{ \dots \}_{i,k}$ is the tracer concentration resulting from a pure 3D advection step. The tracer variance decay by physical mixing χ^{phys} is estimated by the decay term in the budget equation for the square of the mean tracer concentration s due to turbulent diffusion as described in *Burchard and Rennau* [2008]:

$$\chi^{phys} = \int_{-H}^{\eta} 2K_v (\partial_z s)^2 dz \quad (4.4)$$

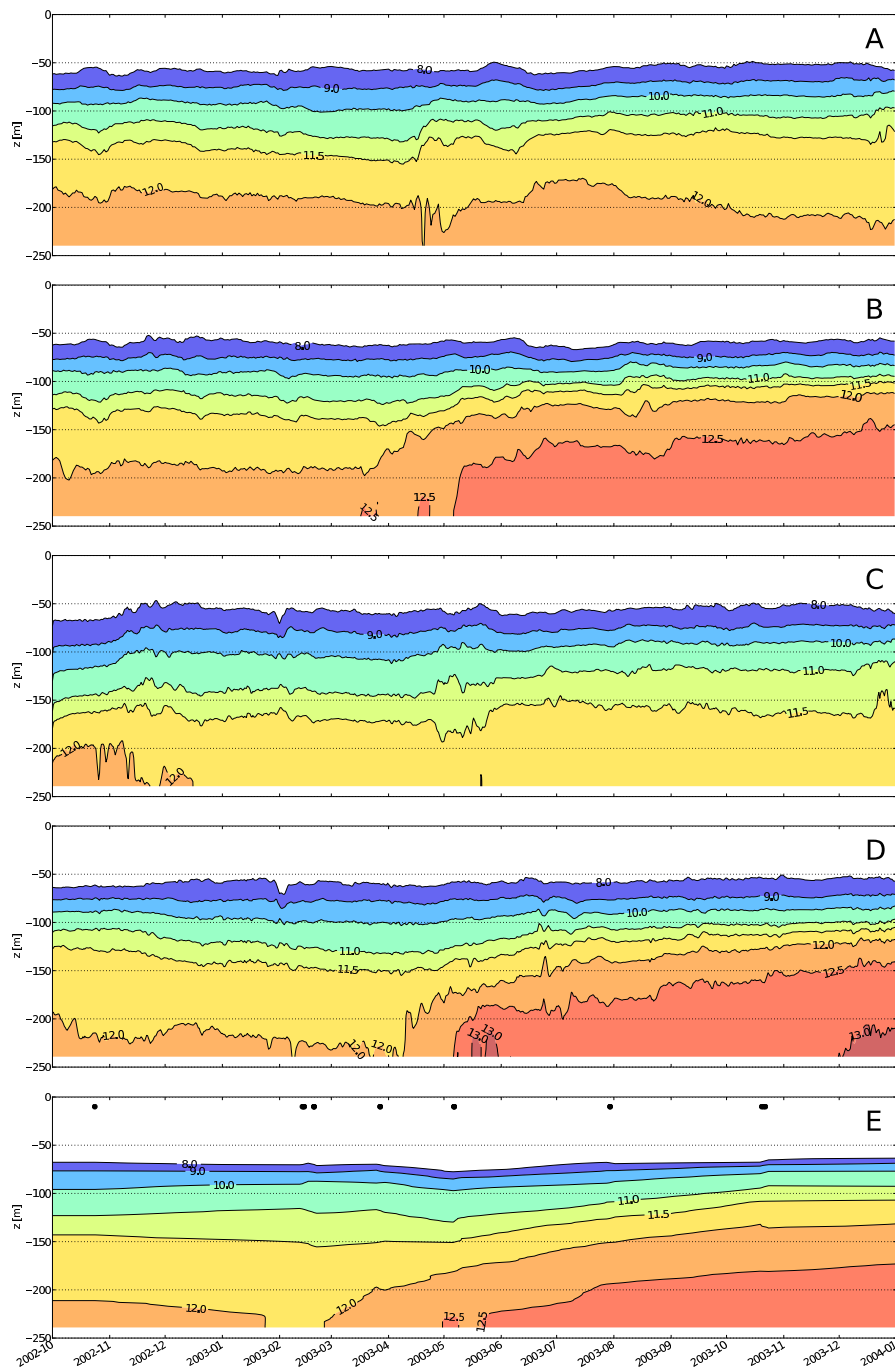


Figure 4.3: Time series of the vertical salinity profile at the station Gotland271 (see Fig. 4.1) for different simulations and measurements: A - sigma coordinates, 2 NM, B - adaptive coordinates, 2 NM, C - sigma coordinates, 1 NM, D - adaptive coordinates, 1 NM, E - measurements interpolated in time, the times of measurements are indicated by black dots.

where K_v is the vertical component of the turbulent diffusivity. The reduction of salinity variance due to horizontal diffusion is switched off in the model configuration since it is not necessary for the stability of the advection scheme. It has to be noted that by setting a horizontal background diffusivity, the horizontal salinity gradients would be reduced, which could account for a reduced numerical mixing.

The numerical mixing of salinity is shown in Fig. 4.4 in the same scaling as the physically induced, turbulent mixing in Fig. 4.5 for the 2 NM simulations and the 1 NM simulations including the internal mixing parameterisation. In Table 4.2, comparable numbers for all the simulations and tracer variance decays for temperature and salinity are listed. The values are calculated for the area east of longitude 16 °E representative for the part of the Baltic Sea, which is not covered by *Rennau and Burchard* [2009], who studied the tracer mixing for the Western Baltic Sea in detail. Additionally to the investigated higher-resolution simulations using the internal mixing parameterisation, earlier results without the internal mixing parameterisation are also listed in table 4.2. The values in table 4.2 show that the adaptive coordinates can reduce the numerical mixing by up to 30 %. The physical mixing for the coarser resolution is disturbed by localized, near-coast convective instabilities for yet unexplained mechanisms in the turbulence closure scheme. A possible explanation for the forcing of instabilities is the shear current due to pressure gradient errors, where the pycnoclines are close to the slopes.

The numerical salinity mixing for the central Baltic Sea is still stronger than the physically induced mixing, except for the higher resolution simulation with adaptive coordinates. Nevertheless, both values are closer to each other when using adaptive coordinates. The physical mixing of vertical gradients is found to be stronger when the numerical mixing is reduced due to the finer horizontal resolution in the simulations as well as using an additional parameterisation of physically-induced mixing. Similarly, a further reduced numerical mixing by an improved advection scheme would increase the potential for even stronger physical mixing. However, the results for mixing in the central Baltic Sea are mostly not representing physical processes. In general, the numerical mixing is strong in channelised bathymetry and along the steeper slopes due to up-welling, similar to the findings in *Rennau and Burchard* [2009] for the Arkona Sea. The simulations with adaptive coordinates show a reduced numerical mixing, and in terms of reducing the numerical temperature mixing, the usage of adaptive coordinates in the 2 NM horizontal resolution simulation is more effective than the increase in horizontal resolution in the fixed grid simulations. For reducing the numerical salinity mixing, the effect of doubled horizontal resolution is almost compensated by the usage of adaptive coordinates, but having a much lower computational cost. The physically induced salinity mixing shows that the western Baltic Sea up to the Gdansk Basin is the major mixing region. Especially the sills between the Arkona and Bornholm Basin as well as the sills east and west of Stolpe Furrow are the mixing hotspots. A significant amount of salinity mixing is also found in regions of river inflow along the coast. The turbulent mixing in the 2 NM sigma-coordinate simulation is strong at the steep slopes at the easterly and westerly side of the deep Gotland Basin, which can be explained by pressure gradient errors. Both, the usage of adaptive coordinates and the increase of horizontal resolution can effectively reduce the pressure gradient error induced mixing in these areas.

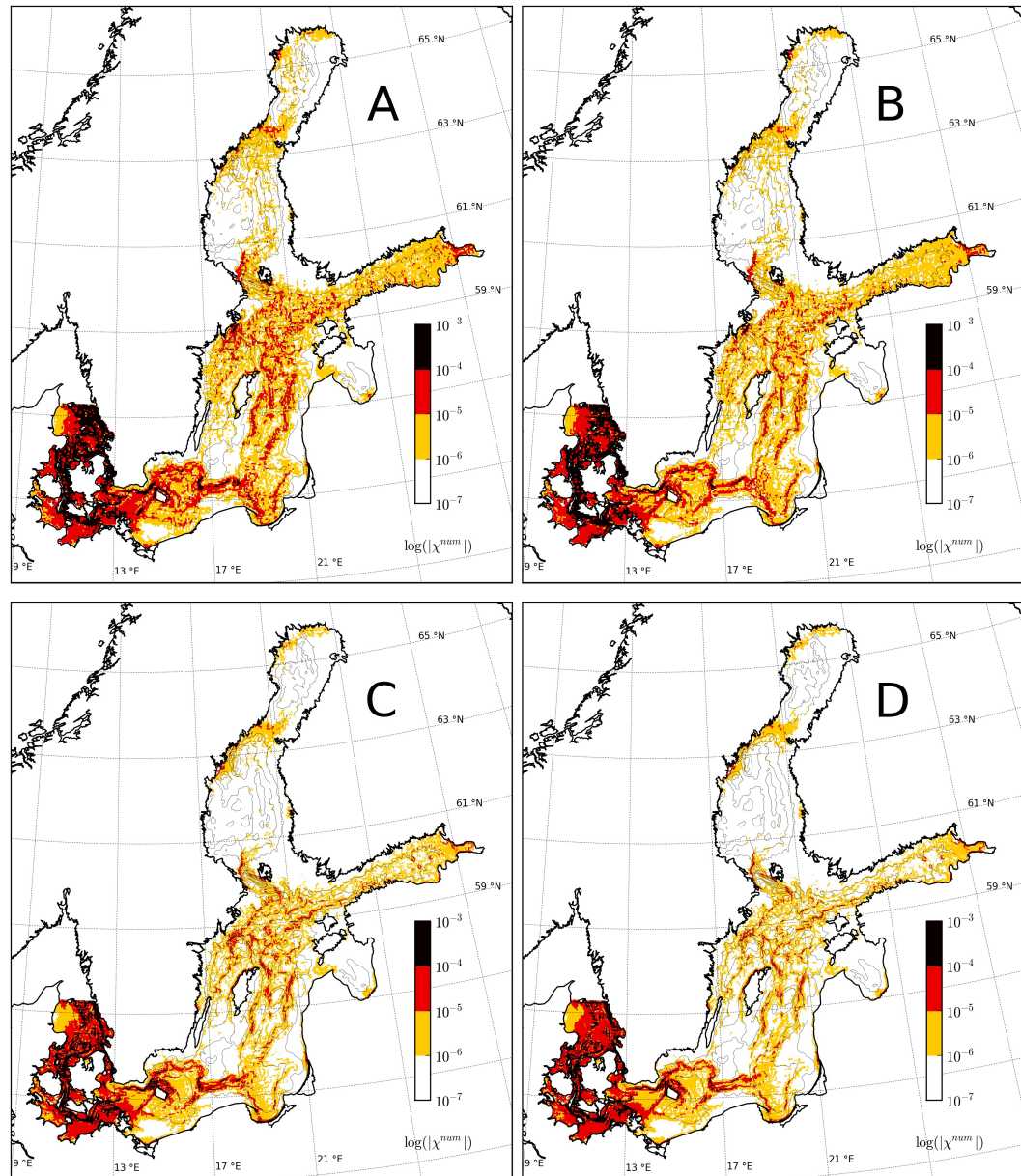


Figure 4.4: The numerical salinity variance decay shown on a log-scale of absolute values for the four different simulations: A - sigma coordinates, 2 NM, B - adaptive coordinates, 2 NM, C - sigma coordinates, 1 NM, D - adaptive coordinates, 1 NM. The internal mixing parameterisation is used for the higher-resolution simulations.

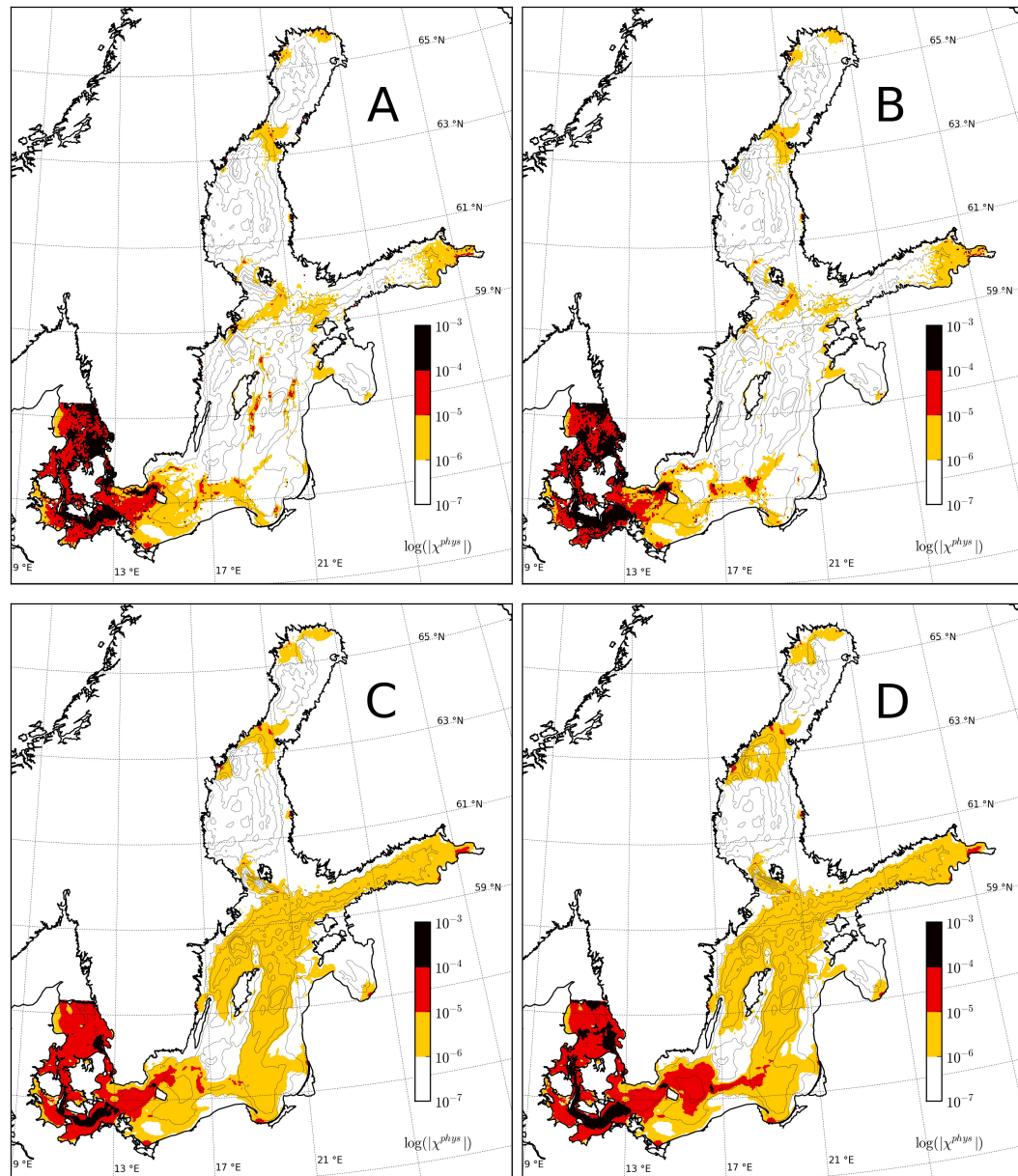


Figure 4.5: The physically induced salinity variance decay shown on a log-scale for the four different simulations: A - sigma coordinates, 2 NM, B - adaptive coordinates, 2 NM, C - sigma coordinates, 1 NM, D - adaptive coordinates, 1 NM. The internal mixing parameterisation is used for the higher-resolution simulations.

4.3 Spatial hydrography of the inflows as projected by the model

In *Piechura and Beszczynska-Möller* [2003], *Feistel et al.* [2003] and *Feistel et al.* [2004], detailed observations of the hydrography of the inflows in 2003 are given from measurements. In this section, we reproduce the lateral structure of these inflows in the Western and southern Baltic Sea by means of the higher-resolution (1 NM) adaptive grid model.

Piechura and Beszczynska-Möller [2003] presented a description of the hydrography of the inflows in 2003 based on vertical transects through the Bornholm Basin and the Stolpe Furrow. We chose snapshots for an evaluation of the simulation for transects B and C in Fig. 4.6: February 2003, at the end of the inflow period, August 2003, when the warm summer inflow is starting, and November 2003, after the summer inflow created a warm intermediate layer. *Piechura and Beszczynska-Möller* [2003] showed that in February 2003 cold, saline waters were entering the Bornholm Basin with maximum salinities of 21 psu. They also found a patchy temperature distribution in the deeper layers and concluded that mixing has happened locally in the Bornholm Basin. The model simulation (fig. 4.7) shows the cold, dense waters entering the Bornholm Basin. The model layers are zooming towards the stratification and allow to resolve the density field, which shows pinched and widened isopycnals as typical for an eddy circulation passing the basin.

In August 2003, the surface heating and mixing created a sharp thermocline as shown in *Feistel et al.* [2003] and *Piechura and Beszczynska-Möller* [2003] for the same dataset. The temperature is showing an almost four-layer structure with the 3-4 °C cold, dense water at the bottom, a patchy warmer layer with temperatures about 6-10 °C, possibly due to smaller inflow pulses in the first half of the year 2003. The measurements show that warm, dense water fills the bottom of the north-east Arkona Basin on the way into the Bornholm Basin. The adaptive coordinates are zooming to and aligning with the thermocline, which is defining the depth of the mixed layer.

Feistel et al. [2004] described that the warm inflow in summer 2003 was not as dense as the bottom waters in the Bornholm Basin from the inflow in January 2003, and therefore occupied the intermediate layer as seen also in Fig. 4.7 for the simulation.

For a completed picture of the three-dimensional hydrography, the bottom salinity and the mean transport below the halocline is shown in Fig. 4.8 and Fig. 4.9 for the simulation with adaptive coordinates and 1 NM horizontal resolution. Here, the halocline depth is the depth of the median of the vertical salinity profile. The major, cold inflow during the first half in 2003 spreads sub-sequentially through the Arkona Basin (January), Bornholm Basin (from February on), Gdansk Basin (March-April) and finally the Gotland Basin (May). When the bottom waters leave the Stolpe Furrow, it divides into a fraction, which moves into the Gdansk Basin and a fraction, which moves directly into the Gotland Basin. During April to June, the simulation shows that below the halocline, the transport is directed northward at the western and eastern slope of the Gotland Basin, whereas a counter current evolves in the deeper, southerly part of the Gotland Basin. In the channelised part of the inflow track such as the Bornholm Channel between the Arkona and Bornholm Basin, the Stolpe Furrow and the southern Gotland Basin, the dense bottom waters are slightly displaced from the main transport below the halocline. The reason is an asymmetric cross-channel density and velocity distribution, which is investigated in more detail in the next section.

	χ_S^{num} [10^{-6} g/kg m/s]	χ_T^{num} [10^{-5} °C m/s]	χ_S^{phys} [10^{-6} g/kg m/s]	χ_T^{phys} [10^{-5} °C m/s]
sigma 2 NM	3.63	3.97	(>100.)	(>100.)
adaptive 2 NM	2.59	2.29	(>100.)	(>100.)
sigma 1 NM *	2.22	2.48	1.41	3.37
adaptive 1 NM *	1.84	1.63	1.84	3.76
sigma 1 NM	2.64	3.04	0.69	2.01
adaptive 1 NM	2.18	2.02	1.1	2.53

Table 4.2: Numerical and physical mixing for salinity and temperature (indicated by subscript S or T) as the mean value of the watercolumn-wise integrated tracer variance decay for the area east of longitude 16 °E. The star (*) indicates the simulations with the parameterisation of internal mixing.

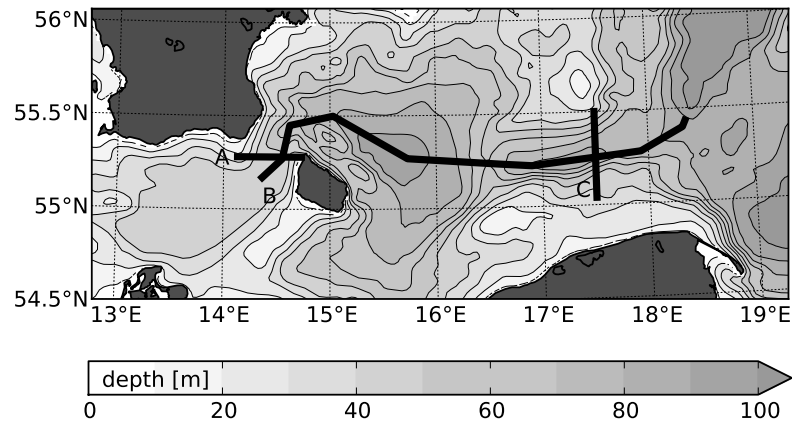


Figure 4.6: The different vertical transects A (Bornholms channel), B (inflow transect) and C (Stolpe Furrow cross-section) as plotted in the manuscript

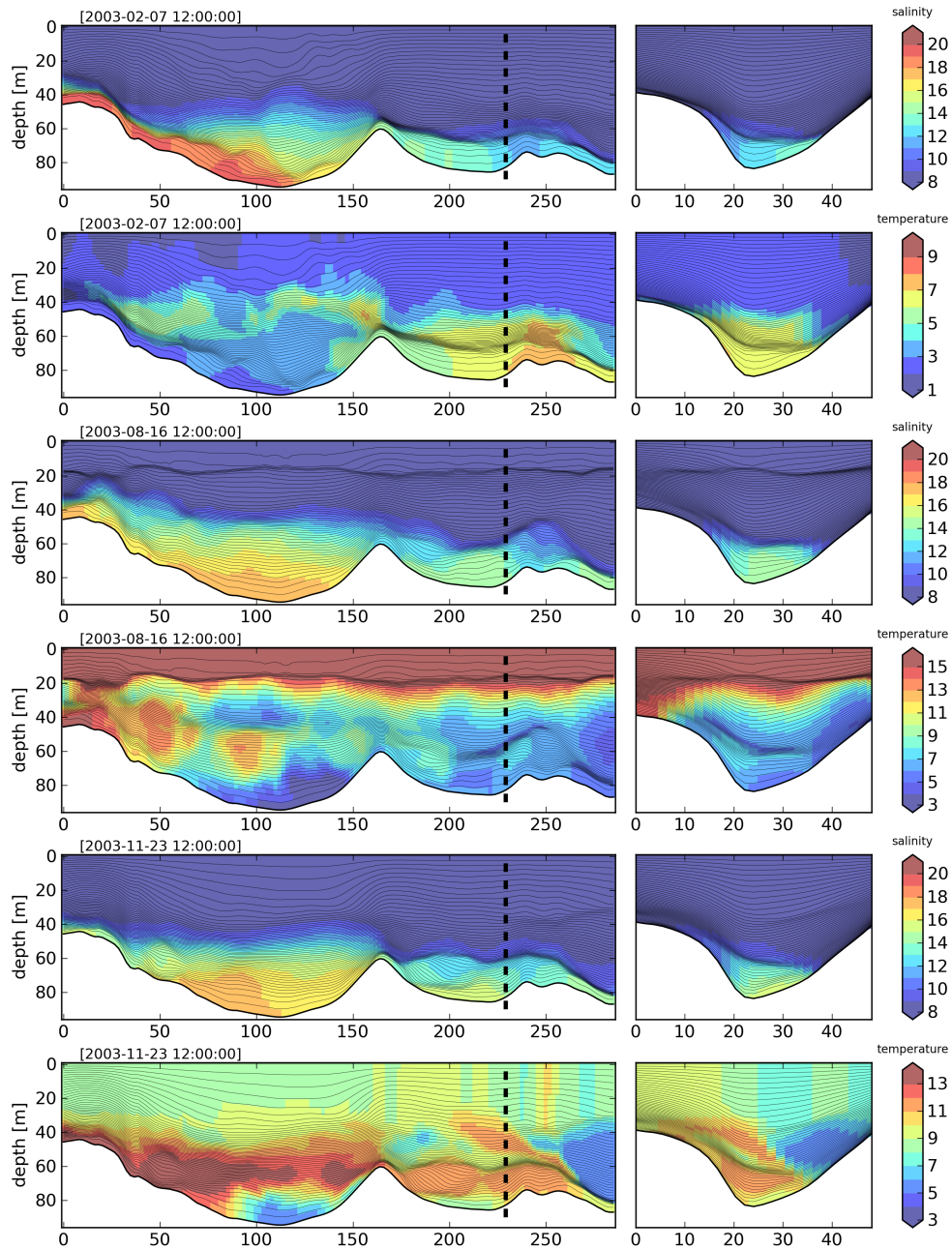


Figure 4.7: Salinity and temperature for the transects B and C (see Fig. 4.6) for February, August and November 2003

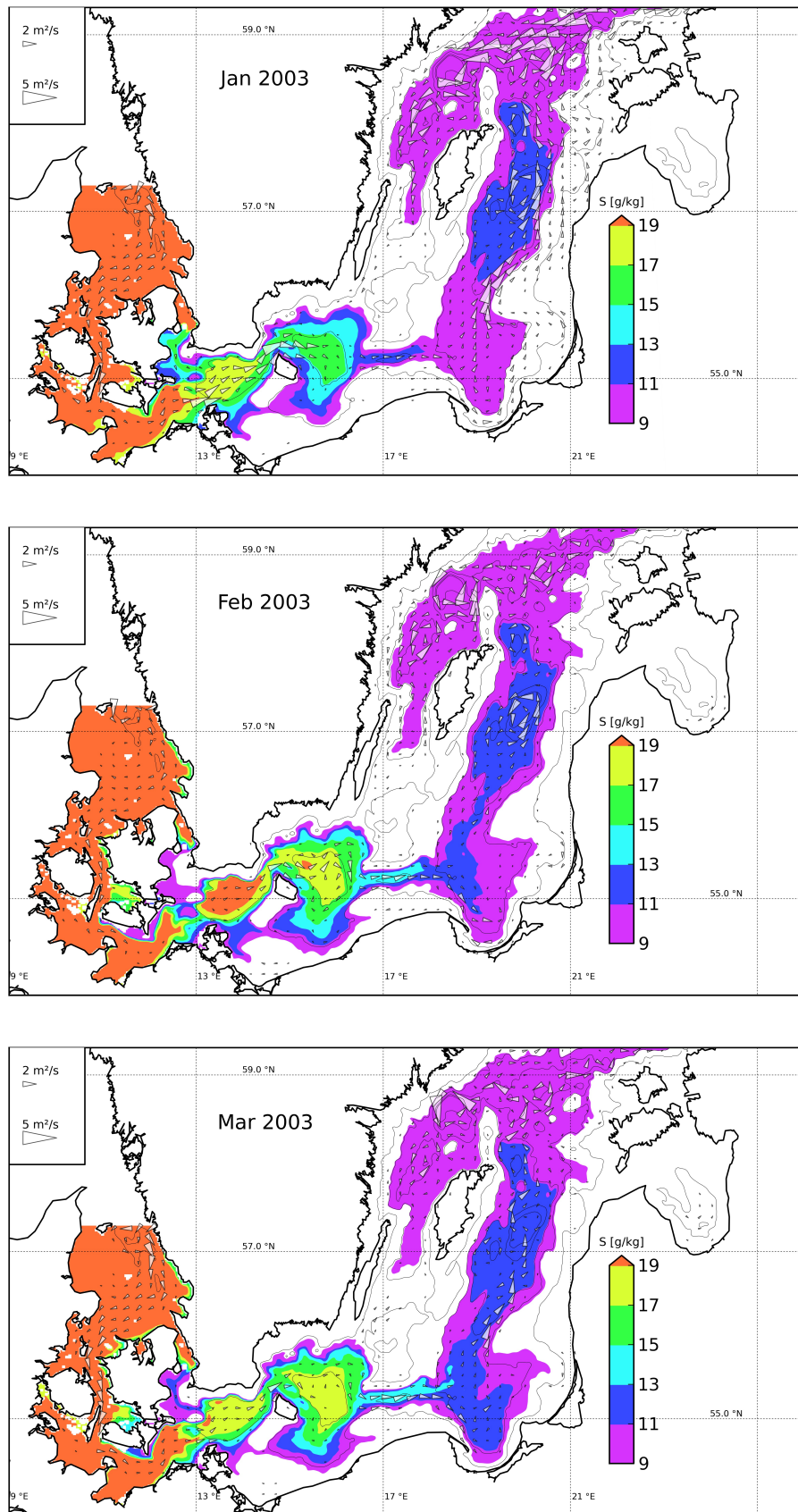


Figure 4.8: The simulated mean transport below the halocline (vectors), the simulated bottom salinity showed above 9 g/kg and the bathymetry contours for 40m, 80m, 120m, 170m and 200m for the months January to March 2003 (using the 1 NM simulation with adaptive coordinates and the internal mixing parameterisation)

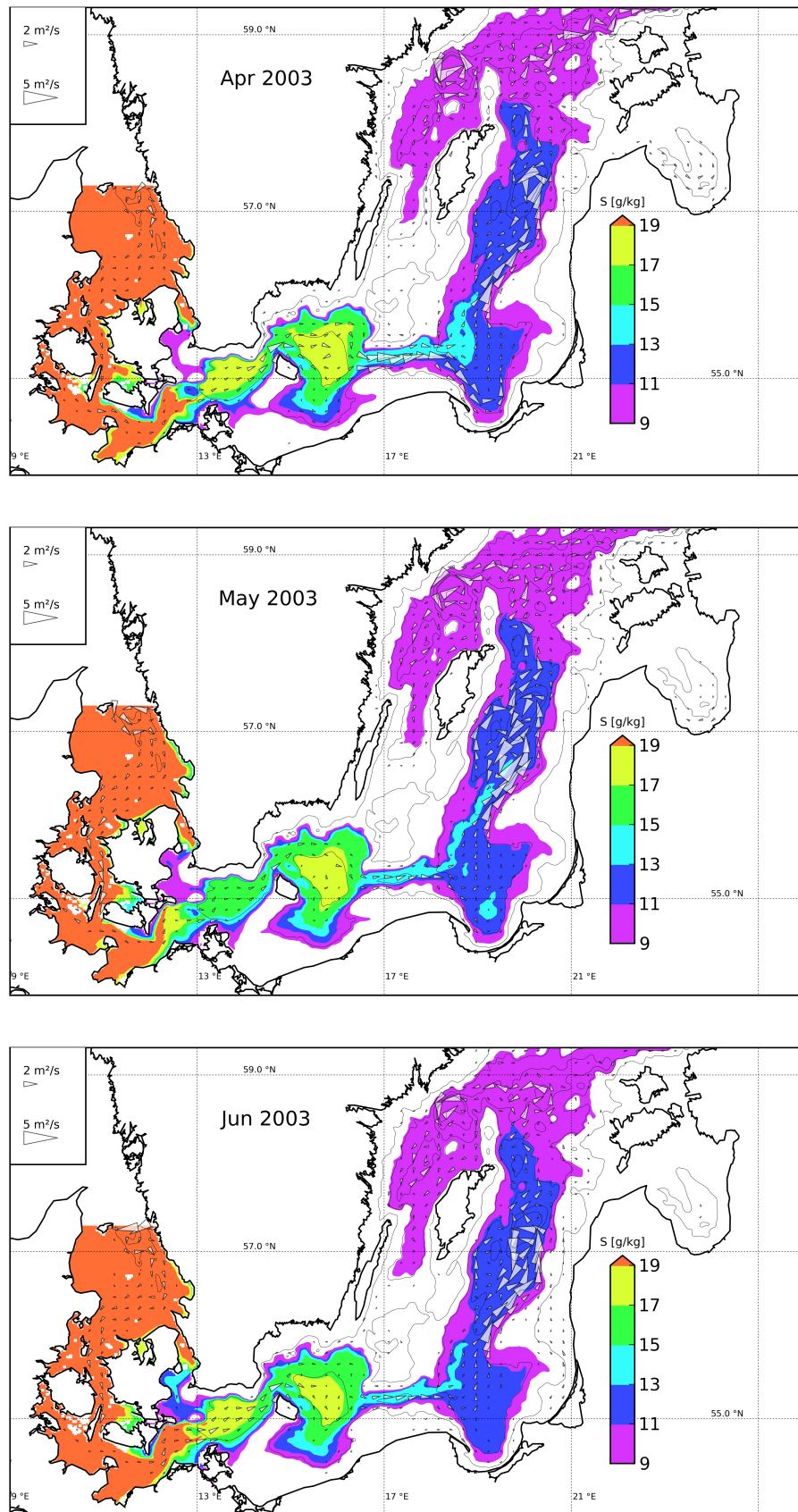


Figure 4.9: The simulated mean transport below the halocline (vectors), the simulated bottom salinity showed above 9 g/kg and the bathymetry contours for 40m, 80m, 120m, 170m and 200m for the months April to June 2003 (using the 1 NM simulation with adaptive coordinates and the internal mixing parameterisation)

4.4 Characteristic inflow dynamics in channelled bathymetry

Umlauf et al. [2007] presented measurements of the gravity current during inflow conditions in the Western Baltic Sea and found a characteristic cross-sectional shape and circulation, which is explained in *Umlauf and Arneborg* [2009a, b] by three-dimensional effects of earth rotation. In a high-resolution model study, *Umlauf et al.* [2010] showed that the vertical entrainment of ambient water into the gravity current is a vertical and laterally varying process. As shown in fig. 4.5 the Bornholm Channel between the Bornholm Basin and the Arkona Basin as well as the Stolpe Furrow are mixing hotspots in the southern Baltic Sea. Interestingly, these regions show a channelled bathymetry as studied in *Umlauf et al.* [2010]. Hence, in order to represent the realistic mixing in the channelised bathymetry, the cross-sectional hydrography has to be reproduced as realistic as possible. *Umlauf et al.* [2010] pointed out that mixing into the gravity current is suppressed at the lower side of the gravity current (referring to the depth of the density interface). Ambient water is mixed into the density interface and transported in a jet from the lower side to the upper side of the channel, where the mixing into the gravity currents takes place.

The cross-sectional hydrography is investigated here for the simulations with 1 NM horizontal resolution for the Bornholm Channel for January 2003, when the major, cold inflow passed in a steady state for a few inertial periods. Fig. 4.10 shows the along-channel and cross-channel velocity for the simulation with fixed sigma coordinates and adaptive coordinates. Both simulations are showing the same scenario with plume salinities of more than 20 g/kg, along channel velocities of more than 0.5 ms^{-1} and a cross-channel jet with speeds of about 0.3 ms^{-1} . The salinity interface sharpens at the down-welling side of the channel for both simulations, but the effect is limited for the sigma coordinate simulation to the places, where the isolines of density are coincide with the coordinate alignment, roughly given by the channels shape. The adaptive coordinate simulation shows a much stronger isohaline pinching and a thinner interface jet, well aligned with the isohalines. In Fig. 4.7, a similar pinching of isolines is found in the Stolpe Furrow cross-section. Especially at about 14.5°E in Fig. 4.10, the cross-sectional transport in the sigma coordinates simulation is basically aligned with the coordinates, the isohalines spread out due to mixing, which also results in a weaker core of the plume.

The weaker core of the plume and the even further displacement of the dense core of the gravity current from the strongest along-channel velocities for the sigma-coordinates are reasons for the weaker inflows in the fixed coordinate simulations as presented in section 4.2.

In Figure 4.2, the salinity in the Arkona Basin is similar for all the simulations for the period of 6 January to 15 February. The salt transport during that period of 40 days through the cross-section in figure 4.10 below the inflow's interface (taken here as the 9.5 g/kg salinity isoline) gives for the adaptive coordinates simulation 2811 Mt and for the sigma coordinates simulation 2327 Mt. Hence, the adaptive coordinates simulation allows for an almost 21 % higher amount of salt transport simply by the numerical representation of the channel flow.

4.5 Conclusions on the Baltic Sea modelling

The realistic model study of the Baltic inflows in 2003 shows that the adaptive vertical discretisation with its horizontal filters results in an improved representation of the vertical mixing and horizontal transport processes. This is essential for physically realistic modelling of diapycnal mixing.

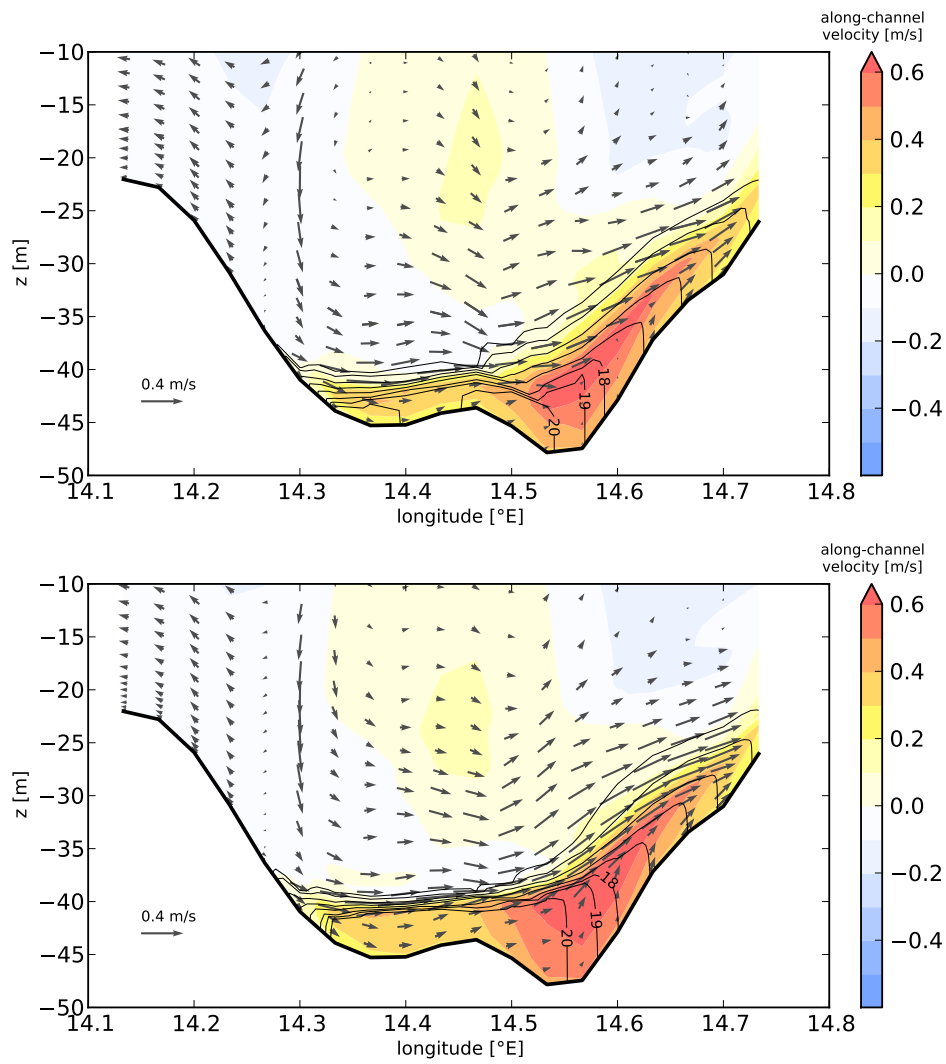


Figure 4.10: Cross-channel velocities (arrows), along-channel velocities (colours) and salinity contours for 2003-01-31 from the simulations using the 1 NM simulation and the internal mixing parameterisation. The upper panel shows the simulation with sigma-coordinates, the lower panels shows the simulation with adaptive coordinates. The unlabelled contours are continued in 2 g/kg steps below salinities of 18 g/kg.

The results confirm the work of *Hofmeister et al.* [2010b], who found for idealised experiments that discretisation errors can be reduced significantly with the adaptive grids. In terms of numerical mixing, the application of adaptive coordinates almost compensates the effect of doubling the horizontal resolution for fixed grids, however at relatively low computational cost.

The model results show that the hotspots of mixing in the Baltic Sea are the straits and the channels in the southern Baltic Sea in addition to the highly active Western Baltic Sea. The resolution of the gravity currents in channelled bathymetry by the adaptive grid model has a significant effect on the simulated deep water renewal in the central Baltic Sea.

Although the discretisation errors are reduced effectively by the adaptive coordinates, the numerical mixing is still a major contributor to the effective tracer mixing in a Baltic Sea model. Refined physical mixing parametrisations will improve the model results only, if the numerical mixing is effectively reduced.

The model performance can be further enhanced for the adaptive grids, if the 3D advection scheme is improved in terms of reduced numerical mixing. Additionally, a technique allowing for drying of bottom layers in the adaptive grid would decrease the steepness of the layer slopes with the potential to further reduce pressure gradient errors in the adaptive grid.

5 Summary and conclusions

In the present thesis, the strengths and weaknesses of numerical modelling of stratified coastal seas are evaluated in detail. Therefore two different marine systems were studied exemplarily – a shallow estuary, which is stratified and de-stratified several times throughout a year and the deeper, permanently stratified Baltic Sea. Both systems show dense inflows along the bottom, which are important for the physical regime in the systems. Hence, the approach of the above studies is to use a state-of-the-art numerical model, which resolves the along-bottom flow with bottom-following coordinates.

The strengths of numerical modelling of stratified seas is obviously the possibility for a detailed, complete analysis of the acting physical processes. These processes are in the best case well resolved in time and the three spacial dimensions by the discretisation and implementation of the primitive equations.

In order to study the generation and destruction of stratification in shallow seas, a diagnostic method for analysing the relevant processes was developed in the framework of the thesis. Measurements usually cannot provide all the necessary data for evaluating the contributing processes of stratification. For the shallow estuary example, the Limfjord, the high-resolution study made it possible to identify the major processes determining stratification from the simulation results. The processes of differential advection are major contributions in the realistic example. Also, the application of the analysis in idealised experiments lead to the insight that different processes act together in the stratification process. This confirms that only a good resolution of the vertical and horizontal gradients of density and velocities in the water column allows to reproduce the ongoing stratifying processes in a numerical model.

With the newly developed diagnostics for the stratifying processes, empirical estimates and simple numerical models can be theoretically verified. Also unresolved or ignored contributions to the stratification can be estimated since the dynamic equation for potential energy anomaly, derived here, provides a complete budget. The realistic, high-resolution model study of the Limfjord shows that physical processes can be analysed successfully with a numerical model.

The simulation of larger, deeper and permanently stratified coastal seas is shown to be subject to discretisation errors in model resolutions, which are manageable with today's computers. In the present thesis, the Baltic Sea is the study subject, since its basins are largely affected by processes at the sloping sea bed towards the coast. The findings can be generalised also for other coastal seas with permanent stratification, such as the Black Sea. The aim of the studies on numerical techniques is to investigate and improve the representation of the physical processes by the model discretisation. Large discretisation errors (such as numerical mixing and internal pressure gradient errors) occur even in higher resolutions, although tracer budgets for e.g. the Baltic Sea could be reproduced realistically in previous studies.

In the thesis, the mixing effect of internal pressure gradient errors is evaluated to be a significant source of uncertainties in numerical models of coastal stratified seas. Pressure gradient errors are artificially eroding the permanent stratification in models using bottom-following coordinates, next to inducing a significant artificial circulation. It has been shown

here that improved numerical model techniques, such as improved internal pressure gradient schemes and adaptive vertical coordinates, reduce pressure gradient errors effectively. A major outcome of the thesis is the development of adaptive vertical coordinates for realistic, three-dimensional numerical ocean models. The advantages of the grid adaptation are presented for idealised studies as well as for a realistic hindcast study in the Baltic Sea. With a relatively small overhead in computation time of a numerical model using adaptive coordinates in the vertical, discretisation errors can be reduced as effective as increasing the horizontal resolution of a fixed grid model. However, the former is far more efficient in terms of computational effort. Additionally, the optimised representation of the physical regime by the adaptive coordinates allows for a convergence of discretisation-sensitive techniques as the pressure gradient calculation towards the expected solution.

For future applications of the presented numerical techniques, it can be recommended to further improve the numerics of advection in numerical models. Even the presented adaptive grid discretisation will benefit from improved advection schemes in terms of further reducing the discretisation errors. It has been shown that mixing in a numerical model is highly affected by discretisation errors of the advection terms. Improved mixing schemes will not necessarily improve the effective mixing, including the physically-motivated and numerical mixing, in the model. The presented numerical techniques increase the performance of a numerical model in coastal stratified seas, which allows for studying further improved mixing schemes. In the realistic hindcast study in the Baltic Sea, the reduced numerical mixing revealed the lack of unparametrised mixing processes in the model. Hence, further research on the parametrisation of internal wave mixing, double-diffusive mixing or eddy mixing in numerical models is necessary for a better physical performance of numerical models in coastal stratified seas.

Bibliography

- Ackermann, J., M. Loewen, and P. Hamblin, Benthic-Pelagic coupling over a zebra mussel reef in western Lake Erie, *Limnology and Oceanography*, 46(4), 892–904, 2001.
- Adcroft, A., and R. Hallberg, On methods for solving the oceanic equations of motion in generalized vertical coordinates, *Ocean Modelling*, 11, 224–233, 2006.
- Arakawa, A., and V. R. Lamb, Computational design of the basic dynamical processes of the UCLA General Circulation Model, *Meth. Comput. Phys.*, pp. 173–263, 1977.
- Arneborg, L., V. Fiekas, L. Umlauf, and H. Burchard, Gravity current dynamics and entrainment - a process study based on observations in the Arkona Basin, *J. Phys. Oceanogr.*, 37, 2094–2113, 2007.
- Auclair, F., P. Marsaleix, and C. Estournel, Sigma coordinate pressure gradient errors: evaluation and reduction by an inverse method, *Journal of Atmospheric and Oceanic Technology*, 17, 1348–1367, 2000.
- Axell, L., On the variability of Baltic Sea deepwater mixing, *J. Geophys. Res.*, 103, 21,667–21,682, 1998.
- Beckers, J.-M., H. Burchard, E. Deleersnijder, and P.-P. Mathieu, On the numerical discretisation of rotated diffusion operators in ocean models, *Monthly Weather Review*, 128, 2711–2733, 2000.
- Beckmann, A., and R. Döscher, A method for improved representation of dense water spreading over topography in geopotential-coordinate models, *J. Phys. Oceanogr.*, 27, 581–591, 1997.
- Beckmann, A., and D. B. Haidvogel, Numerical simulation of flow around a tall isolated seamount. Part I: Problem formulation and model accuracy, *J. Phys. Oceanogr.*, 23, 1736–1753, 1993.
- Behrens, J., K. Dethloff, W. Hiller, and A. Rinke, Evolution of small-scale filaments in an adaptive advection model for idealized tracer transport, *Monthly Weather Review*, 128, 2976–2982, 2000.
- Blayo, E., and L. Debreu, Adaptive mesh refinement for finite-difference ocean models: First experiments, *J. Phys. Oceanogr.*, 29, 1239–1250, 1999.
- Bleck, R., An oceanic general circulation model framed in hybrid isopycnic-cartesian coordinates, *Ocean Modelling*, 4, 55–88, 2002.
- Bleck, R., and L. T. Smith, A wind-driven isopycnic coordinate model of the North and Equatorial Atlantic Ocean. 1. Model development and supporting experiments, *J. Geophys. Res.*, 95, 3273–3285, 1990.

- Blumberg, A. F., and G. L. Mellor, A description of a coastal ocean circulation model, in *Three dimensional ocean models*, edited by N. S. Heaps, pp. 1–16, American Geophysical Union, Washington, D.C., 1987.
- Bowden, K. F., Turbulent mixing in estuaries, *Ocean Management*, 6, 117–135, 1981.
- Bowden, K. F., and L. A. Fairbairn, A determination of the frictional forces in a tidal current, *Proc. Trans. R. Soc. Lond. A*, 214, 371–392, 1952.
- Bryan, K., A numerical model for the study of the world ocean, *J. Computat. Phys.*, 4, 347–376, 1969.
- Burchard, H., Recalculation of surface slopes as forcing for numerical water column models of tidal flow, *App. Math. Modelling*, 23, 737–755, 1999.
- Burchard, H., and J.-M. Beckers, Non-uniform adaptive vertical grids in one-dimensional numerical ocean models, *Ocean Modelling*, 6, 51–81, 2004.
- Burchard, H., and K. Bolding, GETM - a general estuarine transport model. Scientific documentation, *Tech. Rep. EUR 20253 EN*, European Commission, 2002.
- Burchard, H., and R. Hofmeister, A dynamic equation for the potential energy anomaly for analysing mixing and stratification in estuaries and coastal seas, *Estuarine, Coastal and Shelf Science*, 77, 679–687, 2008.
- Burchard, H., and O. Petersen, Hybridisation between σ and z coordinates for improving the internal pressure gradient calculation in marine models with steep bottom slopes, *Int. J. Numer. Meth. Fluids*, 25, 1003–1023, 1997.
- Burchard, H., and H. Rennau, Comparative quantification of physically and numerically induced mixing in ocean models, *Ocean Modelling*, 20, 293–311, 2008.
- Burchard, H., K. Bolding, T. P. Rippeth, A. Stips, J. H. Simpson, and J. Sündermann, Microstructure of turbulence in the Northern North Sea: A comparative study of observations and model simulations, *J. Sea Res.*, 47, 223–238, 2002.
- Burchard, H., K. Bolding, and M. R. Villarreal, Three-dimensional modelling of estuarine turbidity maxima in a tidal estuary, *Ocean Dynamics*, 54, 250–265, 2004.
- Burchard, H., K. Bolding, W. Kühn, A. Meister, T. Neumann, and L. Umlauf, Description of a flexible and extendable physical-biogeochemical model system for the water column, *J. Mar. Sys.*, 61, 180–211, 2006.
- Burchard, H., G. Flöser, J. V. Staneva, R. Riethmüller, and T. Badewien, Impact of density gradients on net sediment transport into the Wadden Sea, *J. Phys. Oceanogr.*, 38, 566–587, 2008.
- Burchard, H., F. Janssen, K. Bolding, L. Umlauf, and H. Rennau, Model simulations of dense bottom currents in the Western Baltic Sea, *Cont. Shelf Res.*, 29, 205–220, 2009.
- Chassignet, E. P., et al., Generalized vertical coordinates for eddy-resolving global and coastal ocean forecasts, *Oceanography*, 19, 20–31, 2006.

- Cheng, Y., V. M. Canuto, and A. M. Howard, An improved model for the turbulent PBL, *Journal of Atmospheric Sciences*, 59, 1550–1565, 2002.
- Chu, P. C., and C. Fan, Hydrostatic correction for reducing horizontal pressure gradient errors in sigma coordinate models, *J. Geophys. Res.*, 108, 3206, doi: 10.1029/2002JC001,668, 2003.
- Cloern, J. E., Turbidity as a control on phytoplankton biomass and productivity in estuaries, *Cont. Shelf Res.*, 7, 1367–1381, 1987.
- de Boer, G. J., J. D. Pietrzak, and J. C. Winterwerp, Using the potential energy anomaly equation to investigate the roles of tidal straining and advection in river plumes, *Ocean Modelling*, 22, 1–11, 2008.
- Deleersnijder, E., and K. G. Ruddick, A generalized vertical coordinate for 3D marine problems, *Bulletin de la Société Royale des Sciences de Liège*, 61, 489–502, 1992.
- Dewar, W., and T. McDougall, The numerical solution of the one-dimensional advection-diffusion equation in layered coordinates, *Monthly Weather Review*, 128, 2575–2587, 2000.
- Ezer, T., Entrainment, diapycnal mixing and transport in three-dimensional bottom gravity current simulations using the Mellor-Yamada turbulence scheme, *Ocean Modelling*, 9, 151–168, 2005.
- Fallesen, G., F. Andersen, and B. Larsen, Life, death and the revival of the hypertrophic Mariager Fjord, *J. Mar. Sys.*, 25, 313–321, 2000.
- Feistel, R., G. Nausch, W. Matthäus, and E. Hagen, Temporal and spatial evolution of the Baltic deep water renewal in spring 2003, *Oceanologia*, 45, 623–642, 2003.
- Feistel, R., G. Nausch, T. Heene, J. Piechura, and E. Hagen, Evidence for a warm water inflow into the Baltic Proper in summer 2003, *Oceanologia*, 46, 581–598, 2004.
- Feistel, R., G. Nausch, and E. Hagen, Unusual Baltic inflow activity 2002/3 and varying deep-water properties, *Oceanologia*, 48, 21–35, 2006.
- Fennel, W., T. Seifert, and B. Kayser, Rossby radii and phase speeds in the Baltic Sea, *Cont. Shelf Res.*, 11, 23–36, 1991.
- Fiedler, B., Grid adaptation and its effect on entrainment in an E-I model of the atmospheric boundary layer, *Monthly Weather Review*, 130, 733–740, 2002.
- Fischer, H. B., E. J. List, R. C. Y. Koh, J. Imberger, and N. H. Brooks, *Mixing in Inland and Coastal Waters*, Academic Press, New York, 1979.
- Frechette, M., and E. Bourget, Food limited growth of *Mytilus edulis L.* in relation to the benthic boundary layer, *Canadian Journal of Fisheries and Aquatic Sciences*, 42(6), 1166–1170, 1985.
- Gale, E., C. Pattiaratchi, and R. Ranasinghe, Vertical mixing processes in Intermittently Closed and Open Lakes and Lagoons, and the dissolved oxygen response, *Estuarine, Coastal and Shelf Sci.*, 69, 205–216, 2006.
- Galperin, B., L. H. Kantha, S. Hassid, and A. Rosati, A quasi-equilibrium turbulent energy model for geophysical flows, *Journal of Atmospheric Sciences*, 45, 55–62, 1988.

- Gent, P. R., and J. C. McWilliams, Isopycnal mixing in ocean circulation models, *J. Phys. Oceanogr.*, 20, 150–155, 1990.
- Golenko, N., V. Paka, M. Golenko, and A. Korzh, Meso-scale water structure in the southern Baltic in the summer of 2006, *J. Mar. Sys.*, 74, S13–S19, 2008.
- GOTM, General Ocean Turbulence Model, <http://www.gotm.net>, 2005.
- Griffies, S. M., R. C. Pacanowski, M. Schmidt, and V. Balaji, Tracer Conservation with an Explicit Free Surface Method for z-Coordinate Ocean Models, *Monthly Weather Review*, 129, 1081–1098, 2001.
- Hagen, E., and R. Feistel, Observations of low-frequency current fluctuations in deep water of the Eastern Gotland Basin / Baltic Sea, *J. Geophys. Res.*, 109, 1–15, 2004.
- Halliwell, G. R., Evaluation of vertical coordinate and vertical mixing algorithms in the HYbrid-Coordinate Ocean Model (HYCOM), *Ocean Modelling*, 7, 285–322, 2004.
- Haney, R. L., On the Pressure Gradient Force over Steep Topography in Sigma Coordinate Ocean Models, *J. Phys. Oceanogr.*, 21, 610–619, 1991.
- Hofmeister, R., Model studies on stratification in the Limfjord, *Diplom-thesis*, Institute of Physics, University of Rostock, 2006, 74pp.
- Hofmeister, R., H. Burchard, and K. Bolding, Realistic modelling of stratification in the Limfjord, *Cont. Shelf Res.*, 29, 1515–1524, 2009.
- Hofmeister, R., J.-M. Beckers, and H. Burchard, Realistic modelling of the major inflows into the central baltic sea in 2003 using terrain-following coordinates, *Ocean Modelling*, 2010a, submitted.
- Hofmeister, R., H. Burchard, and J.-M. Beckers, Non-uniform adaptive vertical grids for 3D numerical ocean models, *Ocean Modelling*, 33, 70–86, 2010b.
- Holt, J., and I. James, An s coordinate density evolving model of the Northwest European Continental Shelf - 1, model description and density structure, *J. Geophys. Res.*, 106, 14,015–14,034, 2001.
- Ilicak, M., T. M. Özgökmen, H. Peters, H. Baumert, and M. Iskandarani, Performance fo two-equation turbulence closures in three-dimensional simulations of the Red Sea overflow, *Ocean Modelling*, 24, 122–139, 2008.
- Iselin, J., J. Prusa, and W. Gutowski, Dynamic grid adaptation using the MPDATA scheme, *Monthly Weather Review*, 130, 1026–1039, 2002.
- Jackett, D. R., T. J. McDougall, R. Feistel, D. G. Wright, and S. M. Griffies, Algorithms for density, potential temperature, conservative temperature and the freezing temperature of seawater, *Journal of Atmospheric and Oceanic Technology*, 23, 1709–1728, 2006.
- Jay, D. A., and J. D. Musiak, Particle trapping in estuarine tidal flows, *J. Geophys. Res.*, 99, 445–461, 1994.
- Kasahara, A., Various vertical coordinate systems used for numerical weather predictions, *Monthly Weather Review*, 102, 509–522, 1974.

- Kondo, J., Air-sea bulk transfer coefficients in diabatic conditions, *Bound. Layer Meteor.*, 9, 91–112, 1975.
- Kremp, C., T. Seifert, V. Mohrholz, and W. Fennel, The oxygen dynamics during the Baltic inflow events in 2001 to 2003 and the effect of different meteorological forcing - A model study, *J. Mar. Sys.*, 67, 13–30, 2007.
- Lander, J. W. M., P. A. Blokland, and J. M. de Kok, The three-dimensional shallow water model TRIWAQ with a flexible vertical grid definition, *Tech. Rep. RIKZ/OS-96.104x, SIMONA report 96-01*, National Institute for Coastal and Marine Management / RIKZ, The Hague, The Netherlands, 1994.
- Lass, H. U., H. Prantke, and B. Liljebladh, Dissipation in the Baltic proper during winter stratification, *J. Geophys. Res.*, 108, 3187, 2003.
- LeBlond, P. H., and L. Mysak, *Waves in the ocean*, Elsevier, New York, 1978, 602 pp.
- Lehmann, A., and H.-H. Hinrichsen, On the thermohaline variability of the Baltic Sea, *J. Mar. Sys.*, 25, 333–357, 2000.
- Lehmann, A., P. Lorenz, and D. Jacob, Modelling the exceptional Baltic Sea inflow events in 2002-2003, *Geophys. Res. Letters*, 31, doi:10.1029/2004GL020,830, 2004.
- Liseikin, V., *Grid generation methods*, Springer, Berlin-Heidelberg, 1999.
- Madec, G., P. Delecluse, M. Imbard, and C. Levy, Opa 8.1 ocean general circulation model reference manual, vol. 11, pp. 1–91, 1998.
- Marchesiello, P., L. Debreu, and X. Couvelard, Spurious diapycnal mixing in terrain-following coordinate models: The problem and a solution, *Ocean Modelling*, 26, 156–169, 2009.
- Martinho, A. S., and M. L. Batteen, On Reducing the Slope Parameter in Terrain-Following Numerical Ocean Models, *Ocean Modelling*, 13, 166–175, 2006.
- Matthäus, W., Mixing across the primary Baltic halocline, *Beitr. Meeresk.*, 61, 21–31, 1990.
- Matthäus, W., and H. Frank, Characteristics of major Baltic inflows – a statistical analysis, *Cont. Shelf Res.*, 12, 1375–1400, 1992.
- Meier, H. E. M., Modeling the pathways and ages of inflowing salt- and freshwater in the Baltic Sea, *Estuarine, Coastal and Shelf Sci.*, 74, 610–627, 2007.
- Meier, H. E. M., R. Döscher, B. Broman, and J. Piechura, The major Baltic inflow in January 2003 and preconditioning by smaller inflows in summer/autumn 2002: a model study, *Oceanologia*, 46 (4), 557–579, 2004.
- Mellor, G., and A. Blumberg, Modeling vertical and horizontal diffusivities with the sigma coordinate system, *Monthly Weather Review*, 113, 1379–1383, 1985.
- Mellor, G. L., T. Ezer, and L.-Y. Oey, The pressure gradient conundrum of sigma coordinate ocean models, *Journal of Atmospheric and Oceanic Technology*, 11, 1126–1134, 1994.
- Mellor, G. L., L.-Y. Oey, and T. Ezer, Sigma coordinate pressure gradient errors and the seamount problem, *Journal of Atmospheric and Oceanic Technology*, 15, 1122–1131, 1998.

- Mortimer, C. H., The oxygen content of air-saturated fresh waters over ranges of temperature and atmospheric pressure of limnological interest., *Mitt. Internat. Verein. Limnol.*, 22, 1–23, 1981.
- Muschenheim, D. K., and C. R. Newell, Utilization of seston flux over a mussel bed., *Marine Ecology Progress Series*, 85, 131–136, 1992.
- Nunes Vaz, R. A., G. W. Lennon, and J. R. de Silva Samarasinghe, The negative role of turbulence in estuarine mass transport, *Estuarine, Coastal and Shelf Sci.*, 28, 361–377, 1989.
- Officer, C. B., *Physical Oceanography of Estuaries*, Wiley, New York, 1976.
- Osborn, T. R., Estimates of the local rate of vertical diffusion from dissipation measurements, *J. Phys. Oceanogr.*, 10, 83–89, 1980.
- Paka, V. T., V. M. Zhurbas, N. N. Golenko, and L. A. Stefantsev, Effects of the Ekman Transport on the Overflow of Saline Waters through the Slupsk Furrow in the Baltic Sea, *Izvestiya, Atmospheric and Ocean Physics*, 34, 641–648, 1998.
- Paulson, C. A., and J. J. Simpson, Irradiance measurements in the upper ocean, *J. Phys. Oceanogr.*, 7, 952–956, 1977.
- Peters, H., and H. Baumert, Validating a turbulence closure against estuarine microstructure measurements, *Ocean Modelling*, 19, 183–203, 2007.
- Piechura, J., and A. Beszczynska-Möller, Inflow waters in the deep regions of the southern Baltic Sea - transport and transformations, *Oceanologia*, 45, 593–621, 2003.
- Pietrzak, J., The use of TVD limiters for forward-in-time upstream-biased advection schemes in ocean modeling, *Monthly Weather Review*, 126, 813–830, 1998.
- Pietrzak, J., J. Jakobson, H. Burchard, H.-J. Vested, and O. Petersen, A three-dimensional hydrostatic model for coastal and ocean modelling using a generalised topography following co-ordinate system, *Ocean Modelling*, 4, 173–205, 2002.
- Ranasinghe, R., and C. Pattiaratchi, Circulation and mixing characteristics of a seasonally open tidal inlet: a field study, *Mar. Freshwater Res.*, 50, 281–290, 1999.
- Reissmann, J. H., H. Burchard, R. Feistel, E. Hagen, H. U. Lass, V. Mohrholz, G. Nausch, L. Umlauf, and G. Wieczorek, Vertical mixing in the Baltic Sea and consequences for eutrophication - a review, *Progress in Oceanography*, 82, 47–80, 2009.
- Rennau, H., and H. Burchard, Quantitative analysis of numerically induced mixing in a coastal model application, *Ocean Dynamics*, 59, 671–687, 2009.
- Riemenschneider, U., and S. Legg, Regional simulations of the Faroe Bank Channel overflow in a level model, *Ocean Modelling*, 17, 93–122, 2007.
- Rippeth, T. P., and J. H. Simpson, The frequency and duration of episodes of complete vertical mixing in the Clyde Sea, *Cont. Shelf Res.*, 16, 933–947, 1996.
- Rippeth, T. P., N. Fisher, and J. H. Simpson, The semi-diurnal cycle of turbulent dissipation in the presence of tidal straining, *J. Phys. Oceanogr.*, 31, 2458–2471, 2001.

- Schinke, H., and W. Matthäus, On the causes of major Baltic inflows — an analysis of long time series, *Cont. Shelf Res.*, 18, 67–97, 1998.
- Scott, C. F., A prescriptive bulk model of periodic estuarine stratification driven by density currents and tidal straining, *Environmental Modeling and Assessment*, 9, 13–22, 2004.
- Seifert, T., and B. Kayser, A high resolution spherical grid topography of the Baltic Sea, *Meereswiss. Ber., Warnemünde*, 9, 73–88, 1995.
- Sharples, J., and J. H. Simpson, Semi-diurnal and longer period stability cycles in the Liverpool Bay region of freshwater influence, *Cont. Shelf Res.*, 15, 295–313, 1995.
- Shchepetkin, A. F., and J. C. McWilliams, A method for computing horizontal pressure-gradient force in an oceanic model with a nonaligned vertical coordinate, *J. Geophys. Res.*, 108, 10.1029/2001JC001047, 2003.
- Simpson, J., and D. Bowers, Models of stratification and frontal movement in shelf seas, *Deep-Sea Res.*, 28A, 727–738, 1981.
- Simpson, J. H., The shelf-sea fronts: implications of their existence and behaviour, *Phil. Trans. R. Soc. Lond. A*, 302, 531–546, 1981.
- Simpson, J. H., and J. R. Hunter, Fronts in the Irish Sea, *Nature*, 250, 404–406, 1974.
- Simpson, J. H., D. G. Hughes, and N. C. G. Morris, The relation of seasonal stratification to tidal mixing on the continental shelf, *A Voyage to Discovery. Deep-Sea Research (Suppl.)*, pp. 327–340, 1977.
- Simpson, J. H., J. Brown, J. Matthews, and G. Allen, Tidal Straining, Density Currents, and Stirring in the Control of Estuarine Stratification, *Estuaries*, 13, 125–132, 1990.
- Simpson, J. H., H. Burchard, N. R. Fisher, and T. P. Rippeth, The semi-diurnal cycle of dissipation in a ROFI: model-measurement comparisons, *Cont. Shelf Res.*, 22, 1615–1628, 2002.
- Skamarock, W., Truncation error estimates for refinement criteria in nested and adaptive models, *Monthly Weather Review*, 117, 872–886, 1989.
- Slørdal, L., The Pressure Gradient Force in Sigma-Co-ordinate Ocean Models, *Int. J. Numer. Meth. Fluids*, 24, 987–1017, 1997.
- Song, Y., A general pressure gradient formulation for ocean models. Part I: Scheme design and diagnostic analysis, *Monthly Weather Review*, 126, 3213–3230, 1998.
- Song, Y., and D. B. Haidvogel, A semi-implicit ocean circulation model using a generalised topography-following coordinate, *J. Computat. Phys.*, 115, 228–244, 1994.
- Song, Y. T., and T. Hou, Parametric vertical coordinate formulation for multiscale, Boussinesq, and non-Boussinesq ocean modeling, *Ocean Modelling*, 11, 298–332, 2006.
- Song, Y. T., and D. G. Wright, A general pressure gradient formulation for ocean models. Part II: Energy, momentum and bottom torque consistency, *Monthly Weather Review*, 126, 3231–3247, 1998.

- Souza, A. J., N. R. Fisher, J. H. Simpson, and M. J. Howarth, Effects of tidal straining on the semi-diurnal cycle of dissipation in the Rhine region of freshwater influence: Comparison of model and measurements, *J. Geophys. Res.*, 113, C01,011, doi:10.1029/2006JC004,002, 2008.
- Stanev, E. V., and J.-M. Beckers, Numerical simulations of seasonal and interannual variability of the Black Sea thermohaline circulation, *J. Mar. Sys.*, 22, 241–267, 1999.
- Stelling, G. S., and J. A. T. M. van Kester, On the approximation of horizontal gradients in sigma co-ordinates for bathymetry with steep bottom slopes, *Int. J. Numer. Meth. Fluids*, 18, 915–935, 1994.
- Sverdrup, H. U., On conditions for the vernal blooming of phytoplankton, *J. du Conseil*, 18, 287–294, 1953.
- Thompson, J., Z. Warsi, and C. Mastin, *Numerical grid generation - foundations and applications*, Elsevier, New-York, 1985.
- Umlauf, L., and L. Arneborg, Dynamics of rotating shallow gravity currents passing through a channel. Part I: Observation of transverse structure, *J. Phys. Oceanogr.*, 39, 2385–2401, 2009a.
- Umlauf, L., and L. Arneborg, Dynamics of rotating shallow gravity currents passing through a channel. Part II: Analysis, *J. Phys. Oceanogr.*, 39, 2402–2416, 2009b.
- Umlauf, L., and H. Burchard, Second-order turbulence models for geophysical boundary layers. A review of recent work, *Cont. Shelf Res.*, 25, 795–827, 2005.
- Umlauf, L., H. Burchard, and K. Bolding, General Ocean Turbulence Model. Source code documentation, *Tech. Rep. 63*, Baltic Sea Research Institute Warnemünde, Warnemünde, Germany, 2005.
- Umlauf, L., L. Arneborg, H. Burchard, V. Fiekas, H. U. Lass, V. Mohrholz, and H. Prandke, The transverse structure of turbulence in a rotating gravity current, *Geophys. Res. Letters*, 34, L08,601, doi:10.1029/2007GL029,521, 2007.
- Umlauf, L., L. Arneborg, R. Hofmeister, and H. Burchard, Entrainment in shallow rotating gravity currents: A modeling study., *J. Phys. Oceanogr.*, 40, 1819–1834, 2010.
- van Aken, H. M., The onset of stratification in shelf seas due to differential advection in the presence of a salinity gradient, *Cont. Shelf Res.*, 5, 475–485, 1986.
- Wählin, A. K., and C. Cenedese, How entraining density currents influence the stratification in a one-dimensional ocean basin, *Deep-Sea Res. II*, 53, 172–193, 2006.
- Wai, O. W. H., and Q. Lu, Gradient-Adaptive-Sigma (GAS) grid for 3d mass-transport modeling, *Journal of Hydraulic Engineering*, 125, 141–151, 1999.
- Warner, J. C., C. R. Sherwood, H. G. Arango, and R. P. Signell, Performance of four turbulence closure models implemented using a generic length scale method, *Ocean Modelling*, 8, 81–113, 2005.

-
- White, L., and A. Adcroft, A high-order finite volume remapping scheme for nonuniform grids: The piecewise quartic method (PQM), *Journal of Computational Physics*, 227, 7394–7422, 2008.
- Wieczorek, G., E. Hagen, and L. Umlauf, Eastern Gotland Basin case study of thermal variability in the wake of deep water intrusions, *J. Mar. Sys.*, 74, 65–74, 2008.
- Wiles, P., L. van Duren, C. Häse, J. Larsen, and J. H. Simpson, Stratification and mixing in the Limfjorden in relation to mussel culture, *J. Mar. Sys.*, 60, 129–143, 2006.
- Winters, K. B., P. N. Lombard, J. J. Riley, and E. A. d’Asaro, Available potential energy and mixing in density-stratified fluids, *J. Fluid Mech.*, 289, 115–128, 1995.

Lebenslauf des Autors

Name Richard Hofmeister
Geburtsdatum 9. April 1982
Geburtsort Neustrelitz, Deutschland
Nationalität Deutsch
Familienstand verheiratet, 2 Töchter (geboren 2006 und 2008)

Jul 1999 Schulabschluss Abitur
(*Gymnasium Carolinum, Neustrelitz*)

Okt 1999 - Sep 2001 Grundstudium Physik-Diplom (*Universität Rostock*)

Okt 2001 - Jul 2002 Zivildienst (*DRK, Neustrelitz*)

Okt 2002 - Jun 2006 Hauptstudium Physik-Diplom (*Universität Rostock*),
Abschluss: Diplom in Physik

Jul 2006 - Okt 2010 Promotionsstudium Physikalische Ozeanographie
(*Leibniz Institut für Ostseeforschung, Warnemünde*)

Selbstständigkeitserklärung

Ich versichere hiermit, dass ich die vorliegende Arbeit selbstständig angefertigt und ohne fremde Hilfe verfasst habe, keine außer den von mir angegebenen Hilfsmitteln und Quellen dazu verwendet habe und die den benutzten Werken inhaltlich und wörtlich entnommenen Stellen als solche kenntlich gemacht habe.

Rostock,